

**HIGH-SPATIAL-RESOLUTION SM-ND & U-PB AND LU-HF & U-PB ISOTOPE
GEOCHEMISTRY OF MONAZITE AND ZIRCON IN THE OLD WOMAN- PIUTE BATHOLITH,
CALIFORNIA**

By Stacy E. Phillips

s.phillips@mun.ca

A Thesis submitted to the School of Graduate Studies in partial fulfilment of the
requirements for the degree of

M.Sc. Geology

Department of Earth Sciences

Memorial University of Newfoundland

May 2015

St John's, Newfoundland

Abstract

The Old Woman-Piute Range Batholith (OWPB) in the Mojave Desert of south-eastern California is a suite of metaluminous and peraluminous Cretaceous granites that intrudes Proterozoic basement. The peraluminous Sweetwater Wash, Painted Rock and North Piute plutons were sampled to investigate geochemical heterogeneity. Zircon and monazite crystals were analysed for U–Pb & Lu–Hf and U–Pb & Sm–Nd isotopes, respectively, using the high-spatial resolution and the recently developed Laser Ablation Split Stream (LASS) approach. Inherited cores are widespread in zircon, limited in monazite, and yield U–Pb ages that range from 1800–1400 Ma, consistent with regional Proterozoic crustal building events. Zircon and monazite rims give a range of crystallisation ages between 70–75 Ma. The OWPB shows a large range in ϵ_{Hf} and ϵ_{Nd} in both inherited and magmatic populations, a characteristic that is derived primarily from the Proterozoic crustal source, but also influenced by the partial dissolution and preservation of inherited grains.

Acknowledgements

First and foremost, my thanks go to my supervisor Dr. John M. Hanchar. He designed this amazing project, allowed me to undertake field work in the Mojave Desert, and allowed me to travel to Washington State University to do some of my analyses. His help, support, advice and discussions have been invaluable to me as I have pursued my Master's. I am most appreciative for everything he has done for me. Thanks also go to Dr. Calvin Miller who has offered much guidance in dealing with the rocks that he knows so well, and to Dr. Chris Fisher for his patience and assistance during my trip to WSU and subsequent discussions about the results.

The numerous analytical staff at MUN; Pam King, Sherri Strong, Wanda Aylward and Rebecca Lam. Thank you for being the unsung heroes of my research. Thanks to my colleagues Anne Westhues and William Bradford who have been my main sources of scientific discussion, always happy to talk through an idea when I wander into their respective offices. To all my fellow graduate students and friends, thank you for helping me keep my sanity over the last few years.

Funding for this project was primarily by a Natural Sciences and Engineering Research Council (NSERC) Discovery Grant to Dr. John M. Hanchar. Additional funding was provided by a Mineralogical Society of America (MSA) Grant for Student Research in Mineralogy and Petrology to Stacy Phillips and the Department of Earth Sciences, Memorial University of Newfoundland.

Table of Contents

Abstract	ii
Acknowledgements	iii
Table of Contents	iv
List of Tables	vii
List of Figures	viii
List of Abbreviations	ix
List of Appendices	x
Chapter 1 - Introduction and Overview	1
1.1 - Background	1
1.2 – Aims	3
1.3 - Methods	4
1.4 - Geological overview	5
1.4.1 - Regional geology	5
1.4.2 - Nature of the Old Woman-Piute batholith	10
1.4.3 - Previous petrochemical investigations	16
1.5 - LASS technique	18
1.6 - Presentation	20
1.7 - Co-authorship Statement	21
Chapter 2 - High-spatial-resolution Sm-Nd & U-Pb and Lu-Hf & U-Pb isotope geochemistry of monazite and zircon in Old Woman-Piute Batholith, Mojave Desert, southeastern California	23
2.1 - Abstract	24
2.2 - Introduction	25
2.3 - Geological overview	28
2.3.1 - Regional geology	28
2.3.2 - Nature of the Old Woman-Piute batholith	30

2.3.3 - Previous work	31
2.3.4 - Sample descriptions	34
2.4 - Analytical Methods	36
2.4.1 - LASS method	38
2.5 - Results	41
2.5.1 - Major and trace element geochemistry	41
2.5.2 - Whole rock saturation temperature calculations	41
2.5.3 - Whole-rock isotopes (Sr, Sm-Nd and Lu-Hf)	47
2.5.4 - Accessory mineral characterisation	49
2.5.5 - <i>In situ</i> data	54
2.5 - Discussion	58
2.5.1 - Differentiation trends in an evolving magma	58
2.5.2 - Saturation temperatures	60
2.5.3 - Whole rock radiogenic tracer isotopes	61
2.5.4 - U-Pb data	62
2.5.5 - Tracer isotope data	63
2.5.6 - Epsilon-Time plots	65
2.5.7 - Levels of isotopic heterogeneity in the OWPB	67
2.5.8 - Inheritance and growth of accessory minerals	70
2.6 - Conclusions	74
2.7 - Acknowledgements	75
2.8 - References	76
Chapter 3 - Summary	96
3.1 - Usefulness of the LASS technique	111
3.2 - Directions for future research	112
3.3 - Conclusions	113
References	116
Appendix A - Analytical Methods	137

A.1 - Analytical Methods: Whole Rock	137
A.2 - Major and trace elements	137
A.2.1 - Crushing	137
A.2.2 - Whole rock major and trace elements	137
A.3 - Whole rock isotopes	138
A.3.1 - Whole rock isotope column chemistry (MUN)	138
A.3.2 - Sm-Nd & Sr column chemistry (MUN)	138
A.3.3 - Sm-Nd & Sr TIMS analysis (MUN)	139
A.3.4 - Lu-Hf column chemistry (MUN)	139
A.3.5 - Lu-Hf MC-ICP-MS analysis (MUN)	140
A.4 - Analytical Methods: <i>In situ</i>	141
A.4.1 - LASS setup (WSU)	141
A.4.2 - U-Pb zircon analysis (Portsmouth)	142
A.4.3 - Lu-Hf & LASS zircon analyses (WSU)	145
A.4.4 - Zircon data reduction	147
A.4.5 - Monazite LASS (WSU)	147
A.4.6 - Monazite LASS data reduction	150
A.5 - Isotopic reservoir values	151
Appendix B - Analysis of reference standards	153
B.1 - Whole rock isotopic standards	153
B.2 - <i>In situ</i> isotopic standards	154
B.2.1 - U-Pb only standards (UoP)	154
B.2.2 - Lu-Hf only standards (WSU)	154
B.2.3 - LASS zircon standards	155
B.2.4 - LASS monazite standards	159
Appendix C – Supplementary data files	163

List of Tables

Chapter 2

Table 2.1 - Location and petrological summary of OWPB samples.

Table 2.2 - Summary of radiogenic isotopic analyses done on OWPB samples.

Table 2.3 - Whole rock major and trace element data for the OWPB samples.

Table 2.4 - Whole rock zircon (TZr) and monazite (TMnz) saturation temperatures for the OWPB samples.

Table 2.5 - Whole rock Sm-Nd, Sr and Lu-Hf data for the OWPB samples.

Table 2.6 - *In situ* isotopic ranges of zircon and monazite grains.

List of Figures

Chapter 1

- Figure 1.1** – Location of the OWPB in relation to regional geological features.
Figure 1.2 – Intrusive relationship of the SWP granite and the Fenner Gneiss.
Figure 1.3 – Geological map of the OWPB.
Figure 1.4 – Schematic cross section of the OWPB.
Figure 1.5 – Geological map of the SWP.

Chapter 2

- Figure 2.1:** Geological maps of the OWPB.
Figure 2.2: Schematic diagram of the Laser Ablation Split Stream (LASS) analytical setup.
Figure 2.3: Whole rock Harker plots of major and trace elements of the OWPB samples.
Figure 2.4: Chondrite normalised whole rock rare earth element plots for the OWPB samples.
Figure 2.5: Whole rock tracer isotope data for OWPB samples.
Figure 2.6: CL & BSE images of zircon crystals from the OWPB.
Figure 2.7: BSE images of monazite crystals from the OWPB.
Figure 2.8: Th-rich monazite crystals.
Figure 2.9: X-ray maps of selected monazite grains.
Figure 2.10: *In situ* zircon U-Pb isotopic data.
Figure 2.11: *In situ* monazite U-Pb isotopic data.
Figure 2.12: *In situ* zircon Lu-Hf isotopic data.
Figure 2.13: *In situ* monazite Sm-Nd isotopic data.
Figure 2.14: *In situ* monazite REE data.
Figure 2.15: Epsilon – time plots for OWPB *in situ* isotopic data.

List of Abbreviations

EPMA	electron probe micro analysis
LA-ICP-MS	laser ablation inductively coupled plasma mass spectrometry
LASS	laser ablation split-stream
LREE	light rare earth elements
MC-ICP-MS	multi collector inductively coupled plasma mass spectrometry
MG	metaluminous granitoids
MSWD	mean square weighted deviates
NPP	North Piute Pluton
OWPB	Old Woman-Piute Batholith
PG	peraluminous granitoids
ppm	parts per million
PRP	Painted Rock Pluton
REE	rare earth elements
r.s.d.	residual standard deviation
SWP	Sweetwater Wash Pluton
ID-TIMS	isotope dilution thermal ionisation mass spectrometry
wt. %	weight percent

List of Appendices

Appendix A: Analytical Methods

A.1 - Analytical Methods: Whole Rock

A.2 - Major and trace elements

A.2.1 - Crushing

A.2.2 - Whole rock major and trace elements

A.3 - Whole rock isotopes

A.3.1 - Whole rock isotope column chemistry

A.3.2 - Sm-Nd & Sr column chemistry

A.3.3 - Sm-Nd & Sr TIMS analysis

A.3.4 - Lu-Hf column chemistry

A.3.5 - Lu-Hf MC-ICP-MS analysis

A.4 - Analytical Methods: *In situ*

A.4.1 - LASS setup

A.4.2 - U-Pb zircon analysis (UoP)

Table A.4.2.1 - Zircon U-Pb operating parameters and data acquisition parameters (UoP).

A.4.3 - Lu-Hf & LASS zircon analyses (WSU)

Table A.4.3.1 - Zircon LASS operating parameters (WSU).

A.4.4 - Zircon data reduction

A.4.4.1 - Lu-Hf

A.4.4.2 - LASS U-Pb

A.4.5 - Monazite LASS

Table A.4.5.1 - Monazite LASS operating parameters (WSU).

A.4.6 - Monazite LASS data reduction

A.4.6.1 - Sm-Nd

A.4.6.2 - U-Pb

A.5 - Isotopic reservoir values

Appendix B: Analysis of reference standards

B.1 - Whole rock isotopic standards

B.2 - *In situ* isotopic standards

B.2.1 - U-Pb only (UoP)

Figure B.2.1.1 - Weighted average plots of Plešovice and GJ-1 standard U-Pb analyses.

B.2.2 - Lu-Hf only (WSU)

Figure B.2.2.1 - Weighted average plots of B144/MunZirc standard Lu-Hf analyses.

B.2.3 - LASS zircon standards

Figure B.2.3.1 - Weighted average plots of Plešovice and FC-1 standard Lu-Hf analyses.

Figure B.2.3.2 - Concordia and weighted average plot of Mud Tank standard LASS analyses.

Figure B.2.3.3 - Weighted average plot of B144/MunZirc standard Lu-Hf LASS analyses.

Figure B.2.3.4 - Concordia and weighted average plot of 91500 standard LASS analyses.

B.2.4 - LASS monazite standards

Figure B.2.4.1 - Weighted average plot of Trebilcock, JNd-1 glass and LREE glass standard Sm-Nd analyses.

Figure B.2.4.2 - Concordia and weighted average plot of KMO standard LASS analyses.

Figure B.2.4.3 - Terra-Wasserburg and weighted average plot of Thai standard LASS analyses.

Appendix C: Supplementary data files

Chapter 1 - Introduction and Overview

1.1 - Background

In situ analyses of accessory minerals at the sub-grain scale have proven to be effective tools for understanding the origins and evolution of magmatic systems, with studies often utilising multiple isotopic systems and minerals (e.g., Kemp et al., 2007; McFarlane & McCulloch, 2007; Xie et al., 2008). Improvements in *in situ* analytical methods such as SIMS (secondary ionisation mass spectrometry), LA-ICP-MS (laser ablation inductively coupled plasma mass spectrometry) and LA-MC-ICP-MS (laser ablation inductively coupled plasma multi collector mass spectrometry) have revealed details of magmatic processes at increasingly finer temporal and spatial scales. The majority of these isotopic studies have focused on zircon (Amelin et al., 2000; Harrison et al., 2005; Hawkesworth & Kemp, 2004). When U-Pb geochronology is combined with O and Lu-Hf isotopes (and in some cases trace elements), the integration of these isotopic systems can be a powerful petrogenetic tool for studying both granitic rocks (Crowley et al., 2008) and high grade metamorphic rocks (Schaltegger et al., 1999). Similar to zircon, the mineral monazite-(Ce) ($[Ce,La,Nd,Th]PO_4$) is also a powerful tracer of crustal processes (Hawkins & Bowring, 1997; Tomascak et al., 1998; Iizuka et al., 2011). The potential to simultaneously measure U-Pb and tracer (e.g., Lu-Hf and Sm-Nd) isotopes in zircon and monazite respectively by the laser ablation split stream (LASS) method (Yuan et al., 2008; Fisher et al., 2014; Goudie et al., 2014) in complex,

compositionally zoned, accessory minerals allows for a high-resolution spatial and temporal snapshot of the crystallisation history at a finer scale than would be achieved using whole mineral grain, or whole-rock, samples. This ability to resolve intra-crystalline heterogeneity is an important tool for geoscientists as geological processes are sought to be understood at ever smaller scales (Nemchin et al., 2013).

The late Cretaceous Old Woman-Piute Batholith (OWPB) in the Mojave Desert of southeastern California is an excellent natural laboratory in which to utilise these techniques in order to understand the petrogenesis of peraluminous continental arc granites. Three such plutons (Sweetwater Wash, North Piute, and Painted Rock) were chosen for detailed analysis in this study. The Sweetwater Wash Pluton (SWP) is well characterised in terms of field relations and geochemistry (e.g., whole rock major, minor and trace elements, radiogenic tracer and stable isotopes) (Mittlefehldt & Miller, 1983; Miller et al., 1990; Wark & Miller, 1993) allowing for further detailed mineral-scale analysis. A preliminary study of monazite in the SWP by Fisher et al. (in preparation) documented the presence of significant isotopic heterogeneity. The North Piute Pluton (NPP) and the Painted Rock Pluton (PRP), both of similar age to the SWP, have received less attention, and so this study will act as the first dedicated work on these plutons. These plutons will also provide useful comparisons to the more extensive SWP and will allow potential heterogeneities in the OWPB to be investigated at the batholith scale.

The current study aims to investigate and explain scales of heterogeneity of the OWPB and constrain its petrogenesis within a local and a regional context. Fieldwork

involved systematic sampling along a transect in the SWP allowing spatial and temporal variations to be investigated via the records preserved in the chemistry of accessory minerals. Samples were also collected from the NPP and PRP as part of this comparative study. This study is the first to thoroughly investigate the petrogenesis of a plutonic system by analysing monazite by the LASS method, and by combining this with zircon U-Pb and Lu-Hf data, a high-spatial-resolution geochronological and chemical record will be revealed. Furthermore, verifying and understanding the isotopic heterogeneity observed in the OWPB will provide important insights into monazite and zircon isotope systematics and crustal evolution.

1.2 – Aims

- To investigate the variations in monazite and zircon isotope geochemistry throughout the SWP, NPP, and PRP.
- To examine potential mineral-scale isotopic disequilibrium in the SWP, NPP, and PRP.
- To compare the SWP to other peraluminous granites in the Old Woman-Piute Range batholith.
- To use mineral-scale U-Pb and tracer isotope heterogeneity to understand magma chamber processes in a well-characterized plutonic system and to develop a model for the petrogenesis of the OWPRB.

1.3 - Methods

- Description of rock types in the OWP through field observations, hand samples and thin section petrography
- Use of BSE imaging (zircon and monazite), cathodoluminescence (zircon) and compositional X-ray mapping (monazite) to characterise zonation patterns
- U-Pb dating of monazite and zircon grains by LA-ICP-MS, done at University of Portsmouth
- Lu-Hf isotopic analysis of dated zircon grains by MC-ICP-MS, done at Washington State University
- U-Pb and Sm-Nd isotopic analysis of monazite grains by LASS, done at Washington State University
- Whole rock major and trace element geochemistry of all samples by ICP-MS, analysed by ACT-LABS
- Whole rock Sr and Sm-Nd isotopic analysis of all samples by TIMS, done at Memorial University of Newfoundland
- Whole rock Lu-Hf isotopic analysis of all samples by MC-ICP-MS, done at Memorial University of Newfoundland

1.4 - Geological overview

1.4.1 - Regional geology

The crust into which the OWPB intruded is long-lived and has a complex geologic history. The oldest rocks exposed today are of Proterozoic age (1.8 to 1.7 Ga), but U-Pb data for detrital and inherited zircon grains from Proterozoic supracrustal and intrusive rocks and Mesozoic plutons document the existence of an older component in the eastern Mojave Desert (very early Proterozoic to Late Archean, 2-3 Ga) (Wooden & Miller, 1990; Kapp et al., 2002; Barth et al., 2009; Strickland et al., 2013). Sm-Nd model ages from Proterozoic crystalline rocks also suggests the presence of 2.0-2.3 Ga crust under the area (Bennett & DePaolo, 1987). Whole rock Pb isotopic compositions at 1.7 Ga are distinctive having high $^{207}\text{Pb}/^{204}\text{Pb}$ and very high $^{208}\text{Pb}/^{204}\text{Pb}$ relative to $^{206}\text{Pb}/^{204}\text{Pb}$ (Wooden & Miller, 1990). This Nd and Pb isotopic character of the Eastern Mojave Desert crust is distinct from similar Proterozoic provinces of North America, probably reflecting input from Archean crust into Paleoproterozoic sedimentary sequences and mantle-derived magmas (e.g., Bennett & DePaolo, 1987).

The oldest exposed rocks of the eastern Mojave Desert crust are immature clastic metasedimentary rocks derived from an adjacent arc terrane and deposited at 1.79-1.75 Ga (Barth et al., 2009; Strickland et al., 2013). This supracrustal sequence was intruded by slightly younger mafic and granitic magmas and then metamorphosed at upper amphibolite to granulite facies, migmatized, and intruded by more granites in a

series of events that lasted until ca. 1.67 Ga (Wooden & Miller, 1990; Barth et al., 2009; Strickland et al., 2013).

Moderate volumes of granite were emplaced in the Mojave crust at ~1.4 Ga and form part of the NE-SW trending “anorogenic” belt that runs from northern Europe, through Labrador, across the eastern and southern United States, and into Southern California (Anderson, 1983). Siliciclastic and carbonate-dominated shelf sedimentation occurred from the Neoproterozoic into the Cambrian recording the change from a stable passive margin into a rifting phase, and then into the establishment of passive margin sedimentation by the earliest Cambrian that continued to the Permian and Triassic (Walker, 1988; Miller et al., 1990; Barth et al., 2009).

The OWPB is located to the east of the 0.706 $^{87}\text{Sr}/^{86}\text{Sr}$ line (Kistler, 1990), and within a muscovite-granite belt that extends throughout the Cordillera (Figure 1.1). This geochemical boundary has been interpreted to represent either the margin of the Proterozoic crust (Miller & Bradfish, 1980; Kistler, 1990), or alternatively, the western edge of the North American lithospheric mantle (Miller et al., 2000). The strongly peraluminous nature of much of the OWPB is in contrast to that of other Mesozoic batholiths such as the Sierra Nevada and Peninsular Ranges, where muscovite-bearing plutons are much less common.

Intense reactivation of the North American craton occurred in the Mesozoic during the Sevier Orogeny and continued through the Laramide Orogeny (Livaccari,

1991). Plutonism in the Mojave began in the mid-Jurassic with the subduction of the Farallon Plate under the North American Plate, expressed in the vicinity of the OWPB by the emplacement of the synkinematic Clipper Mountains pluton at ~160 Ma and abundant 145 Ma dikes (Miller & Wooden, 1994). As subduction continued into the Cretaceous the tectonic style varied along the arc reflecting the complexities of oblique convergence of the subducting slab. Contractual orogenic forces caused the formation of the Fenner Shear zone to the east of the Piute Mountains, through which the ~85 Ma East Piute pluton was emplaced (Karlstrom et al., 1993).

The major episode of magmatism in the Eastern Mojave occurred between 75-70 Ma, proposed to be due to the collapse of the inland orogenic belt after the tectonically thickened crust encountered the lithosphere of the Colorado Plateau (Livaccari, 1991). During the Late Cretaceous two distinct types of magma were emplaced: earlier metaluminous- to weakly peraluminous (MG) granodiorites and later peraluminous granites (PG). These peraluminous and metaluminous intrusions account for ~85% of the total exposed intrusive mass in the Mesozoic upper crust in the OWPB (Miller & Wooden, 1994).

Rapid unroofing of the OWPB from mid-crustal levels occurred during the Late Cretaceous and into the early Tertiary. $^{40}\text{Ar}/^{39}\text{Ar}$ thermochronology and apatite fission track data suggest that the Old Woman Mountains area initially cooled rapidly at a rate of 100°C/m.y. between 73 and 70 Ma through conduction of heat to surrounding rocks, and then by 10-30°C/m.y. until after 60 Ma (Foster et al., 1989; Foster et al., 1990;

Foster et al., 1992). Ductile shear zones, expressed as mylonitization and penetrative deformation of the deeper granitoids, are thought to be responsible for the unroofing in this region, in a similar fashion to other Cordilleran metamorphic core-complexes (Carl & Miller, 1991).

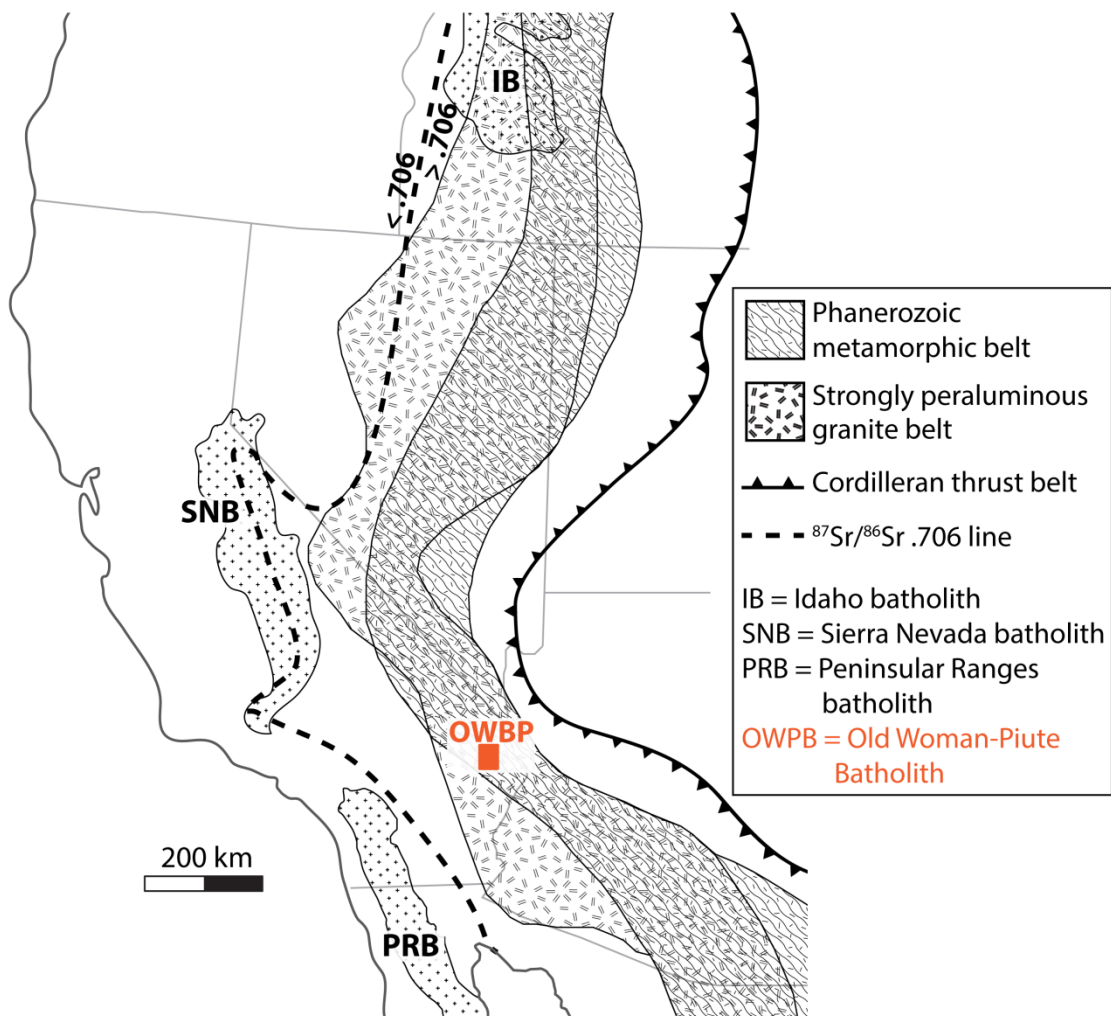


Figure 1.1 – Location of the OWPB in relation to regional geological features.

After Miller & Bradfish (1980).

1.4.2 - Nature of the Old Woman-Piute batholith

The country rocks into which the Old Woman-Piute (OWP) batholith intrudes are part of the Proterozoic complex of the eastern Mojave Desert. Towards the margins of the SWP there is a clear intrusive relationship between the granite and the gneiss, with intrusive veining, small scale migmatisation and dynamic mobilisation of gneiss blocks within the granite (Figure 1.2.).

The OWPB includes both of the Cretaceous magma series: the MG Old Woman and Goffs plutons and the strongly PG Sweetwater Wash (SWP), Painted Rock (PRP), North Piute (NPP), and Lazy Daisy plutons (Figure 1.3). The peraluminous granites, which are the focus of this study, occur in discrete plutons and show the temporal sequence muscovite-biotite granite → muscovite-biotite-garnet granite → muscovite-garnet granite → aplite and pegmatite (Mittlefehldt & Miller, 1983). Peraluminous granitoid rocks are uniformly felsic (70-76 wt. SiO₂) with sodic plagioclase > K-feldspar. Biotite is present in all but the most felsic aplites, becoming subordinate with evolution and the appearance of garnet. Zircon and monazite are important accessory minerals, both minerals being more abundant in the biotite-rich samples.

Regional tilting exposes deeper structural levels of the Old Woman batholith towards the south (Figure 1.4). Roof contacts are typically sharp with injections of aplite/pegmatite dikes being common. The roof and floor sections of the Sweetwater Wash pluton are sheet like, and whilst enclaves are sparse in the roof zone the lower parts of the pluton grade into floor material with increasing proportions of country rock.

Beneath this heavily injected zone is a sheared heterogeneous zone of gneissic country rock below which is the sheet-like MG Old Woman granodiorite (Miller et al., 1990). A similar sheared zone is present at its base with extensive migmatisation present at depth. The PRP, which is completely enclosed by the Old Woman pluton, encloses large blocks of the Old Woman granodiorite. At the cm-scale there is evidence of interaction between the two rock types, possibly assimilation or mixing having occurred. Dikes observed to cut the Old Woman pluton above the PRP may represent feeder dikes for the shallower Sweetwater Wash pluton (Miller et al., 1990). Multiple mineral barometers suggest that the NPP was emplaced at ~10 km and the SWP at ~15km (Foster et al., 1992).

Garnet-bearing granite facies occur in the SWP and PRP, which has been mapped along the margins of the SWP (Figure 1.5). Garnet-bearing aplite/pegmatite facies also occur sporadically in the SWP and tend to be located towards the centre of the pluton. The NPP is the most homogeneous of the three plutons, being composed of very uniform 2-mica granite.



Figure 1.2 – Intrusive relationship of the SWP granite and the Fenner Gneiss.

Facing south along Carbonate Gulch, at the south east margin of the Sweetwater Wash Pluton. The light coloured granite of the SWP in this boulder is seen to intrude the dark Fenner Gneiss unit. Metre sized rotated blocks have been incorporated into, and been intruded by the granite, reflecting the dynamic emplacement of the pluton. Figure b) is a zoomed-in image of Figure a). Photo by Stacy Phillips.

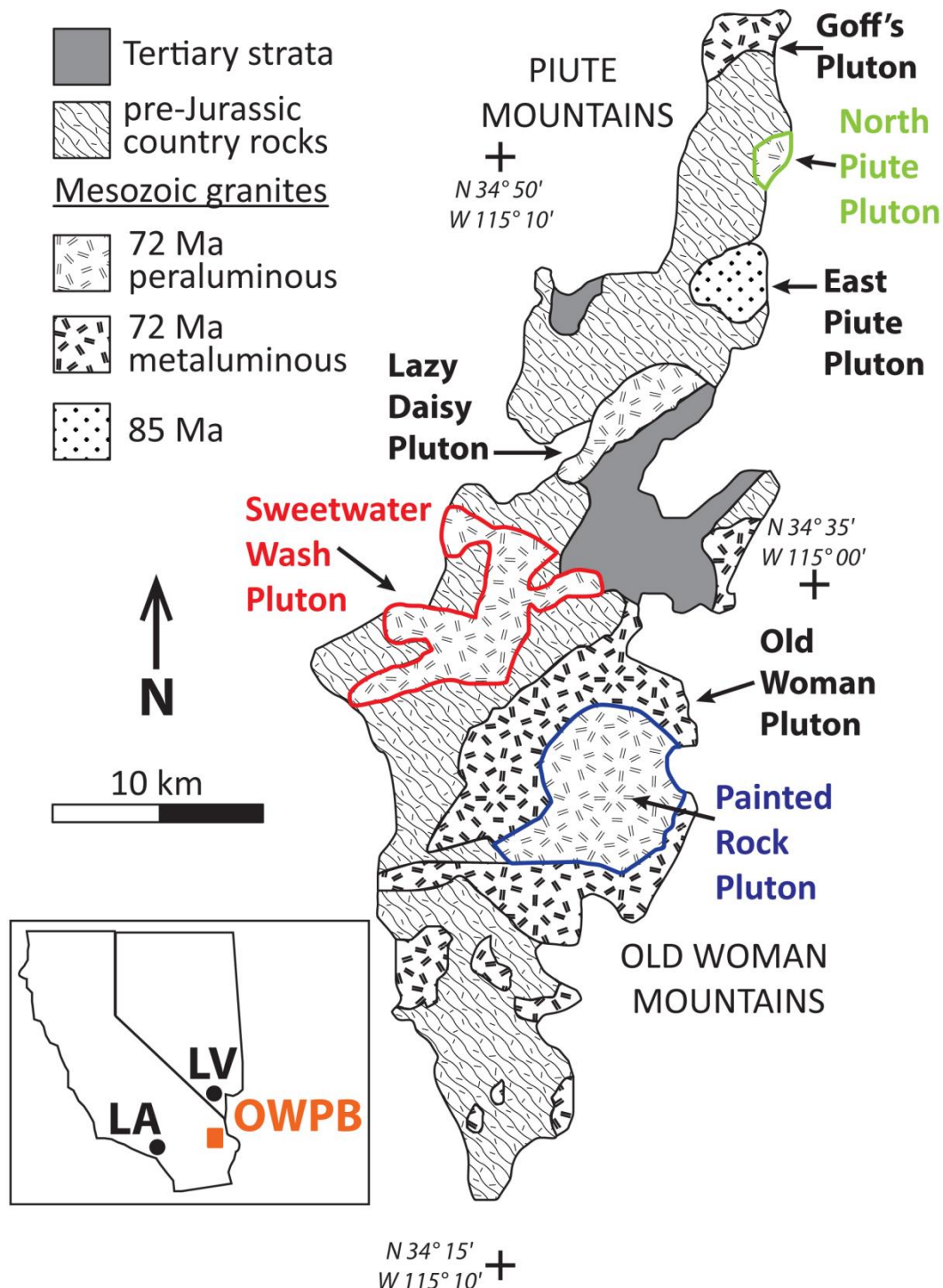


Figure 1.3 – Geological map of the OWPB.

Inset shows location of the OWPB relative to Los Angeles and Las Vegas.

After Miller & Wooden (1994)

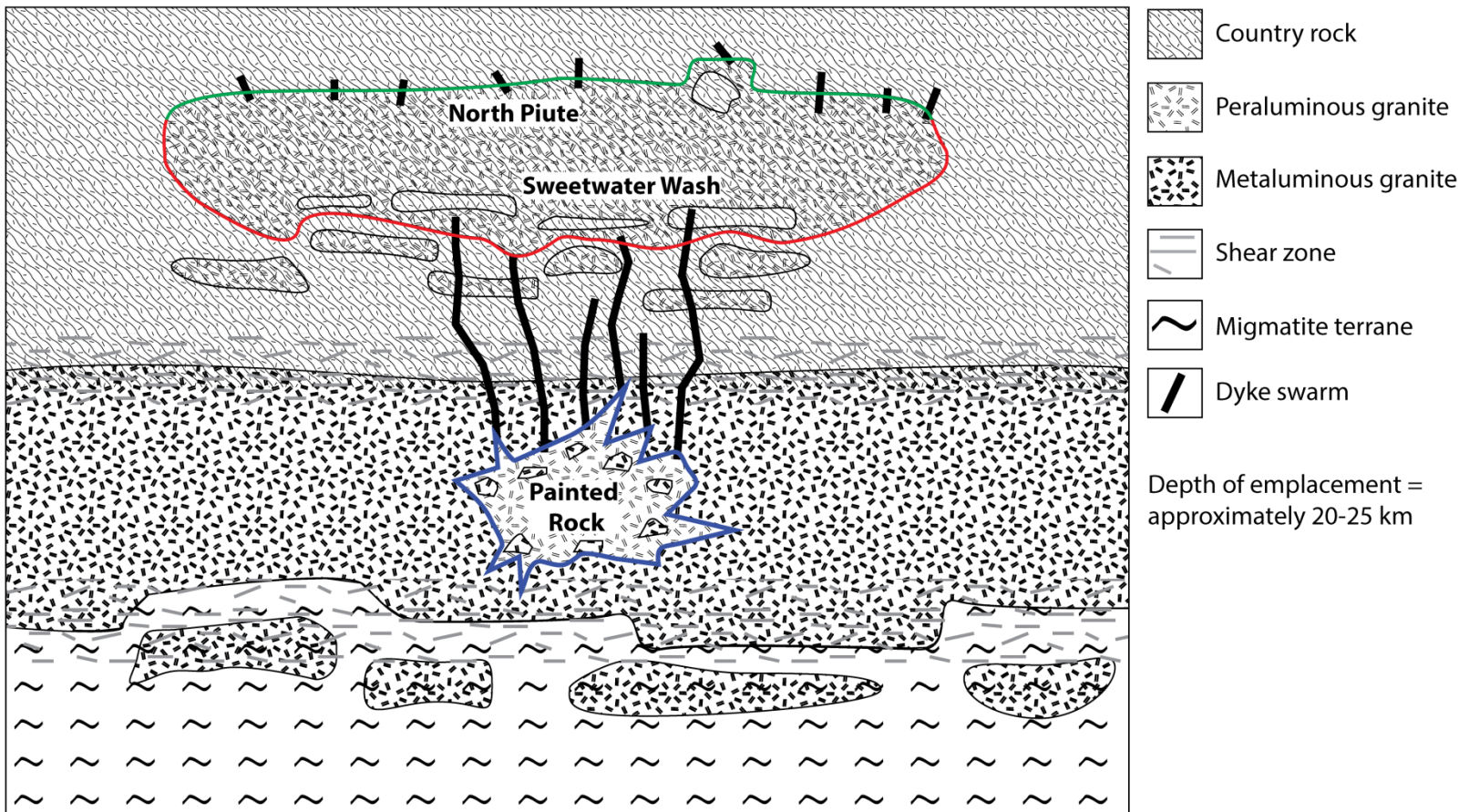


Figure 1.4 – Schematic cross section of the OWPB.

After Miller et al., (1990).

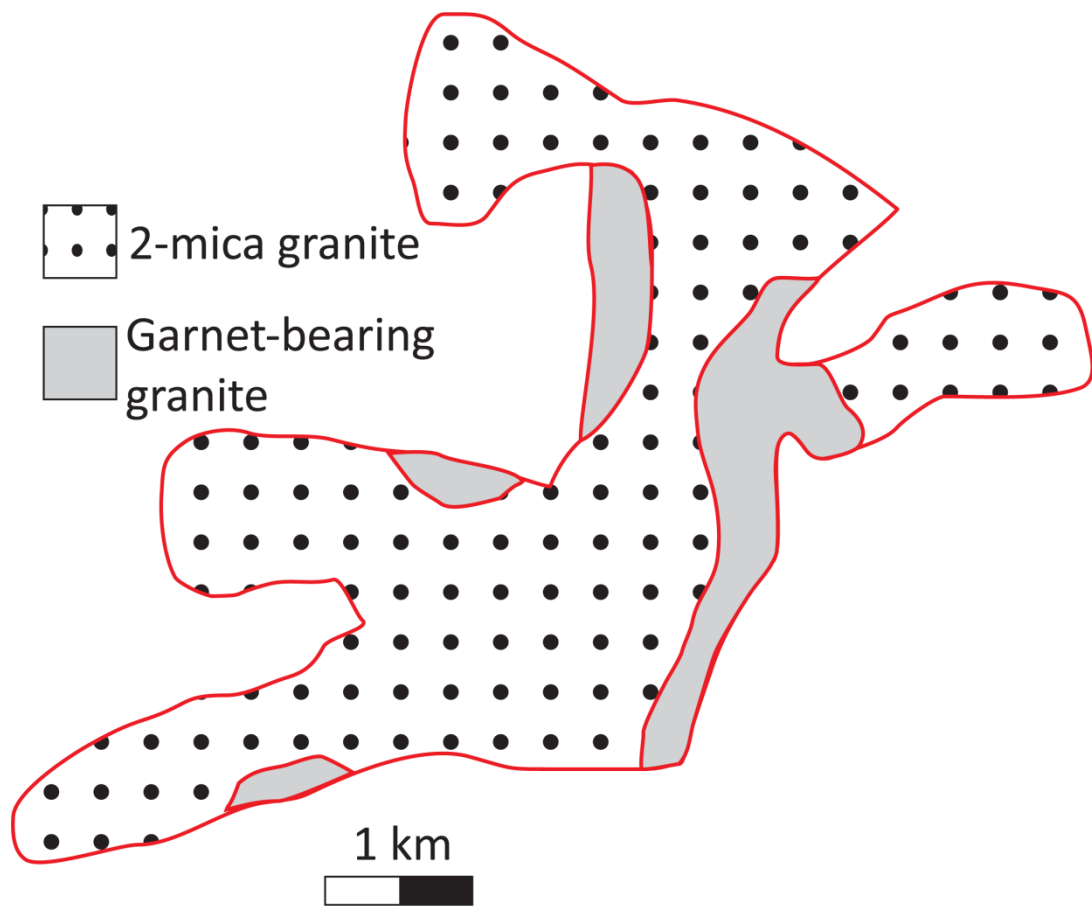


Figure 1.5 – Geological map of the SWP.

After Mittlefehldt & Miller (1983).

1.4.3 - Previous petrochemical investigations

The SWP has been well characterised petrochemically. Whole rock major and trace element analyses by Mittlefehldt & Miller (1983) show smooth geochemical evolutionary trends that are consistent with fractional crystallisation of the observed mineral assemblages. An increase in SiO₂ content between the 2-mica granite and the aplite/pegmatite samples is accompanied by a decrease in Ba and Sr and an increase in Rb, due to feldspar fractionation, while a decrease in LREE abundances is explained by monazite fractionation.

In situ ion probe U-Pb analyses of zircon crystals from the Old Woman granodiorite and Sweetwater Wash two-mica granite yield concordant analyses of 74 ± 3 Ma (2σ), and $^{40}\text{Ar}/^{39}\text{Ar}$ analyses of hornblende from the Old Woman granodiorite yield an age of 73 ± 2 Ma (2σ) (Foster et al., 1989). The SWP granite was found to contain numerous inherited zircon grains with ~50% of the zircon crystals showing anhedral Proterozoic cores and thin magmatic Cretaceous rims with well-formed growth zoning revealed in cathodoluminescence (CL) and back-scattered electron (BSE) imaging (Miller et al., 1992; Hanchar & Miller 1993). The dates for these inherited zircon cores span 1800-1100 Ma, consistent with the eastern Mojave Desert crust as described above (Bennett & DePaolo, 1987). The presence of these inherited zircon cores in the SWP is one of the driving forces behind using *in situ* techniques in accessory minerals such as zircon and monazite, as inter- and intra-crystal variations can reveal important insights

into crustal evolution and magma chamber processes that otherwise cannot be resolved at the whole-rock scale.

Further studies of the SWP have investigated monazite and other accessory minerals. Kingsbury et al., (1993) identified the presence of discordant inherited monazite grains that record U-Pb dates of 1800-1700 Ma, consistent with dates from inherited zircon crystals as described above (Foster et al., 1989). Wark & Miller (1993) investigated monazite, zircon, and xenotime in order to trace the geochemical evolution in the SWP as recorded in those accessory minerals. Differentiation of rock units from granite to aplite is accompanied by flattening of REE patterns in monazite, increasing concentrations of Hf and Y in zircon, and a slight increase in Gd/Ho ratios in xenotime, with U and Th increasing in each of the three phases. Accessory minerals also showed well-developed compositional zonation patterns of Hf, U, Th and REE within grains that reflect changing melt compositions with time.

The whole-rock major element, trace element and isotopic data presented in Miller et al. (1990), Miller et al. (1992), and Miller & Wooden (1994) (as detailed below) constrain the petrogenesis of the two magma series present in the OWPB, with differences between the metaluminous and peraluminous rock types being a function of source composition. High $^{87}\text{Sr}/^{86}\text{Sr}$ (MG = 0.7095-0.7115 vs PG = 0.7014-0.719) and low ϵ_{Nd} (MG = -10 to -12 vs PG = -16 to -17) indicate major contributions from the Proterozoic crust. Assuming that the both magma series were entirely derived from Proterozoic crust, time averaged Rb/Sr ratios for MG and PG rocks suggest a mafic-

intermediate igneous source for the MG and an intermediate-felsic igneous source for the PG series. This is also consistent with their whole-rock $\delta^{18}\text{O}$ values that rule out dominant contributions from either the mantle or sediments (e.g., $\delta^{18}\text{O} = 7.2$ to $9.3\text{\textperthousand}$). Similarly, the high Rb and Ba contents of MG rocks also precludes derivation from a solely mantle source, while the low Rb/Ba of PG rocks rules out a dominantly supracrustal pelitic source.

A suite of lower-crustal xenoliths from a Tertiary dike found in the northern Piute Mountains have Pb, Sr and Nd compositions that are consistent with derivation from a Proterozoic Mojave crust (Miller et al., 1992; Hanchar et al., 1994). Major and trace elements and radiogenic isotopic characteristics of the xenoliths suggest they represent the depleted residue (i.e., restite) after extraction of felsic melt. This Proterozoic Mojave crust is deemed to be heterogeneously composed of intermediate to felsic igneous rocks as well as diverse clastic sedimentary rocks. Modelling of the extracted melt yields compositions that are consistent with that of OWPB granitoids. Calculated melt fractions are variable (0-70%) and must have led to diverse melt compositions.

1.5 - LASS technique

This study serves as the first dedicated investigation into both monazite and zircon in magmatic systems using the laser ablation split stream (LASS) technique. The recently developed LASS method involves the simultaneous determination of U-Pb and Lu-Hf isotopes in zircon (Yuan et al., 2008; Fisher et al., 2014) and U-Pb and Sm-Nd isotopes simultaneously in monazite (Goudie et al., 2014). The ablated sample material

is split into two streams as it exits the ablation cell and U-Pb isotopes are measured by a magnetic sector high resolution (HR) ICP-MS and Sm-Nd or Lu-Hf isotopes are measured by a multicollector (MC-ICP-MS). This method allows for accurate determinations of initial isotopic compositions by using corresponding the U-Pb ages. The primary advantage of the LASS approach is that it allows a robust method of detecting mixed age analyses, which are possible in cases where multiple generations of growth are present in a single crystal. This is especially important in this study as monazite and zircon grains often have complex zoning patterns that reflect different isotopic compositions, and it is imperative that the tracer isotopes are measured in age zone of interest. If, for example, two age components are present in an analysis, sampling both components simultaneously will yield a discordant result and lie on a mixing line between the two ages on a conventional Concordia diagram. Non-split-stream methods involve the determination of U-Pb isotopes first, followed by analysis of tracer isotopes, which does not allow detection of multiple components in the trace isotope analysis. Further, the relatively small spot sizes (20-30 µm) used in this study also help to overcome, but not eliminate completely, issues with mixing different age and isotopic domains (Goudie, et al., 2014; Fisher, et al., 2014).

This method is therefore a powerful tool with which to understand the isotopic systematics of accessory minerals. The accuracy of the LASS method was examined in the above studies by analyses of a multitude of monazite and zircon reference standards that cover a wide range of ages and elemental compositions. It was found that LASS

results are in excellent agreement with accepted and in house reference values and the precision of the LASS technique is often comparable with that of analyses of single isotopic systems. Goudie et al. (2014) reported that the loss in sensitivity from splitting the ablation stream to the two mass spectrometers is ~14%, clearly less than might be expected by splitting the ablation stream into two parts.

1.6 - Presentation

This thesis is presented in manuscript format. Chapter 1 serves as an introduction to the project, an overview regional geology of the area, and a review of previous work. Chapter 2 is a manuscript for a peer-reviewed article that will be submitted as a paper (*High-spatial-resolution Sm-Nd & U-Pb and Lu-Hf & U-Pb isotope geochemistry of monazite and zircon in Old Woman-Piute Batholith, Mojave Desert, California*).

This paper describes the results of this study into the geochemistry of the Old Woman-Piute Batholith. A summary of the project is presented in Chapter 3, as well as proposed future work. Detailed methods for data analysis and reduction are presented in Appendix A, analyses of standard reference materials are presented in Appendix B, and full data tables are presented in Appendix C.

1.7 - Co-authorship Statement

Stacy Phillips: I carried out all of the sample preparation for both whole rock and *in situ* analytical work. This involved crushing of samples, isotopic separation by column chemistry, separation, picking and imaging of monazite and zircon grains, and analysis of zircon Lu-Hf and U-Pb & Lu-Hf by LASS, and U-Pb & Sm-Nd analysis of monazite by LASS. I also carried out data reduction of the data that I collected. The manuscript was written by myself and then passed onto co-authors. The interpretations and conclusions presented benefitted from continuous discussion with John M. Hanchar, Chris Fisher, and Calvin Miller at all stages of the project. Co-authors reviewed the manuscript and helped to improve it.

John M. Hanchar: John provided the design and helped the implementation of the M.Sc. project. He assisted with fieldwork and sample collection in the Mojave Desert and provided help and guidance throughout the project. John provided constructive criticism and discussion during preparation of the manuscript.

Chris Fisher: Chris provided technical assistance with sample analysis and data reduction during my visit to Washington State University. Previous work done by Chris led to the conception of this project, and the work has been improved by discussion with him regarding the interpretation of the results.

Calvin Miller: Calvin provided in depth knowledge of the Mojave Desert granites during fieldwork, as well as insights into granite genesis as data was discussed during manuscript preparation.

Penelope Lancaster & James Darling: Penelope and James carried out the zircon U-Pb analysis at the University of Portsmouth as the lab was not available at MUN. They provided constructive comments on interpretations and conclusions presented in the manuscript.

1 **Chapter 2 - High-spatial-resolution Sm-Nd & U-Pb and Lu-Hf & U-Pb**

2 **isotope geochemistry of monazite and zircon in Old Woman-Piute**

3 **Batholith, Mojave Desert, southeastern California**

4 To be submitted to *Geosphere*.

5 Stacy E. Phillips^{*1}, John M. Hanchar^{1**}, Calvin F. Miller², Christopher M. Fisher³, Penelope

6 J. Lancaster⁴, James R. Darling⁴, and Jeff D. Vervoort³.

7 (1) Department of Earth Sciences, Memorial University of Newfoundland, St. John's, NL,

8 A1B 3X5 Canada

9 (2) Earth & Environmental Sciences, Vanderbilt University, Nashville, TN 37235 USA

10 (3) School of the Environment, Washington State University, Pullman, WA, 99164 USA

11 (4) School of Earth and Environmental Sciences, University of Portsmouth, PO1 3QL,

12 United Kingdom

13 *e-mail: s.phillips@mun.ca

14 **Corresponding author e-mail: jhanchar@mun.ca

15 **Key words**

16 Zircon, monazite, crustal evolution, U-Pb geochronology, LA-ICPMS, LA-MC-ICPMS, laser

17 ablation split stream (LASS), Lu-Hf, Sm-Nd, Mojave, granite petrogenesis

18 **2.1 - Abstract**

19 The Old Woman-Piute Range Batholith (OWPB) in the Mojave Desert of south-
20 eastern California consists of a number of discrete metaluminous and peraluminous
21 plutons that intruded a long-lived and complex Proterozoic basement. Three strongly
22 peraluminous plutons were chosen to investigate isotopic heterogeneity at the sample-,
23 pluton- and batholith-scale. Zircon and monazite crystals were analysed for U–Pb & Lu–
24 Hf and U–Pb & Sm–Nd isotopes respectively, primarily using the laser ablation split
25 stream (LASS) approach. This approach allows for a detailed assessment of geochemical
26 changes in both Hf and Nd compositions in the magmatic system at a fine spatial scale,
27 while also ensuring only relevant growth domains are sampled.

28 The U–Pb data show widespread inheritance in zircon cores, yielding ages
29 between ~1800 and ~1400 Ma, while only four monazite grains yield “old” inherited
30 cores (~1700 Ma), these ages being consistent with the regional Proterozoic
31 geochronology. Zircon and monazite rims give “young” Cretaceous crystallisation ages,
32 and ages between samples and between plutons are within uncertainty of each other.
33 The magmatic zircon and monazite crystals record the Hf and Nd isotopic ratios of their
34 crustal sources and display a strikingly large range in ϵ_{Hf} (young = -8.2– -19.2) and ϵ_{Nd}
35 (young = -12.6 – -21.8). This heterogeneity is thought to be derived directly from the
36 heterogeneous source, and is further controlled by the extent of dissolution and the
37 preservation of inherited zircon and monazite. Isotopic data are consistent with

38 derivation of the OWPB Batholith from the ancient crust into which it intrudes, which is
39 spatially coincident with the inferred edge of Precambrian North America.

40 **2.2 - Introduction**

41 *In situ* analyses of the radiogenic tracer isotope and trace element composition
42 of accessory minerals at the sub-grain scale have proven to be effective tools for
43 understanding the origins and evolution of magmatic systems, with studies often
44 utilising multiple isotopic systems and minerals (Kemp et al., 2007; McFarlane &
45 McCulloch, 2007; Xie et al., 2008). Improvements in *in situ* analytical methods such as
46 SIMS (secondary ionisation mass spectrometry), LA-ICP-MS (laser ablation inductively
47 coupled plasma mass spectrometry) and LA-MC-ICP-MS (laser ablation inductively
48 coupled plasma multi collector mass spectrometry) have revealed details of magmatic
49 processes at increasingly finer temporal and spatial scales. The majority of these isotopic
50 studies have focused on zircon (Amelin et al., 2000; Harrison et al., 2005; Hawkesworth
51 & Kemp, 2004), where U-Pb geochronology is combined with O and Lu-Hf (and in some
52 case trace elements). The integration of these isotopic systems has proven to be a
53 powerful petrogenetic tool for studying both granitic rocks (Crowley et al., 2008) and
54 high grade metamorphic rocks (Schaltegger et al., 1999). Monazite-(Ce)
55 ($[Ce,La,Nd,Th]PO_4$) is also a useful tracer of crustal processes (Hawkins & Bowring, 1997;
56 Tomascak et al., 1998; Iizuka et al., 2011), but has not received near the amount of
57 attention as zircon. The potential to simultaneously measure U-Pb and tracer (e.g., Lu-Hf
58 and Sm-Nd) isotopes in zircon and monazite respectively by the laser ablation split

59 stream (LASS) method (Yuan et al., 2008; Fisher et al., 2014; Goudie et al., 2014) from
60 compositionally zoned accessory minerals allows for a high-resolution spatial and
61 temporal snapshot of crystallisation history, and avoids complications inherent in
62 sampling complexly zoned grains, as concomitant ages provide an effective means to
63 monitor inadvertent sampling of crystal domains which are not of interest (e.g.,
64 inherited domains, and younger overgrowths). This ability to resolve intra-crystalline
65 heterogeneity is an important tool for geoscientists as geological processes are sought
66 to be understood at ever smaller scales (Nemchin et al., 2013).

67 Due to its extensive exposure, the late Cretaceous Old Woman-Piute Batholith
68 (OWPB) in the Mojave Desert of southeastern California has served as an excellent
69 natural laboratory in which to understand the petrogenesis of continental arc granites
70 (Mittlefehldt & Miller, 1983; Miller et al., 1990; Wark & Miller, 1993). Three
71 peraluminous granitic plutons from this batholith were chosen for detailed study. The
72 Sweetwater Wash Pluton (SWP) is well characterised in terms of field relations
73 geochemistry (e.g., whole rock major, minor and trace elements, radiogenic tracer and
74 stable isotopes) (Mittlefehldt & Miller, 1983; Miller et al., 1990; Wark & Miller, 1993),
75 allowing for further detailed mineral-scale analysis. A preliminary study of monazite in
76 the SWP by Fisher et al. (in preparation) demonstrated the presence of significant
77 isotopic heterogeneity. The North Piute Pluton (NPP) and the Painted Rock Pluton (PRP),
78 both of similar age to the SWP, have received less attention, and so this study will act as
79 the first dedicated work on these plutons. These plutons will also provide useful

80 comparisons to the more extensive SWP and will allow potential heterogeneities in the
81 OWPB to be investigated at the batholith scale.

82 The current study aims to investigate scales of heterogeneity of the OWPB and
83 constrain its petrogenesis within a local and a regional context. Fieldwork involved
84 systematic sampling along a transect in the SWP allowing pluton-scale spatial and
85 temporal variations to be investigated via the records preserved in the chemistry of
86 accessory minerals. Samples were also collected from the NPP and PRP for comparison
87 with the SWP. We employ the combination of Lu-Hf isotopes in zircon and Sm-Nd
88 isotopes and REE in monazite, to obtain constraints on the petrogenesis of the SWP
89 through assessment of the degree of isotopic heterogeneity recorded in accessory
90 minerals. Most analyses reported were done using the LASS method, which allows
91 concurrent age analysis along detection of mixed domains and thus ensures that only
92 the crystal domain of the age of interest are considered. Understanding the mechanisms
93 responsible for producing the isotopic heterogeneity or homogeneity observed in the
94 OWPB will help constrain the petrogenesis of peraluminous plutons in general, as well as
95 provide important insights into monazite and zircon isotope systematics, crustal
96 evolution, and the fate of inherited accessory minerals under changing melt conditions.

97 **2.3 - Geological overview**

98 **2.3.1 - Regional geology**

99 The crust into which the OWPB intruded is long-lived and has a complex geologic
100 history. The oldest rocks exposed today are of Proterozoic age (1.8 to 1.7 Ga), but U-Pb
101 data for detrital and inherited zircon grains from Proterozoic supracrustal and intrusive
102 rocks and Mesozoic plutons document the existence of an older component in the
103 eastern Mojave Desert (very early Proterozoic to Late Archean, 2-3 Ga) (Wooden &
104 Miller, 1990; Kapp et al., 2002; Barth et al., 2009; Strickland et al., 2013). Sm-Nd model
105 ages from Proterozoic crystalline rocks also suggest the presence of 2.0-2.3 Ga crust
106 under the area (Bennett & DePaolo, 1987). Whole rock Pb isotopic compositions at 1.7
107 Ga are distinctive having high $^{207}\text{Pb}/^{204}\text{Pb}$ and very high $^{208}\text{Pb}/^{204}\text{Pb}$ relative to
108 $^{206}\text{Pb}/^{204}\text{Pb}$ (Wooden & Miller, 1990). This Nd and Pb isotopic character of the Eastern
109 Mojave Desert crust is distinct from similar Proterozoic provinces of North America,
110 probably reflecting input from Archean crust into Paleoproterozoic sedimentary
111 sequences and mantle-derived magmas (e.g., Bennett & DePaolo, 1987).

112 The oldest exposed rocks of the eastern Mojave Desert crust are immature
113 clastic metasedimentary rocks interpreted to have been derived from an adjacent arc
114 terrane and deposited 1.79-1.75 Ga (Barth et al., 2009; Strickland et al., 2013). This
115 supracrustal sequence was intruded by slightly younger mafic and granitic magmas and
116 then metamorphosed at upper amphibolite to granulite facies, migmatized, and

117 intruded by more granites in a series of events that lasted until ca. 1.67 Ga (Wooden &
118 Miller, 1990; Barth et al., 2009; Strickland et al., 2013).

119 Moderate volumes of granite were emplaced in the Mojave crust at ~1.4 Ga and
120 form part of the NE-SW trending “anorogenic” belt that runs from northern Europe,
121 through Labrador, across the eastern and southern United States, and and into
122 Southern California (Anderson, 1983). Siliciclastic and carbonate-dominated shelf
123 sedimentation occurred from the Neoproterozoic into the Cambrian recording the
124 change from a stable passive margin into a rifting phase, and then into the
125 establishment of passive margin sedimentation by the earliest Cambrian that continued
126 to the Permian and Triassic (Walker, 1988; Miller et al., 1990; Barth et al., 2009).

127 The OWPB is located to the east of the 0.706 $^{87}\text{Sr}/^{86}\text{Sr}$ line (Kistler, 1990), and
128 within a muscovite-granite belt that extends throughout the Cordillera (Figure 2.1a). This
129 geochemical boundary has been interpreted to represent either the margin of the
130 Proterozoic crust (Miller & Bradfish, 1980; Kistler, 1990), or alternatively, the western
131 edge of the North American lithospheric mantle (Miller et al., 2000). The strongly
132 peraluminous nature of much of the OWPB is in contrast to that of other Mesozoic
133 batholiths such as the Sierra Nevada and Peninsular Ranges, where muscovite-bearing
134 plutons are much less common.

135 Intense reactivation of the North American craton occurred in the Mesozoic
136 during the Sevier Orogeny and continued through the Laramide Orogeny (Livaccari,

137 1991). Plutonism in the Mojave began in the mid-Jurassic with the subduction of the
138 Farallon Plate under the North American Plate, expressed in the vicinity of the OWPB by
139 the emplacement of the synkinematic Clipper Mountains pluton at ~160 Ma and
140 abundant 145 Ma dikes (Miller & Wooden, 1994). As subduction continued into the
141 Cretaceous the tectonic style varied along the arc reflecting the complexities of oblique
142 convergence of the subducting slab. Contractual orogenic forces caused the formation
143 of the Fenner Shear zone to the east of the Piute Mountains, through which the ~85 Ma
144 East Piute pluton was emplaced (Karlstrom et al., 1993).

145 The major episode of magmatism in the Eastern Mojave occurred between 75-70
146 Ma, proposed to be due to the collapse of the inland orogenic belt after the tectonically
147 thickened crust encountered the strong lithosphere of the Colorado Plateau (Livaccari,
148 1991). During the Late Cretaceous two distinct types of magma were emplaced: earlier
149 metaluminous- to weakly peraluminous (MG) granodiorites and later peraluminous
150 granites (PG). These peraluminous and metaluminous intrusions account for ~85% of the
151 total exposed intrusive mass in the Mesozoic upper crust in the OWPB (Miller &
152 Wooden, 1994).

153 **2.3.2 - Nature of the Old Woman-Piute batholith**

154 The OWPB includes both of the Cretaceous magma series: the MG Old Woman
155 and Goffs plutons and the strongly PG Sweetwater Wash (SWP), Painted Rock (PRP),
156 North Piute (NPP), and Lazy Daisy plutons (Figure 2.1b). The peraluminous granites,
157 which are the focus of this study, occur in discrete plutons and show the temporal

158 sequence muscovite-biotite granite → muscovite-biotite-garnet granite → muscovite-
159 garnet granite → aplite and pegmatite (Mittlefehldt & Miller, 1983). Peraluminous
160 granitoid rocks are uniformly felsic (70-76 wt. SiO₂) with sodic plagioclase > K-feldspar.
161 Biotite is present in all but the most felsic aplites, becoming subordinate with evolution
162 and the appearance of garnet. Zircon and monazite are important accessory minerals,
163 both minerals being more abundant in the biotite-rich samples.

164 Regional tilting exposes deeper structural levels of the Old Woman batholith
165 towards the south. Roof contacts are typically sharp with injections of aplite/pegmatite
166 dikes being common. The PRP, which is completely enclosed by the Old Woman pluton,
167 encloses large blocks of the Old Woman granodiorite. At the cm-scale there is evidence
168 of interaction between the two rock types, possibly assimilation or mixing having
169 occurred. Dikes observed to cut the Old Woman pluton above the PRP may represent
170 feeder dikes for the shallower Sweetwater Wash pluton (Miller et al., 1990). Multiple
171 mineral barometers suggest that the NPP was emplaced at ~10 km and the SWP at
172 ~15km (Foster et al., 1992).

173 **2.3.3 - Previous work**

174 The SWP has been well characterised petrochemically. Whole rock major and
175 trace element analyses by Mittlefehldt & Miller (1983) show smooth geochemical
176 evolutionary trends that are consistent with fractional crystallisation of the observed
177 mineral assemblages. An increase in SiO₂ content between the 2-mica granite and the
178 aplite/pegmatite samples is accompanied by a decrease in Ba and Sr and an increase in

179 Rb, due to feldspar fractionation, while a decrease in LREE abundances is explained by
180 monazite fractionation.

181 *In situ* ion probe U-Pb analyses of zircon crystals from the Old Woman
182 granodiorite and Sweetwater Wash two-mica granite yield concordant analyses of 74 ± 3
183 Ma (2σ), and hornblende from the Old Woman granodiorite yields an age of 73 ± 2 Ma
184 (2σ) (Foster et al., 1989). The SWP granite was found to contain numerous inherited
185 zircon grains with ~50% of the zircon crystals showing anhedral Proterozoic cores and
186 thin magmatic Cretaceous rims with well-formed growth zoning revealed in
187 cathodoluminescence (CL) and back-scattered electron (BSE) imaging (Miller et al., 1992;
188 Hanchar & Miller, 1993). The dates for these inherited zircon cores span 1800-1100 Ma,
189 consistent with the eastern Mojave Desert crust as described above (Bennett & DePaolo,
190 1987). The presence of these inherited zircon cores in the SWP is one of the driving
191 forces behind using *in situ* techniques in accessory minerals such as zircon and monazite,
192 as inter- and intra-crystal variations can reveal important insights into crustal evolution
193 and magma chamber processes that otherwise cannot be resolved at the whole-rock or
194 whole-grain scale.

195 Further studies of the SWP have since investigated monazite and other accessory
196 minerals. Kingsbury et al., (1993) identified the presence of discordant inherited
197 monazite grains that record U-Pb dates of 1800-1700 Ma, consistent with dates from
198 inherited zircon crystals as described above (Foster et al., 1989). Wark & Miller (1993)
199 investigated monazite, zircon, and xenotime in order to trace the geochemical evolution

200 in the SWP as recorded in those accessory minerals. Differentiation of rock units from
201 granite to aplite is accompanied by flattening of REE patterns in monazite, increasing
202 concentrations of Hf and Y in zircon and a slight increase in Gd/Ho ratios in xenotime,
203 with U and Th increasing in each of the three phases. Accessory minerals also showed
204 well-developed compositional zonation patterns of Hf, U, Th and REE within grains that
205 reflect changing melt compositions with time.

206 The whole-rock major element, trace element and isotopic data presented in
207 Miller et al. (1990), Miller et al. (1992), and Miller & Wooden (1994) constrain the
208 petrogenesis of the two magma series present in the OWPB, with differences between
209 the metaluminous and peraluminous rock types being a function of source composition.
210 High $^{87}\text{Sr}/^{86}\text{Sr}$ (MG = 0.7095-0.7115 vs PG = 0.7014-0.719) and low ϵ_{Nd} (MG = -10 to -12
211 vs PG = -16 to -17) indicate major contributions from the Proterozoic crust. Assuming
212 that the magmas were entirely derived from Proterozoic crust, time averaged Rb/Sr
213 ratios for MG and PG rocks suggest a mafic-intermediate igneous source for the MG and
214 an intermediate-felsic igneous source for the PG series. This is also consistent with their
215 whole-rock $\delta^{18}\text{O}$ values that rule out dominant contributions from either the mantle or
216 sediments (e.g., $\delta^{18}\text{O} = 7.2$ to $9.3\text{\textperthousand}$). Similarly, the high Rb and Ba contents of MG rocks
217 also precludes derivation from a solely mantle source, while the low Rb/Ba of PG rocks
218 rules out a dominantly supracrustal pelitic source.

219 A suite of lower-crustal xenoliths from a Tertiary dike found in the North Piute
220 Mountains have Pb, Sr and Nd compositions that are consistent with derivation from a

221 Proterozoic Mojave crust (Miller et al., 1992; Hanchar et al., 1994). Major and trace
222 elements and radiogenic isotopic characteristics of the xenoliths suggest they represent
223 the depleted residue (i.e., restite) after extraction of felsic melt. This Proterozoic Mojave
224 crust is deemed to be heterogeneously composed of intermediate to felsic igneous rocks
225 as well as diverse clastic sedimentary rocks. Lower crustal xenoliths collected locally
226 contain zircon populations indicative of both igneous and sedimentary protoliths and
227 contain zircon overgrowths of ~75 Ma which is suggestive of a close relationship with
228 these similar age granites (C.M. Fisher & J.M. Hanchar, unpublished results). Modelling
229 of this extracted melt yields compositions that are consistent with that of OWPB
230 granitoids, however calculated melt fractions are variable (0-70%) and must have led to
231 diverse melt compositions.

232 **2.3.4 - Sample descriptions**

233 Sample locations are shown in Figure 2.1b and 2.1c and coordinates are given in
234 Table 2.1. Six SWP samples were collected following a ~7km transect from SW-NE that
235 included both garnet-poor and garnet-bearing varieties (Figure 2.1c) as well as an
236 unmapped outcrop of aplite/pegmatite. Two PRP samples were taken within 200m of
237 each other and again included garnet-poor and garnet-bearing varieties. Three NPP
238 samples were taken 500m apart to investigate potential lateral changes along the roof
239 section of the batholith. All NPP samples are 2-mica granites.

240 Three types of peraluminous rock types occur in the OWPB, and are largely
241 independent of pluton type. The most abundant lithology is the two-mica granite that is

242 ubiquitous in each of the three plutons. The unit is largely equigranular, and is
243 composed of quartz, plagioclase, K-feldspar (plagioclase > K-feldspar), biotite and
244 muscovite, representing the least evolved granite facies. A more evolved garnet-bearing
245 granite exists in the SWP where it is extensive enough to be mapped (Figure 2.1c), and in
246 the PRP where it has a variable distribution. Garnets are up to 1mm in size and are
247 sporadic in distribution but abundant when they are present, often occurring as sub-cm
248 clusters in the PRP. Aplite-pegmatite dikes occur in the SWP and represent the most
249 chemically differentiated unit. This unit is biotite-free but garnet-bearing, and the aplite
250 sampled has a heterogeneous texture, varying between “sugary” texture aplite, to fine-
251 grained (mm-scale) granite, to cm-scale feldspar megacrystic pegmatite. A petrological
252 summary of the samples is given in Table 2.1.

253 **Table 2.1 –Location and petrological summary of OWPB samples.**

Sample	Pluton	Coordinates		Rock type
SWP-12-01	Sweetwater Wash	N34° 33' 30.9"	W115° 12' 43.2"	2-mica granite
SWP-12-02		N34° 32' 59.1"	W115° 14' 3.7"	2-mica granite
SWP-12-03		N34° 32' 35.1"	W115° 15' 03.6"	Garnet-bearing 2-mica granite
SWP-12-04		N34° 35' 01.6"	W115° 10' 54.8"	2-mica granite
SWP-12-05		N34° 36' 01.5"	W115° 10' 57.4"	2-mica granite
SWP-13-01		N34° 34' 45.3"	W115° 10' 36.7"	Garnet bearing aplite, no biotite
PRP-12-01	Painted Rock	N34° 31' 06.2"	W115° 06' 56.8"	Garnet bearing 2-mica granite
PRP-13-01		N34° 31' 07.5"	W115° 07' 03.8"	2-mica granite
NPP-12-01	North Piute	N34° 50' 45.5"	W115° 01' 15.1"	2-mica granite
NPP-12-02		N34° 50' 45.5"	W115° 01' 15.1"	2-mica granite
NPP-13-01		N34° 50' 31.0"	W115° 01' 26.2"	2-mica granite

254

255 **2.4 - Analytical Methods**

256 All samples collected were analyzed for whole-rock major and trace elements,
 257 radiogenic isotopes (e.g., Sr, Sm-Nd, and Lu-Hf) and *in situ* monazite and zircon isotopic
 258 analysis (U-Pb and Sm-Nd, and U-Pb and Lu-Hf). Weathered material was removed by
 259 sawing. The samples were then processed using a jaw crusher, disk mill, and tungsten
 260 carbide shatter box to produce the pulverized material for geochemical analyses. Major
 261 and trace elements were analysed from rock powders at Activation Laboratories Ltd.,

262 Ontario, Canada. Sm, Nd, Lu-Hf and Sr were separated from whole-rock powders by
263 conventional column chemistry techniques. Subsequent isotopic analysis of Sm, Nd and
264 Sr was done by ID-TIMS (Isotope Dilution Thermal Ionisation Mass Spectrometry), with
265 Lu and Hf analysed by MC-ICP-MS, all at Memorial University.

266 Zircon and monazite grains were separated from the crushed material after the
267 disk mill step with the material sieved to retain the size fractions less than 500 µm and
268 greater than 63 µm, using standard heavy liquid and Frantz magnetic separation.
269 Monazite and zircon grains were then hand-picked in ethanol under a binocular
270 microscope, cast in epoxy resin, and then polished to reveal the crystal centres. They
271 were then imaged with BSE (zircon and monazite) and CL (zircon) imaging techniques
272 using the Quanta 400 scanning electron microscope at the CREAT MAF-IIC, Memorial
273 University of Newfoundland. A subset of monazite grains were then qualitatively
274 analysed by EPMA to produce elemental X-ray maps. The EPMA analyses were done
275 using a Jeol JXA-8230 at the Memorial University of Newfoundland CREAT TERRA EPMA-
276 SEM facility with operating conditions of at 15 kV, 250 nA, 0.5 µm step increments, with
277 a dwell time per step of 200 milliseconds.

278 All *in situ* analyses were done using LA-ICP-MS and LA-MC-ICPMS techniques.
279 Zircon U-Pb analyses were done at Portsmouth University. Dated grains were then
280 analysed on the same analysis locations used for U-Pb by Lu-Hf at Washington State
281 University (WSU). Monazite U-Pb and Sm-Nd analyses were done using the LASS method
282 at WSU. Additional U-Pb and Lu-Hf zircon LASS analyses were also done at WSU on

283 grains not previously dated by LA-ICPMS. This is summarised in Table 2.2. Only details of
284 the LASS methodology will be presented here. Details of all other analytical techniques
285 are provided in Appendix A along with analyses of standards done to assess accuracy
286 and precision of data in Appendix B.

287 **Table 2.2 – Summary of radiogenic isotopic analyses done on OWPB samples.**

Sample	Whole Rock			<i>In situ</i>		
	Sm-Nd	Sr	Lu-Hf	Zircon	Monazite	
	TIMS MUN	TIMS MUN	MC-ICP-MS MUN	U-Pb & Lu-Hf LA-ICP-MS UoP & WSU	LASS WSU	LA-ICP-MS LASS WSU
SWP-12-01	X	X	X	X		X
SWP-12-02	X	X	X	X		X
SWP-12-03	X	X	X	X		X
SWP-12-04	X	X	X	X		X
SWP-13-01	X	X	X	X	X	X
PRP-12-01	X	X	X	X	X	X
PRP-13-01	X	X	X	X		X
NPP-12-01	X	X	X	X		X
NPP-12-02	X	X	X	X		X
NPP-13-01	X	X	X	X		X

288 **Notes:** TIMS = Thermal Ionisation Mass Spectrometry, MC-ICP-MS = Multi-collector
289 Inductively-Coupled Mass-Spectrometry, LA-ICP-MS = Laser-Ablation Inductively-
290 Coupled Mass-Spectrometry, LASS = Laser Ablation Sprit Stream. MUN = Memorial
291 University of Newfoundland, UoP = University of Portsmouth, WSU = Washington State
292 University.

293 **2.4.1 - LASS method**

294 This study will also serve as the first dedicated investigation into both monazite
295 and zircon in magmatic systems using the laser ablation split stream (LASS) technique.
296 The recently developed LASS method involves the simultaneous determination of U-Pb
297 and Lu-Hf isotopes in zircon (Yuan et al., 2008; Fisher, et al., 2014) and U-Pb and Sm-Nd
298 isotopes simultaneously in monazite (Goudie, et al., 2014). The ablated sample material
299 is split into two streams as it exits the ablation cell and U-Pb isotopes are measured by a
300 magnetic sector high resolution (HR) ICP-MS and Sm-Nd or Lu-Hf isotopes are measured
301 by a multicollector (MC-ICP-MS). This method allows for accurate determinations of
302 initial isotopic compositions by using corresponding the U-Pb dates. A further advantage
303 of the LASS approach is that it allows a robust method of detecting mixed age analyses,
304 which are possible in cases where multiple generations of growth are present in a single
305 crystal. This is especially important in this study as monazite and zircon grains often have
306 complex zoning patterns that reflect different isotopic compositions, and it is imperative
307 that the tracer isotopes are measured in the same spot as the U-Pb analyses. If, for
308 example, two age components are present in an analysis, sampling both components
309 simultaneously will yield a discordant result and lie on a mixing line between the two
310 ages on a conventional Concordia diagram. Non-split-stream methods involve the
311 determination of U-Pb isotopes first, followed by analysis of tracer isotopes, which does
312 not allow detection of multiple components in the trace isotope analysis. Further, the
313 relatively small spot sizes (20-30 µm) used in this study also help to overcome, but not

314 eliminate completely, this complex zonation problem (Goudie, et al., 2014; Fisher, et al.,
315 2014).

316 All monazite samples and some zircon samples were analysed using the LASS
317 technique at Washington State University. A New Wave 213nm Nd:YAG laser was used
318 to ablate the sample, which is carried from the laser cell using He, as well as N₂ in order
319 to increase the sensitivity and minimize oxide formation. The ablated sample is split
320 using a baffled “Y” connector and transported by Tygon tubing to the Element 2 HR-ICP-
321 MS where U-Pb isotopes are measured, and the Neptune MC-ICP-MS where Sm and Nd
322 or Lu and Hf isotopes are measured (Figure 2.2). The relative elemental concentrations
323 of Ce, Eu and Gd were also simultaneously measured in monazite using the MC-ICP-MS.
324 The laser was operated at 8Hz, ~7J/cm², with a spot size of 20 µm for monazite LASS
325 analyses, and in both zircon Lu-Hf analyses and LASS analyses the laser operated at 10
326 Hz and a fluence of ~8 – 10 J/cm³, using a 30-40µm spot size.

327 The operating parameters and data reduction scheme for the *in situ* LASS
328 analyses follow that presented in (Goudie et al., 2014; Fisher et al., 2014) and are
329 summarised in Appendix A. This also includes information regarding the isobaric
330 interference corrections applied (Yb correction for Hf data, and Sm correction for Nd
331 data).

332 **2.5 - Results**

333 **2.5.1 - Major and trace element geochemistry**

334 Whole rock major, minor and trace element geochemistry data for the OWPB
335 samples are presented in Table 2.3. Granitoids show a restricted range from
336 leucogranite to high-silica granite, with SiO₂ ranging from 71-76% (Figure 2.3). Harker
337 plots show consistent trends with increasing silica, with 2-mica granite samples having
338 the lowest SiO₂ content and the aplite sample having the highest. Al₂O₃, CaO, MgO,
339 Fe₂O₃, TiO₂, Ba and Sr all decrease in concentration with increasing silica, as do La/Lu
340 and Zr/Hf. Rb shows an increase in concentration as silica increases.

341 Chondrite-normalised rare earth element (REE) patterns of the OWPB granitoids
342 broadly correlate with the mineralogy of each sample (Figure 2.4). Two-mica granite
343 samples show a “typical” granitic pattern, with light rare earth element (LREE)
344 enrichment and low heavy rare earth element (HREE) concentrations. With evolution
345 towards the garnet-bearing granite samples and the aplite sample LREE contents
346 decreases, there is a flattening in the LREE slope, and HREE contents increases. All
347 samples show a negative Eu anomaly, which increases as SiO₂ content increases towards
348 the aplite sample. With evolution of the melt it is also observed that overall REE
349 contents decreases.

350 **Table 2.3 – Whole rock major and trace element data for the OWPB samples.**

Sample	SWP-12-01	SWP-12-02	SWP-12-03	SWP-12-04	SWP-12-05	SWP-13-01	PRP-12-01	PRP-13-01	NPP-12-01	NPP-12-02	NPP-13-01
Rock Type	2 mica	2 mica	Garnet	2 mica	2 mica	Aplite	Garnet	2 mica	2 mica	2 mica	2 mica
SiO₂	71.81	75.1	74.12	72.16	71.52	76.68	75.62	73.96	72.37	73.6	74.05
Al₂O₃	14.61	14.2	13.71	14.72	14.26	13.73	13.42	13.3	14.56	14.34	14.2
Fe₂O₃	2.58	1.52	1.52	2.76	2.07	1.26	1.36	1.36	2.25	2.02	1.93
MnO	0.035	0.022	0.044	0.04	0.037	0.042	0.063	0.04	0.04	0.036	0.029
MgO	0.38	0.19	0.08	0.42	0.3	0.11	0.1	0.1	0.32	0.2	0.2
CaO	1.9	1.1	0.76	1.88	1.54	0.84	0.92	0.86	1.37	1.11	1.08
Na₂O	3.69	3.29	3.44	3.58	3.38	3.8	3.5	3.35	3.71	3.83	3.65
K₂O	3.75	4.85	4.57	3.77	3.94	3.85	4.61	4.73	3.89	3.87	4
TiO₂	0.187	0.092	0.039	0.216	0.17	0.048	0.057	0.067	0.166	0.157	0.16
P₂O₅	0.07	0.05	0.05	0.05	0.05	0.03	0.02	0.03	0.06	0.07	0.07
Rb	121	138	154	141	116	235	198	209	123	119	124
Sr	485	196	84	419	406	36	131	155	383	293	297
Ba	1376	728	252	1288	1329	53	470	588	1100	924	1005
Cs	2.5	2.3	1.6	3.5	1.3	1.8	2.6	2.5	0.9	2.2	1.6
Ta	3.59	3.72	3.21	5.83	2.81	5.57	3.33	4.16	3.21	3.23	3.49
Nb	9.7	14.9	11.7	15	8.9	31.7	18.4	19.2	13.9	15.4	10.2

351

352 **Table 2.3 (Continued)**

Sample	SWP-12-01	SWP-12-02	SWP-12-03	SWP-12-04	SWP-12-05	SWP-13-01	PRP-12-01	PRP-13-01	NPP-12-01	NPP-12-02	NPP-13-01
Tl	0.58	0.62	0.65	0.69	0.58	1.01	0.92	1.06	0.58	0.54	0.58
Pb	26	35	30	30	26	39	29	34	21	21	23
Hf	2.5	2.5	1.4	4.2	3	1.4	1.8	2.2	2.7	3	2.9
Zr	102	75	34	164	116	28	49	59	109	105	104
Y	7.4	19.9	15.1	17.7	12.1	39.8	24	35.1	11.1	16.9	11.8
Sc	3	4	4	5	3	6	4	5	2	3	3
U	1.04	2.05	2.31	2	0.99	4.72	2.84	2.83	0.94	1.61	0.82
Th	10.3	11	4.06	14.8	9.89	16.3	8.52	10.7	6.46	12.8	7.39
Ga	17	18	21	20	17	25	20	21	19	20	19
La	30	29.6	8.92	46.3	33.9	9.74	16.5	20	25.3	24.2	23.7
Ce	57.2	58.7	18.3	88.7	64.5	22.2	32.9	40.9	49.8	51.8	48.4
Pr	5.98	6.34	2.03	9.3	6.62	2.9	3.61	4.46	5.12	5.14	4.85
Nd	21.3	22.6	7.38	33.8	23.8	11.9	13.4	17.2	18.4	18.6	17.5
Sm	3.6	5.01	1.97	5.98	3.9	4.77	3.34	4.11	3.23	3.61	3.1
Eu	0.899	0.761	0.266	0.937	0.804	0.239	0.476	0.568	0.729	0.628	0.626
Gd	2.78	3.96	1.93	4.65	3.14	5.43	3.17	4.36	2.33	2.91	2.48
Tb	0.34	0.66	0.38	0.63	0.42	1.09	0.61	0.88	0.37	0.5	0.38

353

354 **Table 2.3 (Continued)**

Sample	SWP-12-01	SWP-12-02	SWP-12-03	SWP-12-04	SWP-12-05	SWP-13-01	PRP-12-01	PRP-13-01	NPP-12-01	NPP-12-02	NPP-13-01
Dy	1.59	3.79	2.44	3.43	2.1	6.78	3.93	5.58	2.14	3.02	2.11
Ho	0.27	0.73	0.5	0.63	0.4	1.39	0.84	1.15	0.4	0.6	0.4
Er	0.76	2.05	1.56	1.74	1.14	4.14	2.53	3.47	1.14	1.77	1.12
Tm	0.114	0.281	0.255	0.247	0.168	0.647	0.39	0.525	0.165	0.271	0.168
Yb	0.78	1.72	1.81	1.58	1.12	4.56	2.54	3.54	1.08	1.8	1.16
Lu	0.138	0.259	0.326	0.266	0.182	0.787	0.389	0.572	0.178	0.3	0.196
Zr/Hf	40.80	30.00	24.29	39.05	38.67	20.00	27.22	26.82	40.37	35.00	35.86
Rb/Sr	0.25	0.70	1.83	0.34	0.29	6.53	1.51	1.35	0.32	0.41	0.42
La/Lu	217.39	114.29	27.36	174.06	186.26	12.38	42.42	34.97	142.13	80.67	120.92

355 **Notes:** Oxides in wt%, trace elements in ppm.

356 **2.5.2 - Whole rock saturation temperature calculations**

357 Zircon saturation temperatures (T_{Zr}) were calculated according to Watson &

358 Harrison (1983),

359
$$T_{\text{Zr}} = 12900 / ([2.95 + 0.85M + \ln(496,000/Zr_{\text{melt}})])$$

360 Where M is the cation ratio $(\text{Na} + \text{K} + 2\cdot\text{Ca}) / (\text{Al}\cdot\text{Si})$ that takes into account the

361 effect of aluminosity and Si content on zircon saturation, and Zr_{melt} is the Zr content in

362 melt; when working with granites, whole-rock compositions are used as a proxy for melt

363 composition (see Miller et al., 2003, regarding limitations on interpretation of T_{Zr} based

364 on whole-rock granite compositions). A recent calibration by Boehnke et al. (2013) yields

365 temperatures that are generally lower by ~50°C for compositions like those of OWP

366 peraluminous granites. Whole-rock T_{Zr} for the OWPB samples using both Watson and

367 Harrison (1983) and Boehnke et al. (2013) models are presented in Table 2.4. In the text

368 that follows, we cite values calculated using Watson & Harrison as these temperatures

369 appear to be more geologically reasonable and consistent with monazite saturation

370 temperatures. Zircon saturation temperatures for our peraluminous granite samples

371 range from 664-793°C, with the more evolved aplite and garnet-bearing granites

372 showing the lowest temperatures.

373 Monazite saturation temperatures (T_{Mnz}) were calculated using the equation of

374 (Montel, 1993) whereby

375 $\ln(REE_t) = 9.50 + 2.34D + 0.3879\sqrt{H_2O} - \frac{13318}{T}$ where

376 $REE_t \sum \frac{REE_i \text{ (ppm)}}{\text{atomic weight (g mol}^{-1})}$ and

$$D = \frac{(Na + K + Li + 2Ca)}{Al} \cdot \frac{1}{(Al + Si)}$$

377 Na, K, Li, Ca, Al, Si are in atomic %; H₂O is in wt. %. The REE considered are from

378 La to Gd, excluding Eu. Water contents here are estimated to be 6%, which is deemed

379 reasonable for differentiated granites (Montel, 1993). Water content is thought to only

380 play a limiting role in the saturation temperature of monazite, however this effect is

381 important at low water contents, and it is thought to affect the rate of dissolution of

382 monazite (Rapp & Watson, 1986; Montel, 1993).

383 Monazite saturation temperatures range between 690-779°C (Table 2.4), a

384 similar range to that observed in zircon. In general the samples with the hottest T_{Zr} also

385 have the hottest T_{Mnz}, T_{Mnz} is lower than T_{Zr}, with exceptions, and the difference

386 between saturation temperatures for both minerals in a given sample is between 0 and

387 27 °C. T_{Zr} and T_{Mnz} are broadly within 5% error of each other.

388

389 **Table 2.4 – Whole rock zircon (T_{Zr}) and monazite (T_{Mnz}) saturation temperatures for the OWPB samples.**

Sample	SWP-12-01	SWP-12-02	SWP-12-03	SWP-12-04	SWP-12-05	SWP-13-01	PRP-12-01	PRP-13-01	NPP-12-01	NPP-12-02	NPP-13-01
Zr (ppm)	102	75	34	164	116	28	49	59	109	105	104
M	1.37	1.27	1.24	1.34	1.29	1.22	1.30	1.30	1.28	1.26	1.24
T_{Zr} (°C) (a)	750	732	676	793	767	664	698	713	762	760	761
T_{Zr} (°C) (b)	699	681	617	748	720	604	641	657	714	714	714
Inheritance %	50	50	20	50	50	10	20	20	30	30	30
T_{Zr} (a) minus inheritance (°C)	697	681	660	735	712	656	682	696	733	731	732
H ₂ O (wt%)	6	6	6	6	6	6	6	6	6	6	6
Total REE	121	126	41	189	136	57	73	91	104	106	100
D	1.10	1.04	1.02	1.08	1.04	1.01	1.08	1.07	1.04	1.02	1.01
T_{Mnz} (°C)	735	750	663	779	757	690	698	718	735	739	736

390 **Notes:** (a) Zircon saturation temperatures calculated using calibration from Watson & Harrison (1983).

391 (b) Zircon saturation temperature calculated using calibration from Boehnke et al., (2013).

392 **2.5.3 - Whole-rock isotopes (Sr, Sm-Nd and Lu-Hf)**

393 Whole-rock Sr, Sm-Nd and Lu-Hf isotopic data are presented in Table 2.5 and
394 Figure 2.5. Initial $^{87}\text{Sr}/^{86}\text{Sr}$ (calculated for 70 Ma) is heterogenous, ranging from 0.71184 -
395 0.72338, with SWP-12-03 being an extreme outlier with $^{87}\text{Sr}/^{86}\text{Sr}_i = 0.73540$. This outlier
396 is a garnet-bearing granite and has the highest Rb/Sr elemental ratio.

397 Initial $^{143}\text{Nd}/^{144}\text{Nd}$ ratios show a relatively narrow range from 0.51160-0.51174,
398 with corresponding $\epsilon_{\text{Nd}i}$ values of (-14.9 - -17.2). Excluding the anomalous SWP-12-03
399 analysis, Sr and Nd show an inverse relationship; those with the lowest $^{87}\text{Sr}/^{86}\text{Sr}_i$ have
400 the highest $\epsilon_{\text{Nd}i}$ (Figure 2.5a).

401 Both Sr and Nd initial isotopic compositions from this study overlap with but
402 show a larger range than OWPB 2-mica granites from Miller et al. (1990) (Figure 2.5).
403 There is also good agreement with data from Fisher et al., (in preparation). Sample SW-1
404 is a 2-mica granite sample taken nearby to SWP-12-04, and NPG is a 2-mica granite from
405 the NPP, approximately 200m west of the NPP-12-01 and NPP-12-02 samples. In both
406 this study and Fisher et al., (in preparation) NPP has a less negative $\epsilon_{\text{Nd}i}$ than SWP (Figure
407 2.5)

408 Hf analyses yield a large range in ϵ_{Hfi} (-18.1 to -7.0) with initial $^{176}\text{Hf}/^{177}\text{Hf}$ ratios
409 ranging between 0.282228–0.282543. Hf data can be split into two groups that
410 correspond to rock type; the two garnet-bearing samples (SWP-12-03 and PRP-12-01)
411 have the most radiogenic initial isotope ratios compared to the two-mica granite

412 samples. The garnet-bearing aplite sample (SWP-13-01), however, plots in the same
413 range as the two-mica samples which have a narrow range in ϵ_{Hf} values, but are much
414 more variable in $^{87}\text{Sr}/^{86}\text{Sr}_i$ (Figure 2.5b) and ϵ_{Nd} values (Figure 2.5c).

415 **Table 2.5 – Whole rock Sm-Nd, Sr and Lu-Hf data for the OWPB samples.**

Sample	SWP-12-01	SWP-12-02	SWP-12-03	SWP-12-04	SWP-12-05	SWP-13-01	PRP-12-01	PRP-13-01	NPP-12-01	NPP-12-02	NPP-13-01
$^{87}\text{Rb}/^{86}\text{Sr}^*$ (1)	0.848	2.394	6.234	1.144	0.972	22.198	5.14	4.585	1.092	1.381	1.42
$^{87}\text{Sr}/^{86}\text{Sr}$	0.71919	0.72576	0.74160	0.71767	0.71510	0.74096	0.72069	0.71988	0.71302	0.71324	0.71325
$^{87}\text{Sr}/^{86}\text{Sr}_{\text{i}}$ (2)	0.71835	0.72338	0.73540	0.71653	0.71413	0.71888	0.71558	0.71532	0.71193	0.71186	0.71184
2σ	14	9	9	10	10	10	10	10	10	10	10
$^{147}\text{Sm}/^{144}\text{Nd}$	0.1038	0.1183	0.151	0.104	0.1001	0.1981	0.1343	0.1353	0.1024	0.107	0.1058
$^{143}\text{Nd}/^{144}\text{Nd}$	0.511708	0.511723	0.511828	0.511776	0.511766	0.511817	0.511770	0.511769	0.511821	0.511818	0.511818
$^{143}\text{Nd}/^{144}\text{Nd}_{\text{i}}(2)$	0.511660	0.511669	0.511759	0.511728	0.511720	0.511726	0.511709	0.511707	0.511774	0.511769	0.511770
2σ	8	10	7	8	7	7	7	8	7	7	7
ϵ_{Nd} (3)	-18.1	-17.8	-15.8	-16.8	-17.0	-16.0	-16.9	-17.0	-15.9	-16.0	-16.0
$\epsilon_{\text{Nd}_{\text{i}}}$ (3)	-17.3	-17.2	-15.4	-16.0	-16.2	-16.0	-16.4	-16.4	-15.1	-15.2	-15.2
2σ	0.3	0.3	0.3	0.3	0.3	0.3	0.3	0.3	0.3	0.3	0.3
$^{176}\text{Lu}/^{177}\text{Hf}$	0.01	0.015	0.029	0.008	0.009	0.05	0.013	-	0.015	0.012	-
$^{176}\text{Hf}/^{177}\text{Hf}$	0.282300	0.282260	0.282471	0.282316	0.282303	0.282369	0.282560	-	0.282271	0.282244	-
$^{176}\text{Hf}/^{177}\text{Hf}_{\text{i}}(2)$	0.282286	0.282240	0.282433	0.282306	0.282291	0.282303	0.282543	-	0.282251	0.282228	-
2σ	8	10	8	12	21	15	7		11	13	
ϵ_{Hf} (4)	-17.2	-18.6	-11.1	-16.6	-17.1	-14.7	-7.9	-	-18.2	-19.1	-
$\epsilon_{\text{Hf}_{\text{i}}}$ (4)	-16.1	-17.7	-10.9	-15.4	-15.9	-15.5	-7.0	-	-17.3	-18.1	-
2σ	0.5	0.5	0.5	0.6	0.8	0.7	0.5	-	0.6	0.6	-

416 **Notes:**417 (1) $^{87}\text{Rb}/^{86}\text{Sr}^*$ were measured using the method of Faure & Mensing (2005).418 (2) All initial compositions are calculated using an age of 70Ma. Decay constants used: $^{87}\text{Rb} \lambda = 1.42 \times 10^{-11}$ (Steiger & Jäger, 1977), $^{147}\text{Sm} \lambda = 6.539 \times 10^{-12}$ (Begemann et al., 2001), $^{176}\text{Lu} \lambda = 1.867 \times 10^{-11}$ (Söderlund et al., 2004).419 (3) ϵ_{Nd} values were calculated using the present day CHUR values of $^{143}\text{Nd}/^{144}\text{Nd} = 0.512630$ and $^{147}\text{Sm}/^{144}\text{Nd} = 0.1960$ (Bouvier et al., 2008).420 (4) ϵ_{Hf} values were calculated using the present day CHUR values of $^{176}\text{Hf}/^{177}\text{Hf} = 0.282785$ and $^{176}\text{Lu}/^{177}\text{Hf} = 0.0336$ (Bouvier et al., 2008).

423 **2.5.4 - Accessory mineral characterisation**

424 Due to chemical zonation that is inherent in zircon and monazite complete
425 characterisation of the internal morphology of these minerals is crucial in order to guide
426 *in situ* analyses. A combined approach utilising BSE for monazite and zircon, CL for zircon
427 (Hanchar & Miller, 1993), and EPMA X-ray elemental maps for monazite (Williams et al.,
428 2007) were used in order to fully describe zonation in these complex accessory minerals.

429 ***2.5.4.1 - Zircon morphology***

430 Figure 2.6 shows the range of zircon morphologies observed in the OWPB
431 samples. Zircon grains range in shape from thin acicular morphologies to stubbier
432 tabular shapes. Zircon grains are typically 100-200µm but can be as small as 75µm and
433 as large as 450µm.

434 Grain morphology is linked to zonation style; acicular zircon with aspect ratios of
435 ~5:1 typically have fine scale igneous growth zoning (Figure 2.6a), whereas more tabular
436 and equant grains are more likely to contain large rounded core regions surrounded by
437 rims (Figure 2.6b). Rim regions vary in size between thin overgrowths of <10 µm to those
438 large enough to be analysed ~40 µm, up to 100 µm in large grains. Many crystals show
439 multiple “rims”, that is, differently coloured growth zoned rims that surround rounded
440 inherited cores (Figure 2.6c-d). Sector zoning is also observed (Figure 2.6e) in some
441 zircon grains. Core regions in the interior of the grains are irregularly shaped and often
442 show embayments where zircon has been resorbed in the new melt (Figure 2.6f). Cores

443 are also typically dark in BSE with rims being lighter, and where zones are dark in BSE
444 they are light in CL (Figure 2.6g). CL images reveal the growth zoning best, with fine
445 banding being less than 10µm wide. Colour changes (i.e., changes in chemistry when the
446 zircon was growing) observed in CL also suggests numerous periods of growth, or
447 discontinuous growth. Where possible, large enough different colour bands within a
448 single zircon were preferentially selected for U-Pb and Lu-Hf analysis. The rims are often
449 inclusion-rich, particularly when rims are light in BSE, with cores containing sparse but
450 larger inclusions (all being <10 µm). Inclusions are mainly composed of apatite or thorite
451 (brighter than zircon in BSE).

452 There are some noticeable differences between the zircon crystals separated
453 from different samples in this study. Samples from the SWP contain more “inherited”
454 cores than NPP, with the least inheritance observed in the PRP. Quantifying the amount
455 of inheritance in a sample however is problematic, due to sampling bias when picking for
456 larger zircon grains that are more likely to contain inherited cores (which as noted above
457 typically have larger surface area for the rims which makes them preferable for the La-
458 ICP-Ms and LA-MC-ICP-MS analyses). These cores are also assumed to be inherited
459 based on zircon texture, but without U-Pb dating this assumption must be taken with
460 caution.

461 **2.5.4.2 - Monazite morphology**

462 Figure 2.7 shows the range of monazite morphologies observed in the OWPB
463 samples. Monazite crystals are typically equant to prismatic in morphology and are 150-

464 200µm in length, though the sizes range from between 50- to 300µm. Crystals tend to
465 be larger in the SWP > PRP > NPP samples.

466 Monazite crystals from the OWPB show a range of zonation styles and will be
467 classified here according to the scheme outlined in Catlos (2013). Many grains show
468 weak zoning, with BSE showing no greyscale intensity contrast (Figure 2.7a). Patchy
469 zonation is a common feature with irregular areas showing a difference in brightness
470 (Figure 2.7b). More regular brightness contrasts are often observed near cracks, or
471 where previous cracks could be interpreted to have annealed, giving rise to a veining
472 texture (Figure 2.7c). Many crystals show simple zoning involving single cores,
473 sometimes with embayments, and single rims (Figure 2.7d), whereas others show
474 concentric, oscillatory (Figure 2.7e) and sector growth zoning. Monazite crystals from
475 sample SWP-13-01 are distinctive in that they only show oscillatory zonation.

476 The monazite grains are often inclusion rich, occurring in both core and rim
477 regions and inclusion trails are common (Figure 2.7f). Inclusions are more abundant and
478 inclusion trails are particularly common in the PRP and NPP samples. Inclusion size varies
479 between sub-micron size up to 50µm. Inclusions are typically composed of acicular
480 needles of zircon or rounded and irregular apatite. Allanite inclusions were also
481 observed.

482 A small number of monazite crystals from the SWP samples show bright, Th-rich
483 regions, but these themselves do not have a consistent morphology (Figure 2.8). Some

484 crystals comprise distinct yet irregular bright core regions, with varying amounts of
485 inclusions in the core (Figure 2.8a-8d). Others show highly irregular small patches of Th-
486 rich areas (Figure 2.8b) whereas other grains have Th-rich regions that extend across
487 most of the crystal (Figure 2.8c).

488 X-ray maps of selected monazite grains show the relative abundance, and
489 variations, of element concentrations (Figure 2.9). X-ray element maps generally show
490 more variation than is visible in BSE images. The zoning in BSE appears to be primarily
491 controlled by variations in Y, Th and U; darker areas in BSE are typically low in Th and U
492 and Y versus lighter areas. Ca shows little intra-grain variation, however faint zonation
493 may be observed that cannot be observed in BSE. The same can be generally said for Nd.
494 However, for the grains where a discrete Th-rich core is observed it is accompanied by a
495 sharp increase in Nd concentration.

496 **2.5.5 - In situ data**

497 ***2.5.5.1 - Zircon U-Pb isotopes***

498 In total, *in situ* zircon U-Pb analyses yielded 185 concordant analyses, 152
499 analyses being done by U-Pb only methods and 34 analyses by the LASS method.
500 Concordia plots are shown in Figure 2.10a, and data tables are presented in Appendix C.
501 Two distinct age populations were identified from the OWPB samples, an “old”
502 Proterozoic population and a “young” Cretaceous population. All samples show evidence
503 of the inherited Proterozoic ages, although not all samples yield concordant old
504 analyses. Zircon rims range from 70-75 Ma based on $^{206}\text{Pb}/^{238}\text{U}$ ages (Figure 2.10b) with

505 weighted average $^{206}\text{Pb}/^{238}\text{U}$ ages for each of the samples being indistinguishable within
506 error. While there is little difference in weighted average ages within error between any
507 of the plutons, the NPP appears the oldest and the SWP is the youngest (NPP = $77.2 \pm$
508 1.9 Ma, PRP = 74.7 ± 1.4 Ma, SWP = 72.2 ± 1.0 Ma, 2σ). These calculated weighted
509 averages also have high MSWD values (typically >2). Concordant old inherited cores
510 yield $^{206}\text{Pb}/^{207}\text{Pb}$ ages that range from 1784 Ma to 1399 Ma, with a peak age of ~ 1700
511 Ma (Figure 2.10c).

512 **2.5.3.2 - Monazite LASS-U-Pb isotopes**

513 250 *in situ* monazite analyses were done using the LASS technique (data
514 presented in Appendix C). The young monazite analyses tend to plot along discordants on
515 Tera-Wasserburg plots (Figure 2.11a), suggesting some incorporation of common Pb, an
516 observation also made by Fisher et al., (in preparation). Similar to that observed in the
517 zircon data there is no distinction within error between crystallisation ages for samples
518 at the hand-sample or the pluton scale. Young monazite grains range in age from 68-75
519 Ma based on $^{206}\text{Pb}/^{238}\text{U}$ ages, with NPP again yielding the oldest $^{206}\text{Pb}/^{238}\text{U}$ weighted
520 average age (NPP = 74.8 ± 1.2 Ma, PRP = 68.4 ± 0.9 Ma, SWP = 70.7 ± 0.4 Ma, all 2σ)
521 (Figure 2.11b). Similarly to the zircon data, weighted averages for individual samples and
522 for each pluton yield ages with MSWD values generally >2 .

523 Young monazite crystallisation ages for a given sample are typically younger than
524 their corresponding zircon ages. This discrepancy is not systematic and differences vary
525 from between ~ 9 Ma to being indistinguishable within error.

526 Unlike the widespread inheritance observed in the zircon grains, only 4 monazite
527 analyses yield Proterozoic ages. Analyses from the inherited monazite cores plot near to
528 concordia on Tera-Wasserburg plots and give $^{207}\text{Pb}/^{206}\text{Pb}$ ages ranging from ~1700 to
529 1600 Ma (Figure 2.11c). This monazite inheritance is only observed in the 2-mica
530 granites of the SWP (samples SWP-12-01, SWP-12-04 and SWP-12-05).

531 **2.5.3.3 - Zircon Lu-Hf isotopes**

532 Two distinct populations of measured $^{176}\text{Hf}/^{177}\text{Hf}$ ratios are evident in the OWPB
533 samples, these corresponding to the age of the zircon components (Figure 2.12). Young
534 zircon grains have average $^{176}\text{Hf}/^{177}\text{Hf} = 0.282344 \pm 35$ (2σ) whilst old zircon grains have
535 average $^{176}\text{Hf}/^{177}\text{Hf} = 0.281844 \pm 35$ (2σ). $^{176}\text{Lu}/^{177}\text{Hf}$ ratios overlap with old samples
536 showing a more restricted range versus young samples, which range from ~0.001 –
537 0.0037 (average $2\sigma \pm 45$ (± 37 average 2σ)).

538 Young zircon Hf compositions calculated at 70Ma show a wide range in negative
539 crustal $\epsilon_{\text{Hf}}(70\text{Ma})$ signatures (-8.3 – -18.6). Old zircon grains have larger negative $\epsilon_{\text{Hf}(70\text{Ma})}$
540 values of -26.4 - -34.9. When compared at a pluton scale these ranges are slightly more
541 restricted in the PRP and NPP versus the SWP (Table 2.6).

542 **2.5.3.4 - Monazite LASS Sm-Nd isotopes**

543 The $^{147}\text{Sm}/^{144}\text{Nd}$ ratios of the OWPB monazite grains range from 0.0689 – 0.2179
544 (average $2\sigma \pm 0.0010$) with an overlap between the young and the old monazite.
545 Proterozoic monazite grains have lower $^{143}\text{Nd}/^{144}\text{Nd}$ ratios than the younger grains but

546 there is an overlap with the range observed for the young monazite grains (Figure
547 2.13a). Average initial ratios for old monazite grains is 0.510329 ± 76 , whereas young
548 zircon has an average $^{143}\text{Nd}/^{144}\text{Nd}_i = 0.511710 \pm 62$ (Figure 2.13b).

549 Similar to the zircon grains, young monazite grains show a range of negative
550 crustal $\epsilon\text{Nd}_{(70\text{ Ma})}$ signatures (-12.5 – -21.5). Old monazite grains also have negative
551 $\epsilon\text{Nd}_{(70\text{Ma})}$ values, ranging between -20.1 and -30.5. At the pluton scale, the NPP shows
552 the narrowest range of ϵ values (~4 epsilon units versus ~9 epsilon units for the PRP and
553 SWP) (Table 2.6).

554 **Table 2.6 – In situ isotopic ranges of OWPB zircon and monazite grains.**

			<u>Zircon ϵ_{Hf}</u> (70Ma)	<u>Monazite ϵ_{Nd}</u> (70Ma)
NPP	Young	Maximum	-10.4	-13.4
		Minimum	-17.2	-17.3
PRP	Old	Maximum	-28.6	-
		Minimum	-32.6	-
SWP	Young	Maximum	-9.6	-12.7
		Minimum	-17.8	-21.5
SWP	Old	Maximum	-30.3	-
		Minimum	-32.9	-
SWP	Young	Maximum	-8.3	-12.5
		Minimum	-18.6	-21.6
SWP	Old	Maximum	-26.4	-20.1
		Minimum	-34.9	-30.5

555

556 **2.5.3.5 - Monazite REE data**

557 In addition to analyses of Sm and Nd isotopes and elemental concentrations, the
558 LASS method allows the determination of Ce, Gd and Eu (Fisher et al., 2011; Goudie et
559 al., 2014). Ce/Gd versus Eu* (Figure 2.14a) shows a broadly positive correlation, with

560 monazite from the most evolved SWP-13-01 aplite sample showing the lowest Ce/Gd
561 and Eu* values. The four “old” monazite grains show relatively high Ce/Gd and relatively
562 low Eu* values, however there is overlap with the compositions of the “young” monazite
563 grains. As discussed above (Section 2.6.5.4) ϵ_{Nd_i} data shows two distinct populations
564 based on age, with the “young” monazite grains showing a large range in epsilon values.
565 There is also considerable range in Eu* (Figure 2.14b) and in Ce/Gd (Figure 2.14c). While
566 there is considerable overlap between the three plutons, monazite grains from NPP tend
567 to show higher Ce/Gd and Eu* values.

568 Trends observed above are in good agreement with *in situ* monazite REE data
569 from Fisher et al., (in preparation) (Figure 2.14). Monazite from the SW-1 and NPG
570 broadly overlap with the 2-mica data from the SWP and NPP respectively in ϵ_{Nd_i} , Ce/Gd
571 and Eu*, however Ce/Gd in sample NPG is shows a much larger range, reaching a
572 maximum of ~50.

573 **2.5 - Discussion**

574 **2.5.1 - Differentiation trends in an evolving magma**

575 The whole-rock composition of the OWPB samples reflects the mineralogy and
576 rock type of each sample, and the predictable geochemical trends represent an
577 evolution in melt composition (Figure 2.3). Depletion in Al, Ca, Ba and Sr at higher silica
578 contents is consistent with feldspar fractionation. The increase in Rb reflects the
579 increase in incompatible elements as crystallisation progressed. The decrease in Mg and

580 Fe are due to the crystallisation of biotite as temperature drops in the evolving melt.
581 Biotite is also removed from the melt due to the melt-crystal reaction of biotite + (Mn,
582 Al)-rich liquid → garnet + muscovite. This reaction is thought to be controlled by the Mn
583 content of in the melt (Miller & Stoddard, 1981). The decrease in La/Lu reflects
584 progressive crystallization of monazite, which strongly prefers LREE and therefore
585 depletes La contents of the melt while having little effect on Lu.

586 The low Zr/Hf ratio in the most silicic rocks is consistent with zircon fractionation.
587 Deviations from chondritic Zr/Hf ratios (~39) are characteristic of the most felsic,
588 evolved rocks and this is thought to be due to the crystallisation and removal of zircon,
589 the main reservoir of Zr and Hf in the crust (Claiborne et al., 2006). Although Hf
590 substitutes effectively for Zr in zircon and Hf concentrations are very high, Zr is favoured
591 over Hf in the zircon structure and therefore progressive crystallization results in
592 decreasing Zr/Hf (Claiborne et al., 2006; Colombini et al., 2011).

593 The whole rock REE behaviour during crystallisation of the OWPB samples (Figure
594 2.4) can be explained by the fractionation of certain mineral phases, and follows the
595 behaviour found by Mittlefehldt & Miller (1983) in their investigation of SWP rocks. The
596 LREE depletion between the 2-mica granites and the aplite sample can be explained by
597 monazite fractionation. The HREE enrichment seen in the differentiation sequence can
598 be explained by the crystallisation of garnet, which changes the behaviour of the HREE
599 from incompatible to compatible. The increase in magnitude of the negative Eu anomaly
600 as the melt evolves is due to the crystallisation of feldspar. Furthermore, the decrease in

601 Ce/Gd and Eu* with evolution (Figure 2.14a) recorded in the OWPB monazite crystals is
602 also consistent with the fractional crystallisation of monazite and feldspar, respectively
603 (Mittlefehldt and Miller, 1983).

604 **2.5.2 - Saturation temperatures**

605 The average T_{Zr} temperature of the two-mica granite samples is interpreted to be
606 the approximate temperature of melt generation ($\sim 755^{\circ}\text{C}$). The preservation of inherited
607 zircon grains and their textural characteristics (inherited cores are often rounded or
608 resorbed) in these samples indicate that the melt was Zr-saturated, or very near to Zr-
609 saturation at the source; otherwise the grains would have dissolved. The presence of
610 magmatic rims on inherited cores indicates that not all of the Zr contents in the rock is
611 from the melt fraction; therefore the T_{Zr} places an upper limit on the magma generation
612 temperature.

613 Using the CL and BSE images, supported by U-Pb ages, it is possible to visually
614 estimate the amount (i.e., volume) of inherited zircon in each sample and thus correct
615 the zircon saturation temperatures (Table 2.4). Corrected values account for between
616 50% inheritance for 2-mica granite samples and 10% inheritance for aplite samples. This
617 decreases zircon saturation temperatures by between 58°C and 7°C , respectively.

618 Conversely the aplite T_{Zr} ($\sim 665^{\circ}\text{C}$) represents the approximate solidus of the
619 magma. Aplites represent segregated melt fractions, and effective melt segregation
620 inhibits the entrainment of existing grains. The aplite sample (SWP-13-01) indeed

621 contains the lowest proportion of inherited grains (estimates at 10%; Table 2.4). This
622 suggests that most of the Zr present is in the melt, thus whole-rock Zr concentrations
623 best approximate the composition and therefore the minimum temperature of the
624 initially emplaced magma (Miller et al., 2003). This low temperature is also likely
625 influenced by the low Zr contents of this sample (28 ppm) due to prior zircon
626 fractionation.

627 If the same interpretations of T_{Mn_z} is made as that for T_{Zr} , that T_{Mn_z} of two-mica
628 granites reflects the approximate temperature of melt generation, then the two
629 thermometers are consistent in suggesting an initial melt temperature of between ~700-
630 750 °C. The amount of inherited monazite in the OWPB samples is negligible and thus
631 correction of T_{Mn_z} is not required. This temperature is broadly consistent with previous
632 estimates using the same whole-rock saturation thermometry (Kingsbury et al., 1993),
633 although the current study involves a wider range of rock types and also includes PRP
634 and NPP as part of the magmatic system. It is important to note, however, that these
635 calculated zircon and monazite saturation temperatures represent estimates that are
636 limited by the imprecise knowledge of melt compositions; that is, whole rock elemental
637 concentrations represent magmas that contain crystals as well as melt.

638 **2.5.3 - Whole rock radiogenic tracer isotopes**

639 The time-integrated initial tracer isotope ratios of the OWPB samples are
640 consistent with derivation from an old crustal source; high $^{87}\text{Sr}/^{86}\text{Sr}$, and strongly
641 negative ϵ_{Hf} and ϵ_{Nd} (Figure 1.5). The whole rock samples show strong isotopic

642 heterogeneity preserved at the batholith scale, with ϵ_{Nd} values show a $\sim 3\epsilon$ unit variation
643 while ϵ_{Hf} show a larger $\sim 11 \epsilon$ unit variation. This also suggests that the source may have
644 been heterogeneous. Although the garnet bearing samples have the highest ϵ_{Hf} (Figure
645 1.5b and 1.5c), as the garnet in these samples is magmatic (Miller & Stoddard, 1981) the
646 observed variation in ϵ_{Hf} is believed to be a function of the source composition when
647 the garnet formed.

648 The Hf-Nd terrestrial array can be generally described by the equation $\epsilon_{\text{Hf}} =$
649 $1.8 * \epsilon_{\text{Nd}}$ (Vervoort & Patchett, 1996; Vervoort & Blichert-Toft, 1999). Based on the OWPB
650 Nd isotopic data, ϵ_{Hf} values are much too radiogenic and should be approximately -25 to
651 -30. This disequilibrium between the Nd and Hf isotopic systems suggests that the
652 source region must contain a large portion of unreacted residual zircon, which can either
653 be retained at the source or entrained in the melt. The presence of abundant zircon
654 grains with old cores found in the xenoliths that are proposed to represent the residual
655 restite of the OWPB source (Miller et al., 1992; Hanchar et al., 1994; Fisher et al., in
656 preparation), and in the zircon grains from the OWPB granites suggests that residual
657 zircon was both retained and entrained.

658 **2.5.4 - U-Pb data**

659 The U-Pb dates from inherited zircon and monazite cores are consistent with
660 ages found in the Proterozoic crust into which the OWPB intrudes (See Section 2.3.1).
661 The range of ages preserved, from 1400-1800 Ma document a number of crustal
662 building events in the Mojave and indicate that the source material for the OWPB melts

663 had undergone multiple episodes of crustal modification and thus was diverse in
664 isotopic composition (Wooden & Miller, 1990; Barth et al., 2009; Strickland et al., 2013).

665 All “young” samples of both zircon and monazite give U-Pb dates of ~70-75 Ma.
666 This range is present at both sample-, pluton- and batholith-scale, precluding the
667 calculation of weighted mean ages or concordia ages with MSWD values close to 1.
668 Assigning such discrete crystallisation ages to magmatic systems is inconsistent,
669 however, with current models of incremental pluton emplacement (Paterson & Tobisch,
670 1992; Coleman et al., 2004; Glazner et al., 2004). High precision (<0.1%) CA-ID-TIMS
671 analyses (Mattinson, 2005) are increasingly revealing zircon populations within
672 individual hand samples that record multiple discrete pulses of zircon growth on the
673 order of 10^4 - 10^6 years (Coleman et al., 2004; Matzel et al., 2006; Miller et al., 2007;
674 Memeti et al., 2010; Schoene et al., 2012). At the lower precision of LA-ICP-MS U-Pb
675 geochronology (1-2% r.s.d.) such magmatic pulses are not resolvable, leading to what
676 appears to be a continuous range of ages. Furthermore, the ability for zircon to survive
677 multiple melt generation events often leads to diverse zircon populations that sample
678 preceding batches of melt, these zircon crystals being called “antecrysts” (Miller et al.,
679 2007). These fine temporal details of pluton growth, which are not the focus of this
680 study, can only be recovered using high precision analytical techniques.

681 **2.5.5 - Tracer isotope data**

682 ***2.5.5.1 - Zircon Lu-Hf isotope composition***

683 While there is considerable scatter in $^{176}\text{Lu}/^{177}\text{Hf}$ ratios, the $^{176}\text{Hf}/^{177}\text{Hf}$ ratios
684 define two populations that correspond to the age of each of the grains (Figure 2.10a).
685 Figure 2.10b shows that the “young” and “old” zircon grains formed in melts with two
686 different initial isotopic ratios, the “young” population growing in a melt with a higher,
687 more radiogenic $^{176}\text{Hf}/^{177}\text{Hf}$ composition. This indicates that the source of the
688 Cretaceous zircons was high in Lu/Hf.

689 **2.5.5.2 - Monazite Sm-Nd isotope composition**

690 Figure 2.11a shows the isotopic ratio data for the OWPB monazite crystals and is
691 similar to that of the zircon data presented in Figure 2.10a, in that there is considerable
692 scatter in the $^{147}\text{Sm}/^{144}\text{Nd}$ ratios. A 75 Ma “reference isochron” is plotted and the
693 isotopic evolution trend is consistent with monazite growth at 75 Ma but variation in
694 $^{143}\text{Nd}/^{144}\text{Nd}$ means this is not a true isochron. The “old” monazite grains however define
695 a linear array that is consistent with a 1700 Ma reference isochron (Figure 2.11a) (also
696 observed in Fisher et al., unpublished). While this isochron is defined by the four
697 inherited grains there are multiple analyses with compositions consistent with growth
698 along the 1700 Ma isochron. As these grains have been independently dated by U-Pb
699 geochronology it is possible to know which isochron the analysis is part of.

700 Initial $^{143}\text{Nd}/^{144}\text{Nd}$ ratios calculated for each monazite analysis (Figure 2.11b) are
701 calculated in the same way as that described for the $^{177}\text{Hf}/^{176}\text{Hf}$ in zircon, and show the
702 same trends; “young” grains are more radiogenic and formed in an isotopically different
703 melt versus the preserved “old” grains.

704 **2.5.6 - Epsilon-Time plots**

705 The isotopic compositions of zircon and monazite respectively at their time of
706 crystallisation, as well as the evolution trends of the inherited components preserved,
707 are shown Figure 2.15a and 2.15b. The oldest inherited zircon crystals, which formed at
708 ~1700-1800 Ma, have a juvenile (+ve) ϵ_{Hf} isotopic signatures, with those forming at
709 ~1400 Ma being less juvenile, and potentially derived from rocks similar to those of
710 1700-1800 Ma grains (Figure 2.15b and 2.15c). As the inherited monazite grains have
711 negative ϵ_{Nd} compositions and are therefore not juvenile, this suggests that the crust in
712 which they formed is older than the crystallisation age of the monazite grains. This is
713 consistent with the regional Nd isotopic signature found in the Mojave by Bennett &
714 DePaolo (1983).

715 There is a large divergence between the ϵ_{Hf} composition of magmatic zircon at
716 70-75Ma, which is between -8 and -20, and the expected ϵ_{Hf} composition of the “old”
717 zircon grains at this age is ~ -28 and -36 (Figure 2.15a). The preservation or dissolution of
718 t_1 residual minerals has a large effect on the composition of the minerals that form at t_2
719 (Figure 2.15c). If all residual minerals undergo dissolution at t_2 they will transfer their
720 isotopic composition to the magmatic mineral. If there isn’t complete dissolution of
721 residual minerals then there will be an offset between the composition that the
722 expected residual composition and that of the magmatic mineral. The isotopic
723 composition of the t_2 magmatic minerals will lie in the region between the compositions
724 of the whole rock granite and the residual t_1 minerals. Undissolved residual minerals will

725 retain their t1 compositions (that have now developed a very negative epsilon value)
726 and can either be left behind at the source as restite or entrained in the new melt as
727 inherited grains. The offset observed in the OWPB zircon ϵ_{Hf} is therefore attributed to
728 the large amount of inherited zircon grains preserved.

729 The “old” monazite evolution trend however does overlap with the least
730 radiogenic magmatic monazite compositions at an ϵ_{Nd} of ~-21, suggesting that there is
731 isotopic inheritance, is limited, if present at all (Figure 2.15b). Furthermore, the ϵ_{Nd}
732 whole rock compositions of the OWPB granitoids only show a slight divergence from the
733 expected evolution of the Mojave Proterozoic crust (Bennett & DePaolo, 1987),
734 consistent with limited levels of inheritance. The Mojave Proterozoic crust is therefore a
735 suitable source of the ~1700Ma inherited monazite grains and a source of the granitic
736 melts at ~75Ma.

737 No whole rock Hf data are available for potential Mojave crustal sources. As
738 such, it is not possible to evaluate similar evolution trends in comparison with the zircon
739 data. Given the expected isotopic systematics, however, the source rock composition
740 can be estimated. Assuming that the “old” zircon cores retain the same initial
741 composition as the source rock they formed from, and by using a typical crustal
742 $^{176}\text{Lu}/^{177}\text{Hf} = 0.015$, crustal evolution trends can be calculated (Figure 15a). These
743 evolution trends calculated using initial compositions from both 1800 Ma and 1400 Ma
744 zircon crystals overlap with the range of Hf whole rock compositions observed in the

745 OWPB samples. This suggests that a crust with these compositions is a suitable source
746 for both the inherited zircon grains and for the 75 Ma granites.

747 The divergence in isotopic evolution between the composition of the whole rock
748 and that of the minerals as seen in in Figure 2.15c is also an effect of the
749 parent/daughter elemental ratios of the mineral in question. Zircon grains have low
750 Lu/Hf meaning there is little ingrowth of radiogenic Hf over time, and therefore ancient
751 zircon will preserve their initial Hf isotopic ratio and will diverge in composition away
752 from any new zircons formed at t2. In contrast, monazite contains sufficient Sm that
753 radiogenic Nd will form and the composition of monazite grains will “keep up” with any
754 isotopic variations in the surrounding crust, and produce a smaller divergence in mineral
755 compositions. This illustrates how the Hf isotopic system in zircon is a more sensitive
756 tracer of isotopic changes over time than Nd is in monazite.

757 **2.5.7 - Levels of isotopic heterogeneity in the OWPB**

758 There is considerable isotopic heterogeneity preserved in ~75Ma domains in
759 both Nd in monazite and Hf in zircon (Table 2.6). This heterogeneity in both systems
760 exists at the whole rock sample-, pluton- and batholith-scale, and appears to be
761 independent of age; the range of epsilon values observed in the inherited components is
762 comparable to that seen in the magmatic components. The complex and heterogeneous
763 nature of the crustal source material is further confirmed by the range of ages observed
764 in the U-Pb ages in both inherited monazite and zircon.

765 The preservation of isotopic heterogeneity in the inherited mineral components
766 suggests that the crustal source was heterogeneous at least at the mineral-scale. The
767 crust is known to have experienced multiple crustal building events during the
768 Proterozoic that have continuously modified the initial juvenile crust. This has then been
769 sampled by the inherited zircon grains. Analyses of the 1400 Ma anorogenic granites of
770 the Mojave by Goode & Vervoort (2006) are consistent with the data presented in this
771 study, in that by 1400 Ma there had been significant modification of the basement crust
772 that created a heterogeneous lower crust, and mantle input at this time, if present at all,
773 was minor.

774 It follows then that melting of an isotopically heterogeneous source could
775 produce isotopically heterogeneous granites. The Hf and Nd budget in felsic magmas will
776 be controlled mainly, by the dissolution of zircon and monazite respectively. The
777 composition of zircon and monazite formed in these magmas and the variability of these
778 components is then controlled by magma chamber processes. If the melt domains have
779 a high connectivity and the melt has the ability to mix and homogenise effectively then
780 any heterogeneity derived from the source will be overcome.

781 Depending on the efficiency or inefficiency of mixing, complete dissolution of a
782 diverse assemblage of minerals can result in either a homogeneous isotope composition
783 of all newly-crystallising minerals, or a range of compositions approximating the range of
784 the source composition, respectively. Partial dissolution and inefficient mixing will also

785 produce isotope heterogeneity as the isotopic budget is partitioned into two
786 components (Figure 2.15).

787 This lack of homogenisation between the various melts and the ability or the
788 source material to effectively transfer a large range of isotopic composition to these
789 melts has also been noted in other granitic rock. Similar findings by Villaros et al. (2012)
790 in the Pan-African Cape Granite Suite, and by Farina et al. (2014) in the Peninsular
791 Pluton, South Africa suggest that heterogeneity in granites can originate from the
792 source, and doesn't have to reflect the mixing of melts from different sources, a view
793 also presented by Clemens (2003), Clemens & Stevens (2012) and Tang et al., (2014). It is
794 suggested by this study then that a heterogeneous crust could have produced a
795 heterogeneous melt that has further diversified due to the variable dissolution of
796 inherited components. As the OWPB source is well constrained and is consistent with
797 derivation from the Mojave Proterozoic crust with little to no mantle-derived input, this
798 study is an excellent test of this model.

799 **2.5.8 Petrogenesis of the OWPB**

800 Of the three plutons sampled, the NPP exhibits the most homogeneous
801 composition, particularly in "young" monazite ϵ_{Nd_i} values (Table 2.6); a 4 epsilon unit
802 range versus 9 epsilon units for both PRP and SWP. Textural observations supported by
803 *in situ* U-Pb data suggest that the NPP contains the least amount of zircon inheritance.
804 Assuming that all three plutons are derived from the same source (albeit a seemingly

805 heterogeneous one) the difference in levels of heterogeneity at the pluton-scale must be
806 ascribed to magma chamber processes. Of the three plutons studied the NPP is the
807 smallest in size, is at the present day shallowest structural level, and appears to be the
808 oldest (although U-Pb data is not indistinguishable with confidence and higher precision
809 TIMS U-Pb data are needed to date the zircon rims). A possible model of petrogenesis
810 therefore is that the NPP represents the first partial melt(s) of the lower crust that
811 ascended to shallower levels. Given the precision of the U-Pb data collected in this study
812 it is not possible to determine how many discrete batches of melt formed the NPP, but
813 the uniformity of the unit in the field and the lack of more evolved garnet-bearing units
814 may suggest that only small volumes of compositionally homogenous melt(s) were
815 emplaced. The small size of the pluton would enable a more thorough mixing of melts,
816 promoting the dissolution of inherited grains in under-saturated conditions.
817 Subsequently, larger volumes of melt were produced in the lower crust that could not
818 ascend to depths as shallow as the NPP. These melts formed the PRP, SWP and other
819 plutons of the OWPB and were likely emplaced incrementally. Over time these batches
820 became more geochemically evolved, creating garnet-bearing batches of melt. These
821 larger volumes were not able to mix efficiently, thus creating the isotopic heterogeneity
822 observed in the accessory minerals.

823 **2.5.8 - Inheritance and growth of accessory minerals**

824 Monazite inheritance is thought to be a rare phenomenon (Copeland et al., 1988;
825 Parrish, 1990, Crowley et al., 2008) and certainly in the OWPB, zircon inheritance is

826 much more abundant than monazite. While old zircon core regions are often somewhat
827 rounded with truncated growth zoning, deep embayments are rare, and core regions
828 can retain a subhedral shape upon which a young rim will grow epitaxially on the
829 inherited core. This is in contrast to the inherited monazite core regions. Two of these
830 grains (Figure 2.8a & 2.8d) have irregular cores that show clear evidence of partial
831 dissolution. The other two grains (Figure 2.8b & 2.8c), however, show a much more
832 patchy and diffuse core region respectively. These textures and the difference in amount
833 of inheritance between zircon and monazite are indicative of the saturation state of the
834 melt (i.e., temperature, composition) with respect to monazite and zircon, and that the
835 rate of dissolution and growth was different for both minerals.

836 In zircon, it appears that while some dissolution did occur when the old grain was
837 entrained in the new melt during the Cretaceous, growth of the new young zircon was
838 faster than the rate of dissolution. The presence of resorbed cores indicates that the
839 melt was slightly undersaturated in zircon when it formed, and is also linked to the
840 temperature: when the magma was at a higher temperature more zircon could dissolve.
841 Conversely, the monazite inherited from the old crust was not in equilibrium with the
842 melt that formed from it, this melt being largely undersaturated with respect to
843 monazite. When the melt was emplaced the “old” monazite underwent rapid
844 dissolution, and a large proportion of the ancient monazite was destroyed.

845 When the melt becomes saturated with regard to zircon and monazite,
846 dissolution of the inherited grains ceases and there is subsequent growth of “young”

847 zircon and monazite domains. Note that these saturation levels need not necessarily be
848 attained at the same time. Indeed using OWPB U-Pb data, the observation that monazite
849 yields slighter younger ages than zircon from the same sample does suggest that
850 monazite saturation was reached after zircon saturation. A similar linkage between
851 zircon and monazite saturation and their ages has also been suggested by Kelsey et al.
852 (2008)

853 In our model of mineral growth these “young” zircon and monazite domains are
854 thought to grow freely in a melt when mineral saturation has been attained. Texturally,
855 the “young” zircon and monazite is consistent with magmatic growth (Figures 2.6-2.9
856 and Section 2.5.4). Where the new crystal has nucleated around an inherited grains that
857 have not fully undergone dissolution (i.e., Ostwald coarsening, Watson et al., 1989) to
858 form a rim, the boundary between the “old” and “young” crystal domains is always
859 sharp. This contact is effectively a mineral scale “chemically eroded” unconformity
860 between the inherited and new mineral. Where there is not an inherited grain upon
861 which a new crystal can nucleate, the new crystals show similar magmatic zonation
862 patterns to the new rims.

863 The chemical contrast between “old” and “young” domains observed in both the
864 X-ray maps (Figure 9) and the *in situ* data (Figures 12, 13 & 15) are also consistent with
865 magmatic growth. The presence of two distinct age and isotope populations in both
866 minerals confirms that the “young” magmatic domains grew in a melt of differing
867 composition to that of the “old” inherited domains.

868 An alternative model for the “young” mineral growth, which we do not prefer, is
869 growth via a replacement mechanism. In other examples where inherited monazite has
870 been observed (namely Hawkins & Bowring (1997) and Crowley et al., (2008)) the
871 younger monazite domains have been explained by secondary alteration due to fluid-
872 mineral interaction with the pre-existing monazite. The mechanism implied, although
873 not explicitly mentioned, in these studies is “simultaneous dissolution re-precipitation”,
874 and has been invoked as the mechanism behind many replacement reactions in natural
875 systems (Putnis, 2002; Putnis, 2009; Putnis & Ruiz-Agudo, 2013). When a mineral is in
876 disequilibrium with a fluid, re-equilibration will occur in order to reduce the Gibbs free
877 energy of the system. This is thought to involve the energetically favourable
878 simultaneous dissolution of the original mineral and the precipitation of the new mineral
879 that is in equilibrium with the fluid. This replacement mechanism progresses inwards
880 from the grain boundary and outer regions of the crystals and produces sharp
881 boundaries both texturally and compositionally.

882 The evidence for this secondary alteration in the Hawkins & Bowring (1997) and
883 Crowley et al., (2008) studies are the sharp contacts between primary and secondary
884 domains, the presence of patchy zonation in the secondary domains, and the variable
885 composition of these domains from EPMA data. While sharp contacts are observed in
886 the OWPB monazite grains, the simple oscillatory zoning textures observed are clearly
887 inconsistent with the replacement mechanism of mineral growth.

888 **2.6 - Conclusions**

889 1) The OWPB was emplaced at ~750-700 °C at ~70-75 Ma and differentiated via

890 fractional crystallisation, consistent with the mineral assemblage observed.

891 2) The range of U-Pb ages possibly suggests incremental growth of the batholith

892 by several batches of coalescing magma and repeated cycles of fractionation, but

893 distinct ages of crystallization cannot be confidently resolved by the LA-ICP-MS

894 technique.

895 3) The source of the OWPB is suggested to be the underlying Mojave Proterozoic

896 crust into which the batholith intrudes. Inherited zircon and monazite grains

897 found in the OWPB granites yield U-Pb ages from ~1800- 1400 Ma, and have Nd

898 isotopic signatures that are consistent with derivation from this crust.

899 4) This source region is indicated by inherited zircon Hf compositions to be

900 heterogeneous. This isotopic characteristic was directly transferred to the

901 Cretaceous melts via dissolution at the source, contributing to the resulting

902 heterogeneity observed in the Cretaceous zircon domains.

903 5) Variable dissolution of inherited components is also suggested to result in the

904 heterogeneity observed in both zircon Hf and monazite Nd compositions. The

905 preservation of this heterogeneity indicates that the melts that formed the

906 OWPB did not successfully homogenise.

907 6) The NPP is the most homogenous of the three plutons studied and may
908 represent the first, small volume melts that formed in the Cretaceous. The
909 subsequent melts that formed the PRP and SWP were more heterogeneous, and
910 experienced more extensive geochemical evolution, producing the wider range
911 of granitic compositions observed.

912 **2.7 - Acknowledgements**

913 Thanks to Anne Westhues, Sherri Strong, and Rebecca Lam for their assistance
914 with sample preparation and analytical work at Memorial University of Newfoundland.
915 Thanks also to the analytical staff at the University of Portsmouth and Washington State
916 University. Thanks to Jean-Marc Montel for providing assistance with monazite
917 saturation temperature calculations. SEP thanks friends and colleagues at Memorial
918 University for helpful discussions and support and to Charles Knack at WSU for help
919 during the analytical work. Research supported by an NSERC Discovery Grant to JMH,
920 the Department of Earth Sciences of Memorial University of Newfoundland, and a
921 Mineralogical Society of America Grant for Student Research in Mineralogy and
922 Petrology to SEP.

2.8 - References

- Amelin, Y., Lee, D-C., Halliday, A.N., 2000. Early-middle Archaean crustal evolution deduced from Lu–Hf and U–Pb isotopic studies of single zircon grains. *Geochimica et Cosmochimica Acta*, 64, pp. 4205-4225.
- Anderson, J. L., 1983. Proterozoic anorogenic granite plutonism of North America. *Geological Society of America Memoir*, 161, pp. 133-154.
- Barth, A. P., Wooden, J. L., Coleman, D. S. & Marilyn B. Vogel, 2009. Assembling and Disassembling California: A Zircon and Monazite Geochronologic Framework for Proterozoic Crustal Evolution in Southern California. *The Journal of Geology*, 117(3), pp. 221-239.
- Begemann, F., Ludwig, K.R., Lugmair, G.W., Min, K., Nyquist, L.E., Patchett, P.J., Renne, P.R. Shih, C.-Y., Villa, I.M., & Walker, R.J., 2001. Call for an improved set of decay constants for geochronological use. *Geochimica et Cosmochimica Acta*, 65, pp. 111-121.
- Bender, E. E., 2008. Petrogenesis of the Fenner Gneiss, Piute and Old Woman Mountains, San Bernardino County, California, *Geological Society of America Abstracts with Programs*, 40, pp. 250.

Bennett, V. C. & DePaolo, D. J., 1987. Proterozoic crustal history of the western United States as determined by neodymium isotopic mapping. Geological Society of America Bulletin, 99, pp. 674-685.

Black, L.P., Gulson, B.L., 1978. The age of the Mud Tank carbonatite, Strangways Range, Northern Territory. BMR Journal of Australian Geology and Geophysics, 3, 227–232

Blichert-Toft, J., 2008. The Hf isotopic composition of zircon reference material 91500. Chemical Geology, 253, pp. 252-257.

Boehnke, P., Watson, E.B., Trail, D., Harrison, T.M., & Schmitt, A.K. (2013) Zircon saturation re-revisited. Chemical Geology, 351, pp. 324–334.

Bouvier, A., Vervoort, J. D. & Patchett, P. J., 2008. The Lu-Hf and Sm-Nd isotopic composition of CHUR: Constraints from unequilibrated chondrites and implications for the bulk composition of terrestrial planets. Earth and Planetary Science Letters, 273, pp. 48-57.

Burchfiel, B. C. & Davis, G. A., 1981. The Geotectonic development of California. In: W. G. Ernst & W. W. Rubey, eds., Prentice-Hall, pp. 217-252.

Carl, B. S. & Miller, C. F., 1991. Western Old Woman Mountains shear zone: Evidence for late ductile extension in the Cordilleran orogenic belt. Geology, 19, pp. 893-896.

Catlos, E. J., 2013. Versatile Monazite: resolving geological records and solving challenges in materials science: Generalizations about monazite: Implications for geochronologic studies. *American Mineralogist*, 98, pp. 819-832.

Chang, Z., Vervoort, J. D., McClelland, W. C. & Knaack, C., 2006. U-Pb dating of zircon by LA-ICP-MS. *Geochemistry, Geophysics, Geosystems*, 7, pp. Q05009.

Cherniak, D., 2010. Diffusion in Accessory Minerals: Zircon, Titanite, Apatite, Monazite and Xenotime. In Y. Zhang and D.J. Cherniak, Eds., *Diffusion in Minerals and Melts*, *Reviews in Mineralogy and Geochemistry*, 72, pp. 827-869.

Cherniak, D. J. & Watson, E. B., 2003. Diffusion in Zircon. *Reviews in Mineralogy and Geochemistry*, 53, pp. 113-143.

Claiborne, L. L., Miller, C.F., Walker, B.A., Wooden, J.L., Mazdab, F.K., & Bea, F., 2006. Tracking magmatic processes through Zr/Hf ratios in rocks and Hf and Ti zoning in zircons: An example from the Spirit Mountain batholith, Nevada. *Mineralogical Magazine*, 70, pp. 517-543.

Claiborne, L.L., Miller, C.F., Flanagan, D.M., Clyne, M.A., Wooden , J.L., 2010a. Zircon reveals protracted magma storage and recycling beneath Mount St. Helens. *Geology*, 38, pp. 1011–1014.

Claiborne, L.L., Miller, C.F., Wooden, J.L., 2010b. Trace element composition of igneous zircon: a thermal and compositional record of the accumulation and evolution of a

large silicic batholith, Spirit Mountain, Nevada. Contributions to Mineralogy and Petrology, 160, pp. 511–531.

Corfu, F., Hanchar, J.M., Hoskin, P.W.O. and Kinny, P. (2003) Atlas of zircon textures. In: J.M. Hanchar and P.W.O. Hoskin, Eds. *Zircon. Reviews in Mineralogy & Geochemistry*, 53, pp 469-500.

Coleman, D. S., Gray, W. & Glazner, A. F., 2004. Rethinking the Emplacement and Evolution of Zoned Plutons: Geochronologic Evidence for Incremental Assembly of the Tuolumne Intrusive Suite, California. *Geology*, 32, pp. 433–6.

Colombini, L.L., Miller, C.F., Gualda, G.A.R., Wooden, J.L., & Miller, J.S., 2011. Sphene and zircon in the Highland Range volcanic sequence (Miocene, southern Nevada, USA): elemental partitioning, phase relations, and influence on evolution of silicic magma. *Mineralogy and Petrology*, 102, pp. 29-50.

Copeland, P., Parrish, R.R., & Harrison, T.M., 1988. Identification of inherited radiogenic Pb in monazite and its implications for U-Pb systematics. *Nature*, 333 (23), pp.760-763.

Cressey, G., Wall, F. & Cressey, B. A., 1999. Differential REE uptake by sector growth of monazite. *Mineralogical Magazine*, 63, pp. 813-828.

Crowley, J. L., Brown, R. L., Gervais, F. & Gibson, H. D., 2008. Assessing Inheritance of Zircon and Monazite in Granitic Rocks from the Monashee Complex, Canadian Cordillera. *Journal of Petrology*, 49, pp. 1915-1929.

Dunning, G., Macdonald, A. & Barr, S., 1995. Zircon and monazite U-Pb dating of the Doi Inthanon core complex, northern Thailand: implications for extension within the Indosinian Orogen. *Tectonophysics*, 251, pp. 197-213.

Faure, G. & Mensing, T., 2005. *Isotopes: principles and applications*. 3rd ed., John Wiley & Sons, 897 pp..

Farina, F., Stevens, G., Gerdes, A., & Frei, D., 2014. Small-scale Hf isotopic variability in the Peninsula pluton (South Africa): the processes that control inheritance of source $^{176}\text{Hf}/^{177}\text{Hf}$ diversity in S-type granites. *Contributions to Mineralogy and Petrology*, 168, pp. 1065.

Fisher, C. M., Hanchar, J.M., Samson, S.D., Dhuime, B., Blichert-Toft, J., Vervoort, J.D., & Lam, R., 2011. Synthetic zircon doped with hafnium and rare earth elements: A reference material for *in situ* hafnium isotope analysis. *Chemical Geology*, 286, pp. 32-47.

Fisher, C. M., McFarlane, C.R.M., Hanchar, J.M., Schmitz, M.D., Sylvester, P.J., Lam, R., & Longerich, H.P., 2011. Sm-Nd isotope systematics by laser ablation-multicollector-inductively coupled plasma mass spectrometry: Methods and potential natural and synthetic reference materials. *Chemical Geology*, Volume 284, pp. 1-20.

Fisher, C.M., Vervoort, J.D. and Hanchar, J.M., 2012. Split-stream laser ablation microanalysis: U-Pb age and Lu-Hf isotopic composition of complexly zoned zircon crystals from the ancient zircon record. Abstract V12A-03 presented at 2012 Fall Meeting, AGU, San Francisco, Calif., 3-7 Dec.

Fisher, C. M., Vervoort, J. D. & DuFrane, S. A., 2014. Accurate Hf isotope determinations of complex zircons using the "laser ablation split stream" method. *Geochemistry, Geophysics, Geosystems*, 15, pp. 121-139.

Foster, D. A., Harrison, T. M. & Miller, C. F., 1989. Age, Inheritance, and Uplift History of the Old Woman-Piute Batholith, California and Implications for K-Feldspar Age Spectra. *The Journal of Geology*, 97, pp. 232-243.

Foster, D. A., Harrison, T. M., Miller, C. F. & Howard, K. A., 1990. The $^{40}\text{Ar}/^{39}\text{Ar}$ thermochronology of the eastern Mojave Desert, California, and adjacent western Arizona with implications for the evolution of metamorphic core complexes. *Journal of Geophysical Research: Solid Earth*, 95, pp. 20005-20024.

Foster, D. A., Miller, C. F., Harrison, T. M. & Hoisch, T. D., 1992. $^{40}\text{Ar}/^{39}\text{Ar}$ thermochronology and thermobarometry of metamorphism, plutonism, and tectonic denudation in the Old Woman Mountains area, California. *Geological Society of America Bulletin*, 104, pp. 176-191.

Goodge, J.W., & Vervoort, J.D., 2006. Origin of Mesoproterozoic A-type granites in Laurentia: Hf isotope evidence. *Earth and Planetary Science Letters*, 243, pp. 711-731.

Goudie, D. J., Fisher, C.M., Hanchar, J.M., Crowley, J.L., & Ayers, J.C., 2014. Simultaneous *in situ* determination of U-Pb and Sm-Nd isotopes in monazite by laser ablation ICP-MS. *Geochemistry, Geophysics, Geosystems*, 15, pp. 2575-2600.

Glazner, A. F., Bartley, J. M., Coleman, D. S., Gray, W. M. & Taylor, R. Z., 2004. Are plutons assembled over millions of years by amalgamation from small magma chambers? *Geological Society of America Today*, 14 , pp. 4–11.

Hanchar, J.M. & Miller, C.F., 1993. Zircon zonation patterns as revealed by cathodoluminescence and backscattered electron images: Implications for interpretation of complex crustal histories. *Chemical Geology*, Volume 110, pp. 1-13.

Hanchar, J. M., Miller, C.F., Wooden, J.L., Bennett, V.C., & Staude, J.-M.G., 1994. Evidence from Xenoliths for a Dynamic Lower Crust, Eastern Mojave Desert, California. *Journal of Petrology*, 35, pp. 1377-1415.

Hanchar, J.M. & Rudnick, R., 1995. Revealing hidden structures: The application of cathodoluminescence and back-scattered electron imaging to dating zircons from lower crustal xenoliths. *Lithos* , 36, pp. 289-303.

Harrison, T. M., Blichert-Toft, J., Müller, W., Albarede, F., Holden, P., & Mojzsis, S.J.,

2005. Heterogeneous Hadean hafnium: Evidence of continental crust at 4.4 to 4.5

Ga. *Science*, 310, pp. 1947–1950.

Hawkesworth, C. J., & Kemp, A.I.S., 2006. Using hafnium and oxygen isotopes in zircons

to unravel the record of crustal evolution. *Chemical Geology*, 226, pp. 144–162.

Hawkins, D. P. & Bowring, S. A., 1997. U-Pb systematics of monazite and xenotime: case

studies from the Paleoproterozoic of the Grand Canyon, Arizona. 127, pp. 87-103.

Hawkins, D. P. & Bowring, S. A., 1997. U-Pb systematics of monazite and xenotime: case

studies from the Paleoproterozoic of the Grand Canyon, Arizona. Contributions to

Mineralogy and Petrology, Volume 127, pp. 87-103.

Hu, Z., Liu, Y., Gao, S., Liu, W., Zhang, W., Tong, X., Lin, L., Zong, K., Li, M., Chen, H., Zhou,

L., & Yang, L., 2012. Improved *in situ* Hf isotope ratio analysis of zircon using newly

designed X skimmer cone and jet sample cone in combination with the addition of

nitrogen by laser ablation multiple collector ICP-MS. *Journal of Analytical Atomic*

Spectrometry, 27, pp. 1391-1399.

Ickert, R.B., Williams, I.S., Wyborn, D., 2010. Ti-in-zircon from the Boggy Plain zoned

pluton: implications for zircon petrology and Hadean tectonics. Contributions to

Mineralogy and Petrology, 162, pp. 447–461.

Iizuka, T., Eggins, S.M., McCulloch, M.T., Kinsley, L.P.J., Mortimer, G.E., 2011. Precise and accurate determination of $^{147}\text{Sm}/^{144}\text{Nd}$ and $^{143}\text{Nd}/^{144}\text{Nd}$ in monazite using laser ablation-MC-ICPMS. *Chemical Geology*, 282, pp. 45-57.

Iizuka, T., Nebel, O. & McCulloch, M. T., 2011. Tracing the provenance and recrystallization processes of the Earth's oldest detritus at Mt. Narryer and Jack Hills, Western Australia: An *in situ* Sm-Nd isotopic study of monazite. *Earth and Planetary Science Letters*, 308, pp. 350-358.

Jackson, S. E., Pearson, N. J., Griffin, W. L. & Belousova, E. A., 2004. The application of laser ablation-inductively coupled plasma-mass spectrometry to *in situ* U-Pb zircon geochronology. *Chemical Geology*, 211, pp. 47-69.

Jeffries, T. E., Fernandez-Suarez, J., Corfu, F. & Gutierrez Alonso, G., 2003. Advances in U-Pb geochronology using a frequency quintupled Nd:YAG based laser ablation system ($\lambda = 213$ nm) and quadrupole based ICP-MS. *Journal of Analytical Atomic Spectrometry*, 18, pp. 847-855.

Kapp, J.D., Miller, C.F., & Miller, J.S., 2002. Ireteba Pluton, Eldorado Mountains, Nevada; late, deep-source, peraluminous magmatism in the Cordilleran interior. *Journal of Geology*, 110, pp. 649–669.

Karlstrom, K. E., Miller, C. F., Kingsbury, J. A. & Wooden, J. L., 1993. Pluton emplacement along an active ductile thrust zone, Piute Mountains, southeastern California:

Interaction between deformational and solidification processes. Geological Society of America Bulletin, 105, pp. 213-230.

Kelsey, D. E., Clark, C. & Hand, M., 2008. Thermobarometric modelling of zircon and monazite growth in melt-bearing systems: examples using model metapelitic and metapsammitic granulites. Journal of Metamorphic Geology, 26, pp. 199-212.

Kemp, A. I. S. et al., 2007. Magmatic and Crustal Differentiation History of Granitic Rocks from Hf-O Isotopes in Zircon. Science, 315, pp. 980-983.

Kingsbury, J. A., Miller, C. F., Wooden, J. L. & Harrison, T., 1993. Monazite paragenesis and U-Pb systematics in rocks of the eastern Mojave Desert, California, U.S.A.: implications for thermochronometry. Chemical Geology, Volume 110, pp. 147-167.

Kistler, R. W., 1990. Two different lithosphere types in the Sierra Nevada, California. In: L. Anderson, ed. The Nature and Origin of Cordilleran Magmatism, Geological Society of America, Memoirs, pp. 271-281.

Košler, J., Forst, L. & Sláma, J., 2008. Spreadsheet-based data reduction for laser ablation ICP-MS. In: P. J. Sylvester, ed. Laser ablation in the Earth Sciences: Current practices and outstanding. Short Course Series 40, Mineralogical Association of Canada, Quebec, pp. 315-317.

Košler, J. & Sylvester, P. J., 2003. Present Trends and the Future of Zircon in Geochronology: Laser Ablation ICPMS In: J.M. Hanchar and P.W.O. Hoskin, Eds. *Zircon*. Reviews in Mineralogy & Geochemistry, 53, pp. 243-275.

Livaccari, R. F., 1991. Role of crustal thickening and extensional collapse in the tectonic evolution of the Sevier-Laramide orogeny, western United States. *Geology*, 19, pp. 1104-1107.

Ludwig, K., 2003. User's Manual for Isoplot 3.00, Berkeley, California.

MacLachlan, K., N. Rayner, G. Dunning, and C. Leugner (2004), New results and ideas from the Rottenstone Domain project, in Summary of Investigations 2004 [CD-ROM], Misc. Rep. 2004-4.2, 2, p. 21, Industry Resources, Saskatchewan Geological Survey, Saskatchewan, Canada.

Mattinson, J.M., 2005. Zircon U-Pb chemical abrasion (bCA-TIMSQ) method: Combined annealing and multi-step partial dissolution analysis for improved precision and accuracy of zircon ages. *Chemical Geology*, 220, pp. 47-66.

Matzel, J. E., Bowring, S. A. & Miller, R. B., 2006. Time scales of pluton construction at differing crustal levels: Examples from the Mount Stuart and Tenpeak intrusions, North Cascades, Washington. *Geological Society of America Bulletin*, 118, pp. 1412-1430.

McFarlane, C. & McCulloch, M., 2007. Coupling of in-situ Sm-Nd systematics and U-Pb dating of monazite and allanite with applications to crustal evolution studies.

Chemical Geology, Volume 245, pp. 45-60.

Memeti, V., Paterson, S.R., Matzel, J., Mundil, R., & Okaya, D.A., 2010. Magmatic lobes

as "snapshots" of magma chamber growth and evolution in large, composite batholiths: An example from the Tuolumne intrusion, Sierra Nevada, California.

Geological Society of America Bulletin, 122, pp. 1912-1931.

Miller, C. F. & Bradfish, L. J., 1980. An inner Cordilleran belt of muscovite-bearing plutons. Geology, 8, pp. 412-416.

Miller, C.F., Wooden, J. L., Bennett, V. C., Wright, J. E., Solomon, G. C., & Hurst, R. W., 1990. Petrogenesis of the composite peraluminous-metaluminous Old Woman-Piute range batholith, southeastern California: isotopic constraints. In: J. Anderson, ed, Geological Society of America Memoirs, pp. 99-109.

Miller, C. F., Hanchar, J.M., Wooden, J.L., Bennett, V.C., Harrison, M.T., Wark, D.A., & Foster, D.A., 1992. Source region of a granite batholith: evidence from lower crustal xenoliths and inherited accessory minerals. Earth and Environmental Science Transactions of the Royal Society of Edinburgh, 83, pp. 49-62.

Miller, C. F. & Wooden, J. L., 1994. Anatexis, hybridization and the modification of ancient crust: Mesozoic plutonism in the Old Woman Mountains area, California. Lithos, 32, pp. 111-133.

Miller, C. F., McDowell, S. & Mapes, R., 2003. Hot and cold granites: Implications of zircon saturation temperatures and preservation of inheritance. *Geology*, 31, pp. 529-532.

Miller, J. S., Glazner, A.F., Lang Farmer, G., Suayah, I.B., & Keith, L.A., 2000. A Sr, Nd, and Pb isotopic study of mantle domains and crustal structure from Miocene volcanic rocks in the Mojave Desert, California. *Geological Society of America Bulletin*, 112, pp. 1264-1279.

Miller, J.S., Matzel, J.E.P., Miller, C.F., Burgess, S.D., & Miller, R.B., 2007. Zircon growth and recycling during the assembly of large, composite arc plutons. *Journal of Volcanology and Geothermal Research*, 167, pp. 282-299.

Mittlefehldt, D. W. & Miller, C. F., 1983. Geochemistry of the Sweetwater Wash Pluton, California: Implications for "anomalous" trace element behavior during differentiation of felsic magmas. *Geochimica et Cosmochimica Acta*, 47, pp. 109-124.

Montel, J.-M., 1993. A model for monazite/melt equilibrium and application to the generation of granitic magmas. *Chemical Geology*, 110, pp. 127-146.

Nemchin, A. A., Horstwood, M. S. A. & Whitehouse, M. J., 2013. High-Spatial-Resolution Geochronology. *Elements*, 9, pp. 31-37.

Paces, J. B. & Miller, J. D., 1993. Precise U-Pb ages of Duluth Complex and related mafic intrusions, northeastern Minnesota: Geochronological insights to physical, petrogenetic, paleomagnetic, and tectonomagmatic processes associated with the 1.1 Ga Midcontinent Rift System. *Journal of Geophysical Research*, 98, pp. 13997-14013.

Parrish, R.R., 1990. U-Pb dating of monazite and its application to geological problems. *Canadian Journal of Earth Science*, 27, pp. 1431-1450.

Patchett, P. & Tatsumoto, M., 1981. A routine high-precision method for Lu-Hf isotope geochemistry and chronology. *Contributions to Mineralogy and Petrology*, 75, pp. 263-267.

Paterson, S. R. & Tobisch, O. T. 1992. Rates of processes in magmatic arcs; implications for the timing and nature of pluton emplacement and wall rock deformation. *Journal of Structural Geology* 14, pp. 291–300.

Putnis, A., 2002. Mineral replacement reactions: from macroscopic observations to microscopic mechanisms. *Mineralogical Magazine*, 66, pp. 689-708.

Putnis, A., 2009. Mineral replacement reactions. In: Oelkers, E. H. & Schott, J. Eds., *Thermodynamics and Kinetics of Water-Rock Interaction*. *Reviews in Mineralogy and Geochemistry*, 70, pp. 87-124.

Putnis, C.V., & Ruiz-Agudo, E., 2013. The mineral-water interface: Where minerals react with the environment. *Elements*, 9, pp.177-182.

Raczek, I., Jochum, K. P. & Hofmann, A. W., 2003. Neodymium and Strontium Isotope Data for USGS Reference Materials BCR-1, BCR-2, BHVO-1, BHVO-2, AGV-1, AGV-2, GSP-1, GSP-2 and Eight MPI-DING Reference Glasses. *Geostandards Newsletter*, 27, pp. 173-179.

Rapp, R. P. & Watson, E. B., 1986. Monazite solubility and dissolution kinetics: implications for the thorium and light rare earth chemistry of felsic magmas. 94, pp. 304-316.

Rehkämper, M. & Hofmann, A., 1997. Recycled ocean crust and sediment in Indian Ocean MORB. *Earth and Planetary Science Letters*, 147, pp. 93-106.

Schaltegger, U., Fanning, C.M., Günther, D., Maurin, J.C., Schulmann, K., & Gebauer, D., 1999. Growth, annealing and recrystallization of zircon and preservation of monazite in high-grade metamorphism: conventional and in-situ U-Pb isotope, cathodoluminescence and microchemical evidence. *Contributions to Mineralogy and Petrology*, Volume 134, pp. 186-201.

Scherer, E.E., Cameron, K.L., & Blichert-Toft, J., 2000. Lu-Hf garnet geochronology: closure temperature relative to the Sm-Nd system and the effects of trace mineral inclusions. *Geochemica et Cosmochimica Acta*, 64, pp. 3413-3432.

- Schoene, B., Crowley, J.L., Condon, D.J., Schmitz, M.D., & Bowring, S.A., 2006. Reassessing the uranium decay constants for geochronology using ID-TIMS U-Pb data. *Geochimica et Cosmochimica Acta*, 70, pp. 426-445.
- Schoene, B., Schaltegger, U., Brack, P., Latkoczy, C., Stracke, A., & Günther, D., 2012. Rates of magma differentiation and emplacement in a ballooning pluton as recorded by U-Pb TIMS-TEA, Adamello batholith, Italy. *Earth and Planetary Science Letters*, 355-356, pp. 162-173.
- Schoene, B., Condon, D.J., Morgan, L., & Mclean, N., 2013. Precision and Accuracy in Geochronology. *Elements*, 9, pp. 19-24.
- Seydoux-Guillaume, A.-M., Goncalves, G., Wirth, R., & Deutsch, A., 2003. Transmission electron microscope study of polyphase and discordant monazites: Site-specific specimen preparation using the focused ion beam technique. *Geology*, 31, pp. 973.
- Sláma, J., Košler, J., Condon, D.J., Crowley, J.L., Gerdes, A., Hanchar, J.M., Horstwood, M.S.A., Morris, G.A., Nasdala, L., Norberg, N., Schaltegger, U., Schoene, B., Tubrett, M.N., & Whitehouse, M.J., 2008. Plešovice zircon - A new natural reference material for U-Pb and Hf isotopic microanalysis. *Chemical Geology*, 249, pp. 1-35.
- Söderlund, U., Patchett, P., Vervoort, J. D. & Isachsen, C. E., 2004. The ^{176}Lu decay constant determined by Lu-Hf and U-Pb isotope systematics of Precambrian mafic intrusions. *Earth and Planetary Science Letters*, 219, pp. 311-324.

Steiger, R. & Jäger, E., 1977. Subcommission on geochronology: Convention on the use of decay constants in geo- and cosmochronology. *Earth and Planetary Science Letters*, 36, pp. 359-362.

Strickland, A., Wooden, J.L., Mattinson, C.G., Ushikubo, T., Miller, D.M., & Valley, J.W., 2013. Proterozoic evolution of the Mojave crustal province as preserved in the Ivanpah Mountains, southeastern California. *Precambrian Research*, 224, pp. 222-241.

Tanaka, T., Togashi, S., Kamioka, H., Amakawa, H., Kagami, H., Hamamoto, T., Yuhara, M., Orihashi, Y., Yoneda, S., Shimuzu, H., Kunimaru, T., Takahashi, K., Yanagi, T., Nakano, T., Fujimaki, H., Shinjo, R., Asahara, Y., Tanimizu, M., & Dragusanu, C., 2000. JNdI-1: a neodymium isotopic reference in consistency with La Jolla neodymium. *Chemical Geology*, 168, pp. 279-281.

Tang M., Wang X.-L., Shu X.-J., Wang D., Yang T., & Gopon P., 2014. Hafnium isotopic heterogeneity in zircons from granitic rocks: Geochemical evaluation and modeling of “zircon effect” in crustal anatexis. *Earth and Planetary Science Letters*, 389, pp. 188–199.

Tomascak, P. B., Krogstad, E. J. & Walker, R. J., 1996. U-Pb Monazite Geochronology of Granitic Rocks from Maine: Implications for Late Paleozoic Tectonics in the Northern Appalachians. *The Journal of Geology*, 104, pp. 185-195.

Tomascak, P. B., Krogstad, E. J. & Walker, R. J., 1998. Sm-Nd isotope systematics and the derivation of granitic pegmatites in southwestern Maine. *The Canadian Mineralogist*, 36, pp. 327-337.

Townsend, K. et al., 2001. Low temperature replacement of monazite in the Ireteba granite, Southern Nevada: geochronological implications. *Chemical Geology*, 172, pp. 95-112.

Vervoort, J. D. & Blichert-Toft, J., 1999. Evolution of the depleted mantle: Hf isotope evidence from juvenile rocks through time. *Geochimica et Cosmochimica Acta*, 63, pp. 533-556.

Vervoort, J. D. & Jonathan Patchett, P., 1996. Behavior of hafnium and neodymium isotopes in the crust: Constraints from Precambrian crustally derived granites. *Geochimica et Cosmochimica Acta*, 60, pp. 3717-3733.

Vervoort, J. D., Patchett, P. J., Söderlund, U. & Baker, M., 2004. Isotopic composition of Yb and the determination of Lu concentrations and Lu/Hf ratios by isotope dilution using MC-ICPMS. *Geochem. Geophys. Geosyst.*, 5, pp. Q11002.

Villaros, A., Buick, I.S., & Stevens, G., 2011. Isotopic variations in S-type granites: an inheritance from a heterogeneous source? *Contributions to Mineralogy and Petrology*, 163, pp. 243-257.

Wark, D. A. & Miller, C. F., 1993. Accessory mineral behavior during differentiation of a granite suite: monazite, xenotime and zircon in the Sweetwater Wash pluton, southeastern California, U.S.A. *Chemical Geology*, 110, pp. 49-67.

Watson, E. B. & Harrison, T. M., 1983. Zircon saturation revisited: temperature and composition effects in a variety of crustal magma types. *Earth and Planetary Science Letters*, 6, pp. 295-304.

Watson, B.E., Vicenzi, E.P., & Rapp, R.P. 1989. Inclusion/host relations involving accessory minerals in high-grade metamorphic and anatetic rocks. *Contributions to Mineralogy and Petrology*, 101 , pp. 220-231.

Wiedenbeck, M., Allé, P., Corfu, F., Griffin, W.L., Meier, M., Oberli, F., Von Quadt, A., Roddick, J.C., & Spiegel, W., 1995. Three Natural Zircon Standards for U-Th-Pb, Lu-Hf, Trace Element and REE Analyses. *Geostandards Newsletter*, 19, pp. 1-23.

Williams, M. L. & Jercinovic, M. J., 2012. Tectonic interpretation of metamorphic tectonites: integrating compositional mapping, microstructural analysis and *in situ* monazite dating. *Journal of Metamorphic Geology*, 30, pp. 739-752.

Williams, M. L., Jercinovic, M. J. & Hetherington, C. J., 2007. Microprobe Monazite Geochronology: Understanding Geologic Processes by Integrating Composition and Chronology. *Annual Review of Earth and Planetary Sciences*, 35, pp. 137-175.

Wooden, J. L. & Miller, D. M., 1990. Chronologic and isotopic framework for Early Proterozoic crustal evolution in the eastern Mojave Desert Region, SE California.

Journal of Geophysical Research: Solid Earth, 95, pp. 20133-20146.

Woodhead, J. D. & Herdt, J. M., 2005. A Preliminary Appraisal of Seven Natural Zircon Reference Materials for *In situ* Hf Isotope Determination. Geostandards and Geoanalytical Research, 29, pp. 183-195.

Woodhead, J.D., Herdt, J. M., Shelley, M., Eggins, S., & Kemp, R., 2004. Zircon Hf-isotope analysis with an excimer laser, depth profiling, ablation of complex geometries, and concomitant age estimation. Chemical Geology, 209, pp. 121-135.

Xie, L. et al., 2008. *In situ* simultaneous determination of trace elements, U-Pb and Lu-Hf isotopes in zircon and baddeleyite. Chinese Science Bulletin, Volume 53, pp. 1565-1573.

Xiong, Q., Zheng, J., Griffin, W.L., O'Reilly, S.Y., & Pearson, N.J., 2013. Decoupling of U-Pb and Lu-Hf isotopes and trace elements in zircon from the UHP North Qaidam orogen, NE Tibet (China): tracing the deep subduction of continental blocks. Lithos, 155, pp. 125-145.

Yuan, H.L., Gao, S., Dai, M.-N., Zong, C.-L., Günther, Fontaine, G.H., Liu, X.-M., & Diwu, C., 2008. Simultaneous determinations of U-Pb age, Hf isotopes and trace element compositions of zircon by excimer laser-ablation quadrupole and multiple-collector ICP-MS. Chemical Geology, 247, pp. 100-118.

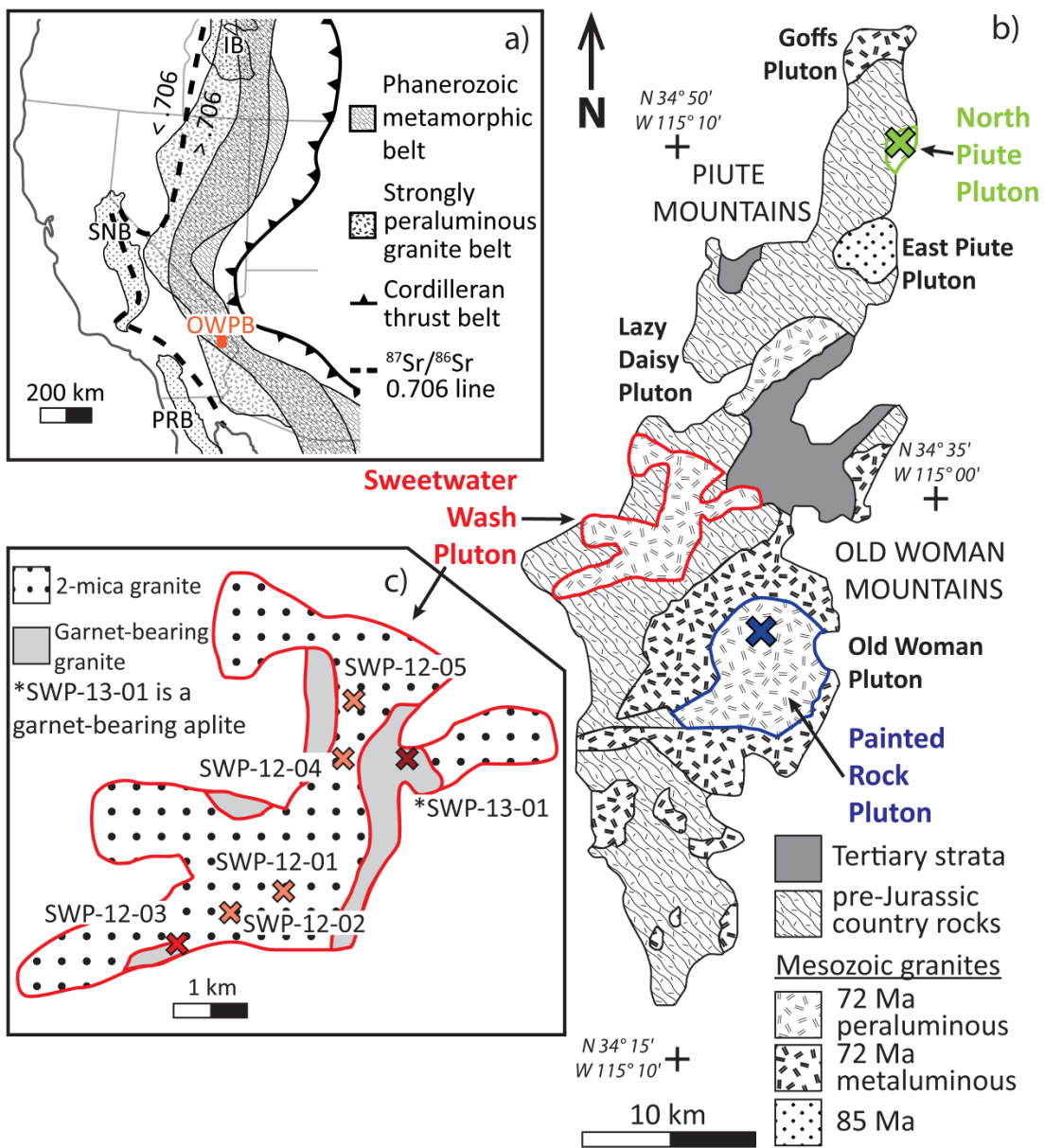


Figure 2.1: a) Location of the Old Woman-Piute Batholith in relation to tectonic and geochemical features of the North American Cordillera. After (Miller & Bradfish, 1980). b) Geological map of the Old Woman-Piute Range Batholith. After (Miller & Wooden, 1994). c) Geological map of the Sweetwater Wash Pluton. After (Mittlefehldt & Miller, 1983).

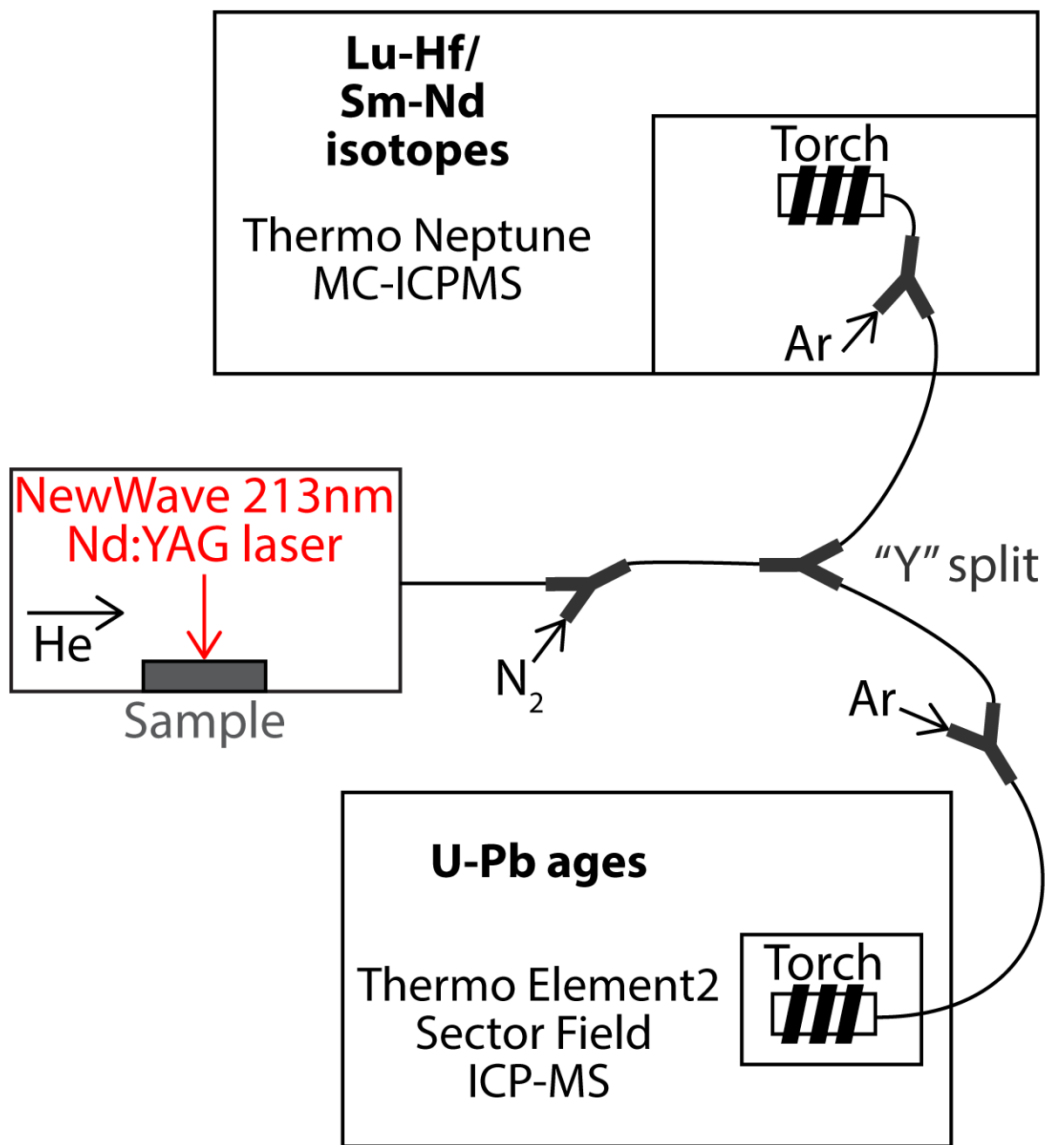


Figure 2.2: Schematic diagram of the Laser Ablation Split Stream (LASS) analytical setup. After (Fisher, et al., 2014)

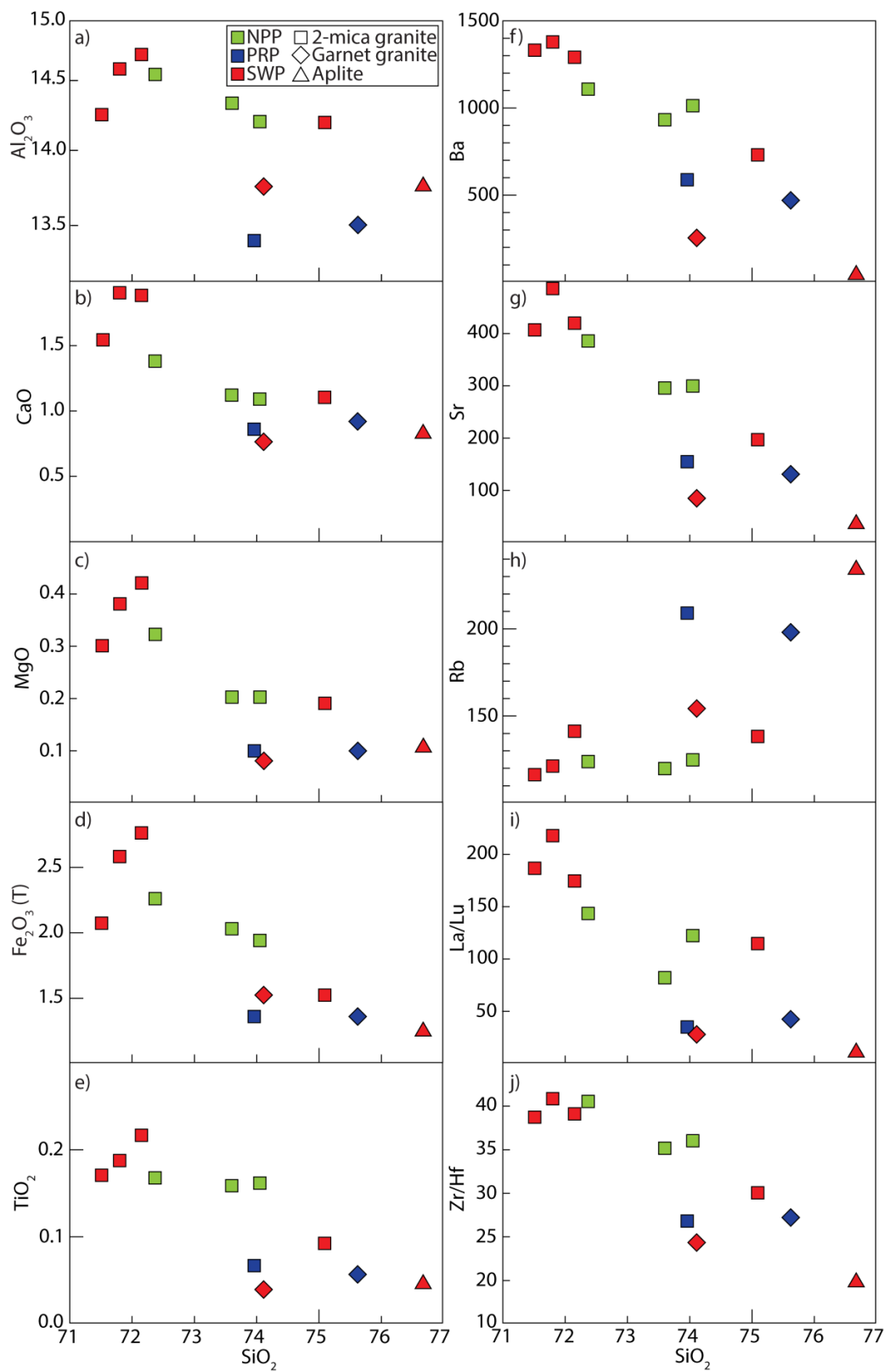


Figure 2.3: Whole rock Harker plots of major and trace elements of the OWPB samples.

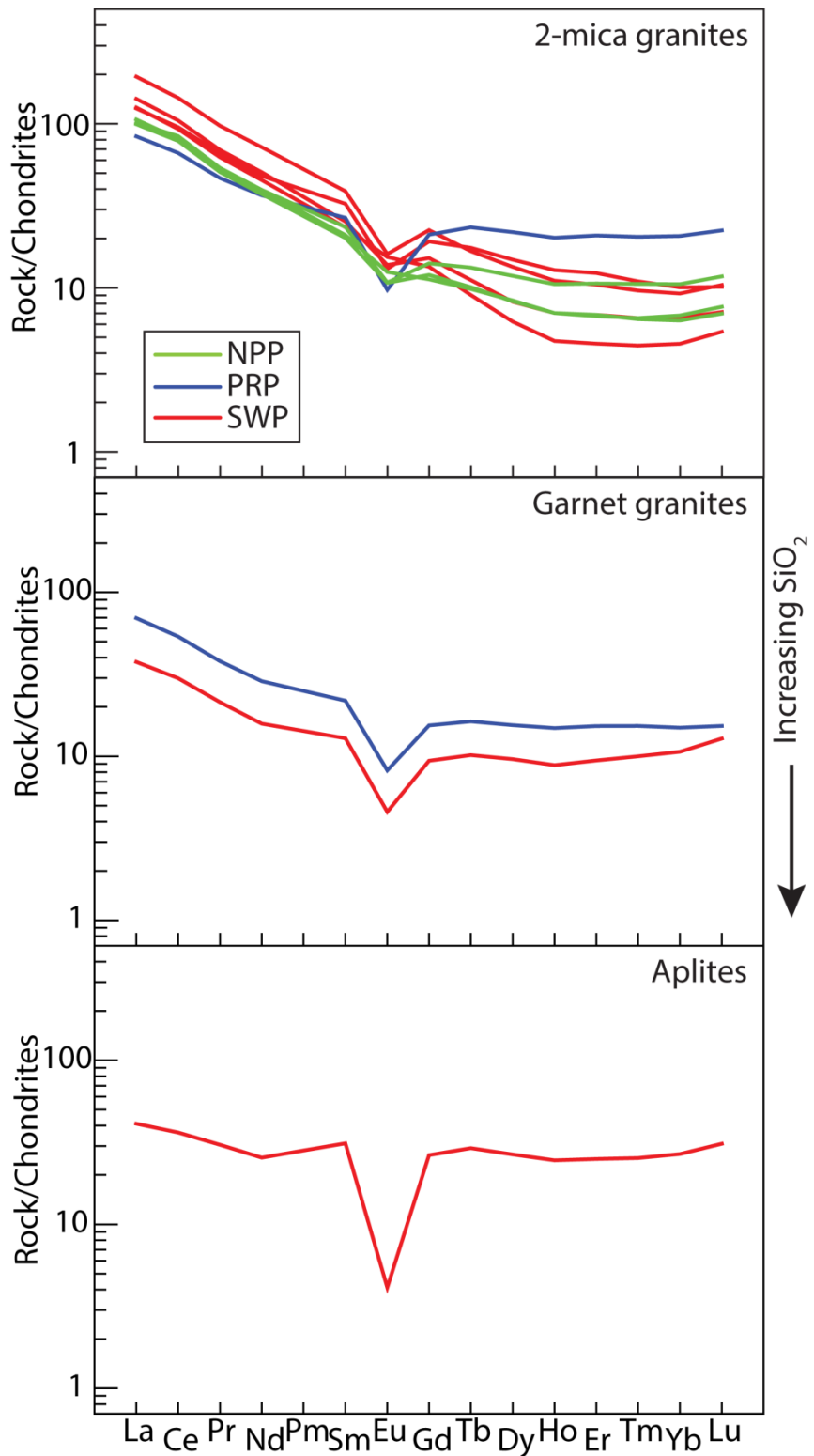


Figure 2.4: Chondrite normalised whole rock rare earth element plots for the OWPB samples. Using normalising values of Sun & McDonough (1989).

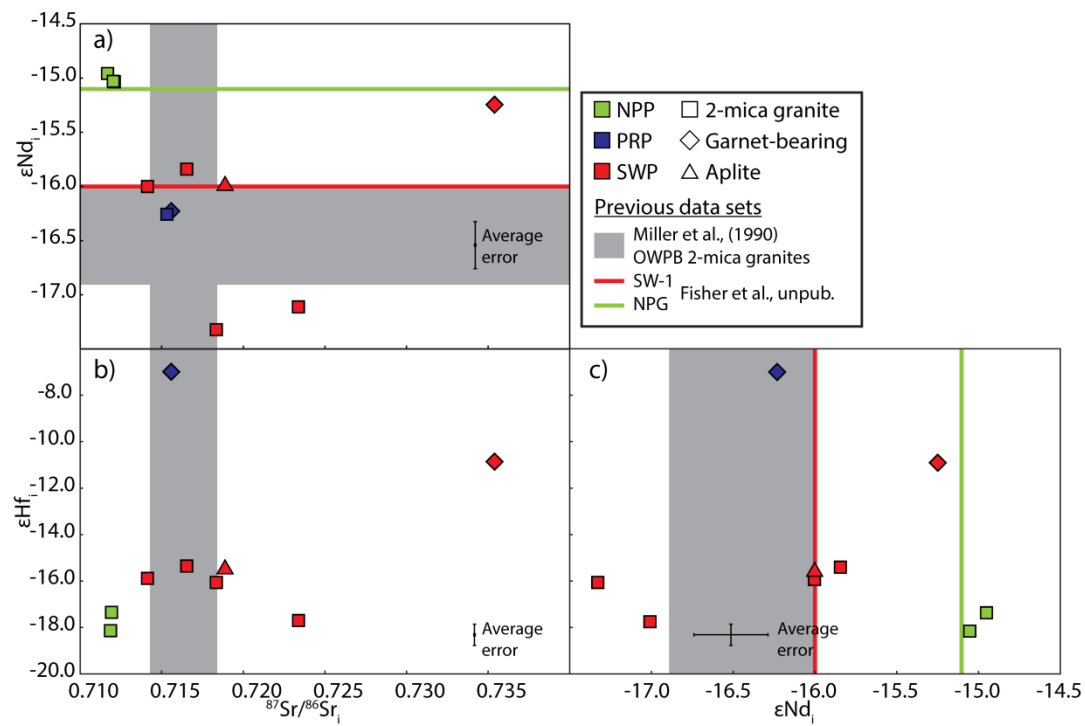


Figure 2.5: Whole rock tracer isotope data for OWPB samples. a) ϵ_{Nd_i} vs. $^{87}\text{Sr}/^{86}\text{Sr}_i$. b) ϵ_{Hf_i} vs. $^{87}\text{Sr}/^{86}\text{Sr}_i$. c) ϵ_{Nd_i} vs. ϵ_{Hf_i} .

Grey fields represent data from 2-mica granite samples from the OWPB of Miller et al. (1990). SW-1 and NPG data is from Fisher et al., (unpublished), with samples being from the SWP and NPP respectively.

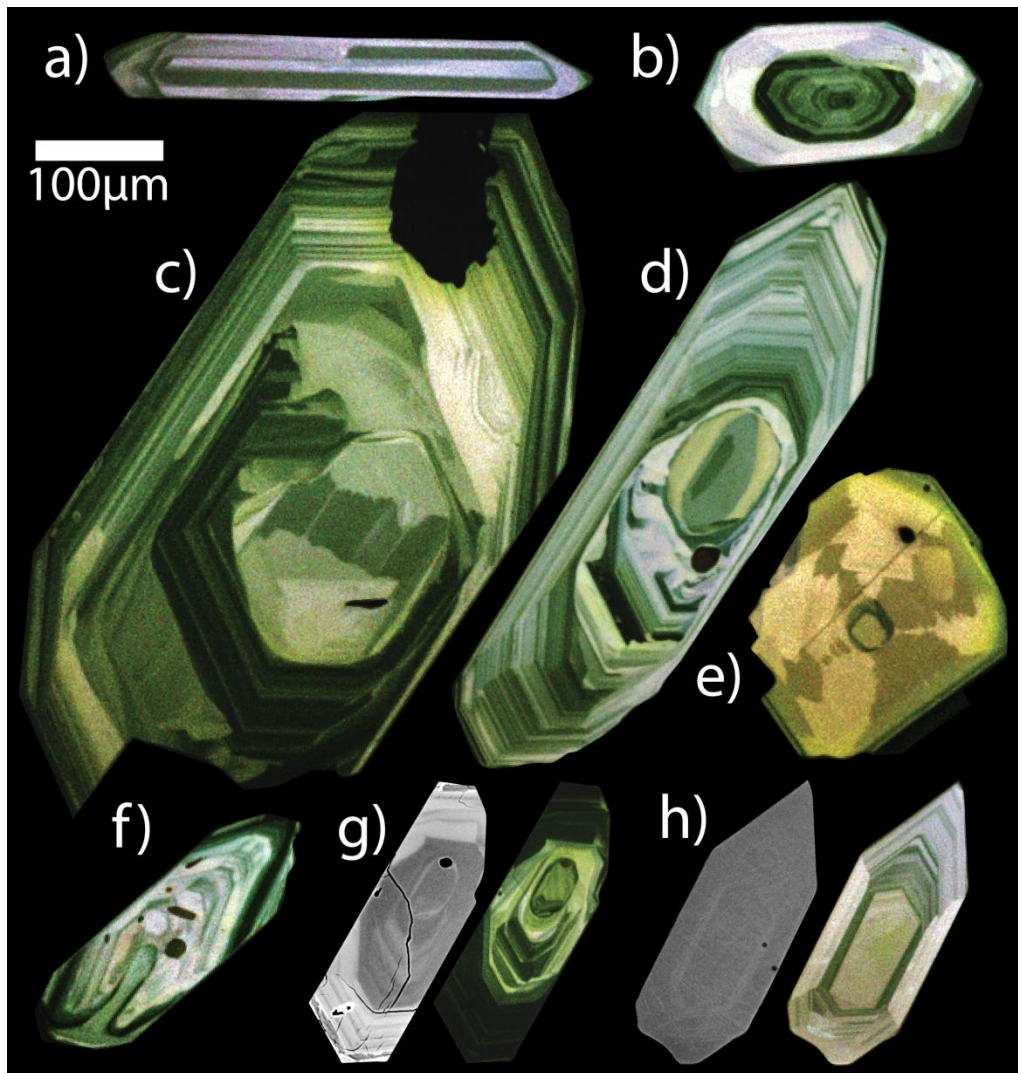


Figure 2.6: CL & BSE images of zircon crystals from the OWPB exhibiting a range of internal features. a) Acicular zircon with oscillatory zoning. b) Small tabular crystal with a rounded core. c) – d) Large crystals with multiple rim regions. e) Equant crystal with sector zoning. f) Deep embayment into the core region. g) – h) Right – BSE image, Left-CL image. g) Dark regions in CL are light regions in BSE. h) Zonation seen in CL is not seen in BSE image.

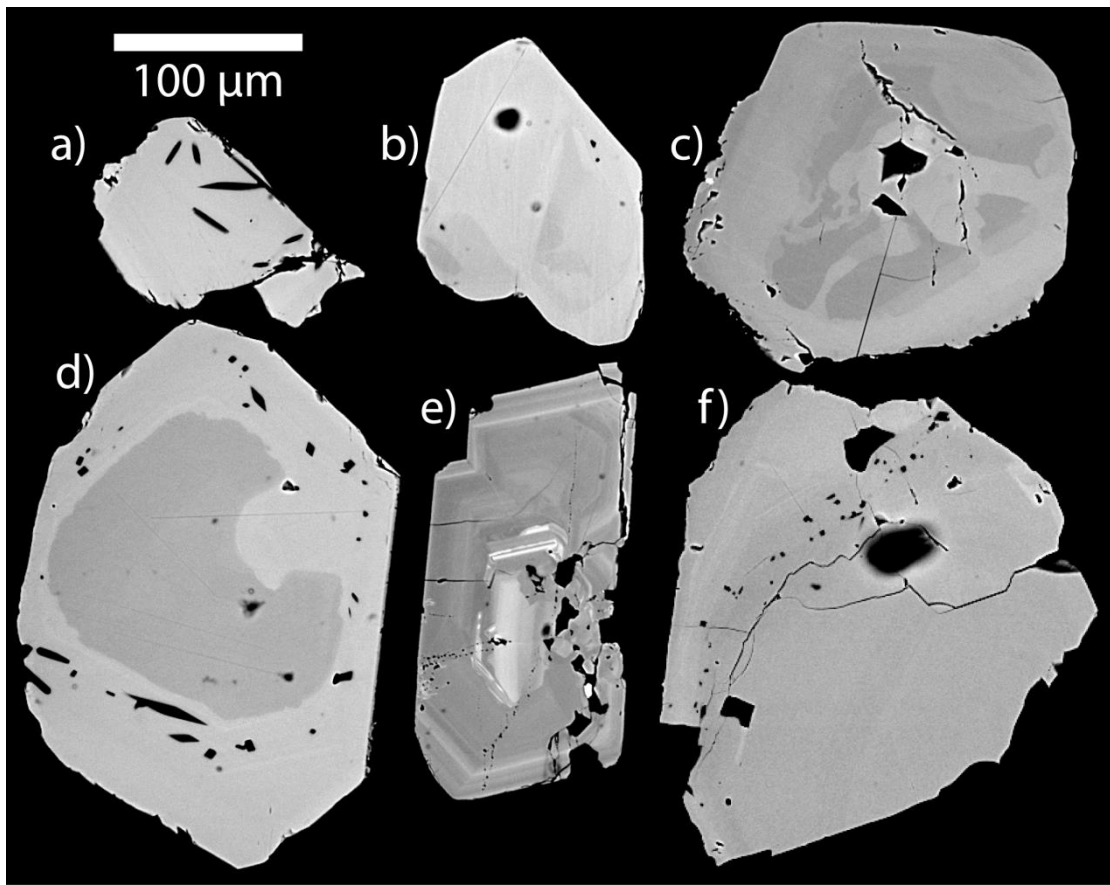


Figure 2.7: BSE images of monazite crystals from the OWPB exhibiting a range of internal features. a) Weak zoning and acicular zircon inclusions. b) Irregular patchy zoning. c) Veined zoning emanating from a central core. d) Simple zoning of core and rim with an embayment in the core. e) Concentric oscillatory zoning with zones parallel to the margin of the crystal. f) Inclusion trail extending throughout the crystal.

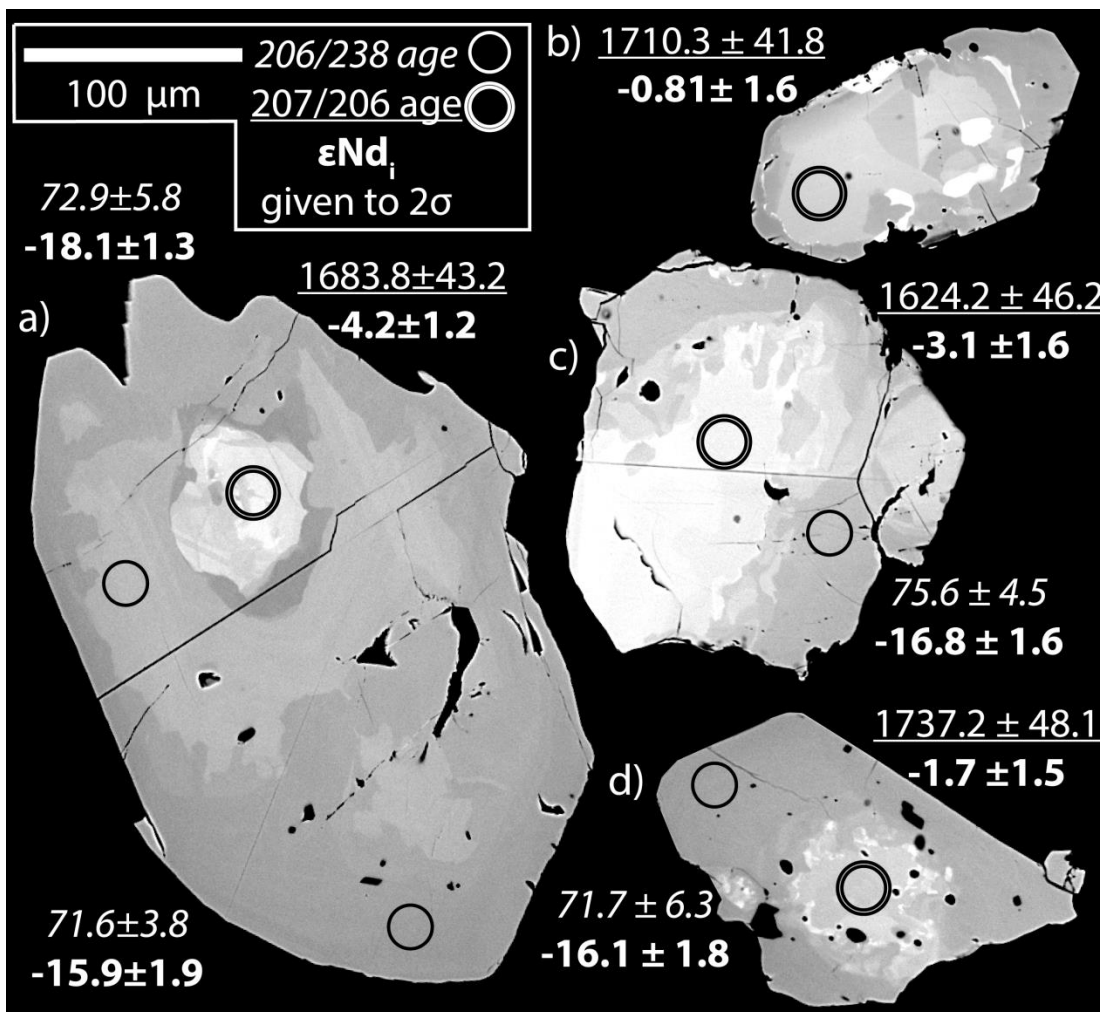


Figure 2.8: Th-rich monazite crystals. a) and d) show distinct, bright core regions, whereas b) shows irregular patches and c) shows large bright area that extends across most of the grain.

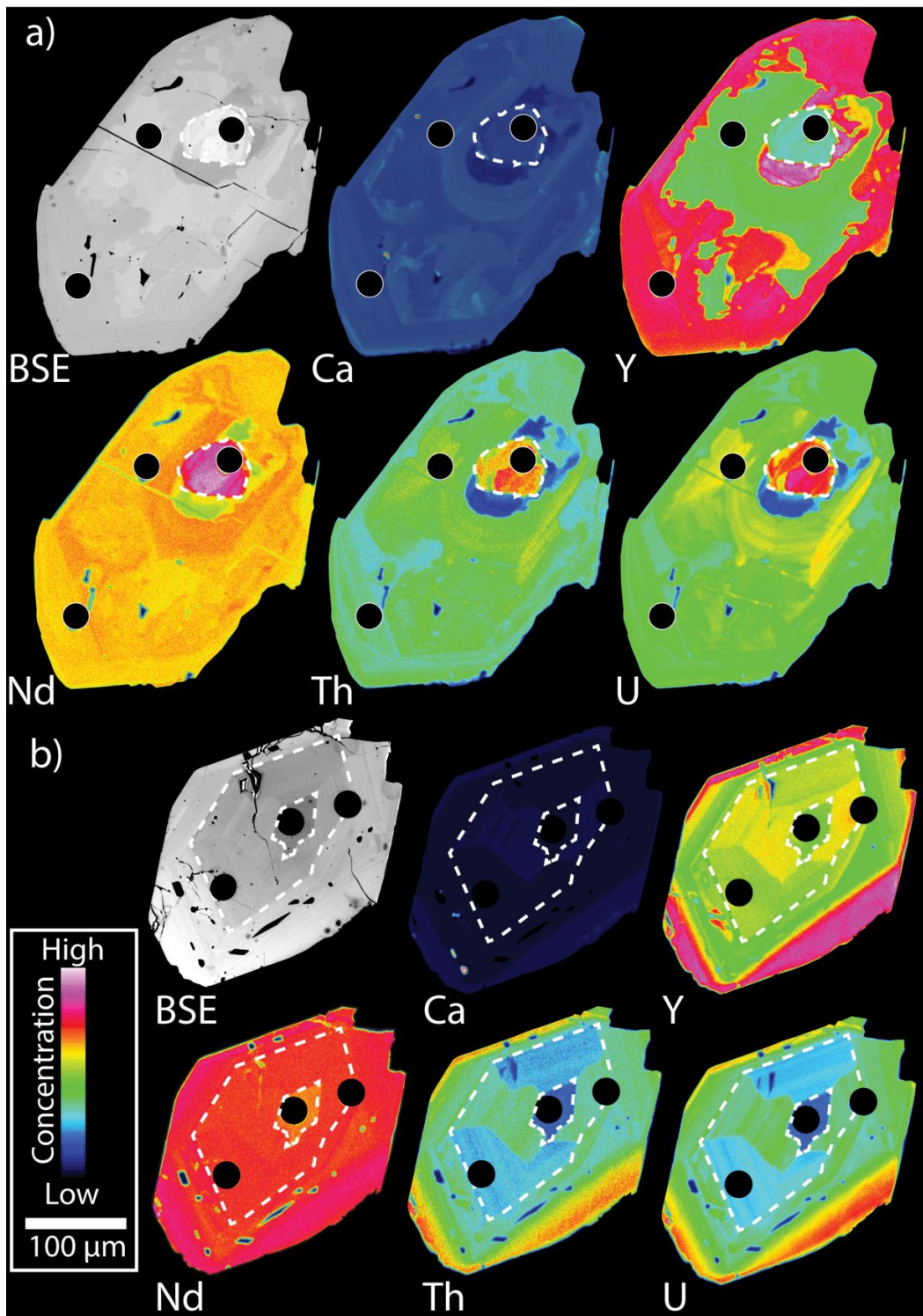


Figure 2.9: X-ray maps of selected monazite grains. BSE images are shown alongside element maps of Ca, Y, Nd, Th and U. a) is from sample SWP-12-05 and is the same grain shown in Figure 2.8a. b) is from sample NPP-13-01.

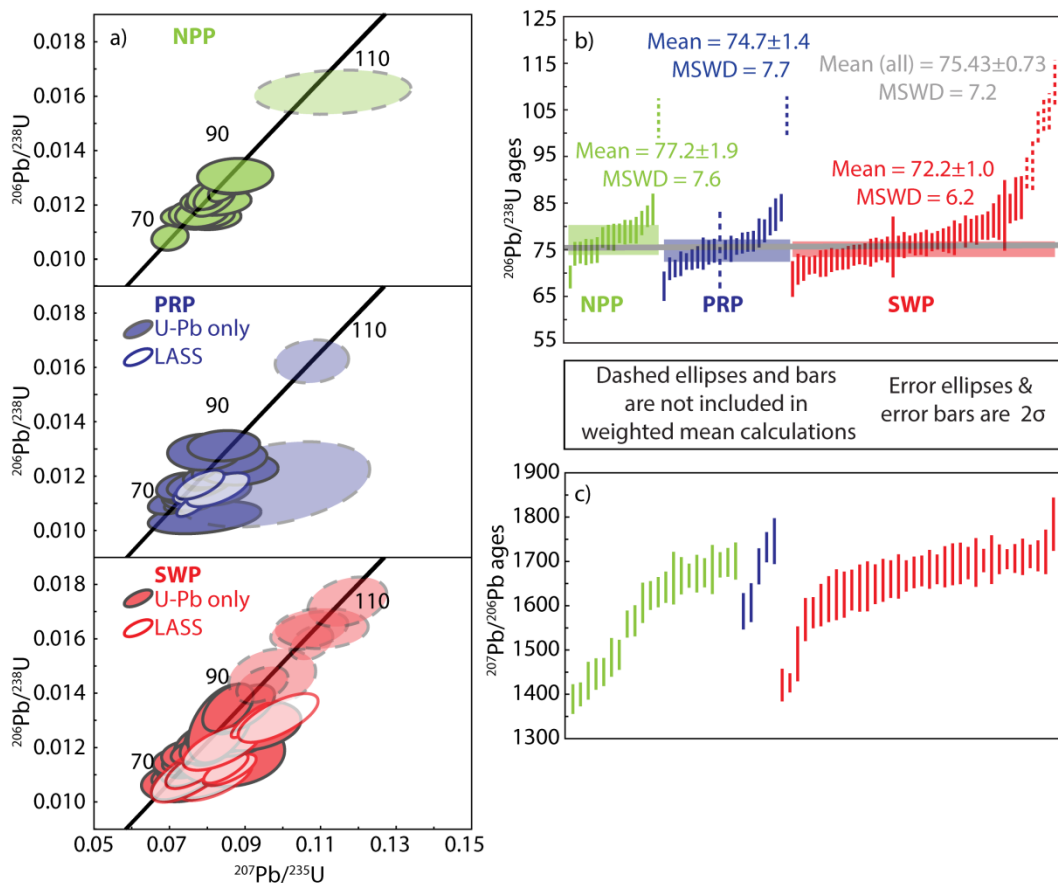


Figure 2.10: In situ zircon U-Pb isotopic data. a) Concordia diagrams for each of the plutons in the OWPB. Same scale used for each plot. b) Weighted mean plot of “young” zircon grains, showing average ages for each pluton and for the entire OWPB. MSWD = mean square weighted deviation. C) Weighted mean plot of “old” zircon grains.

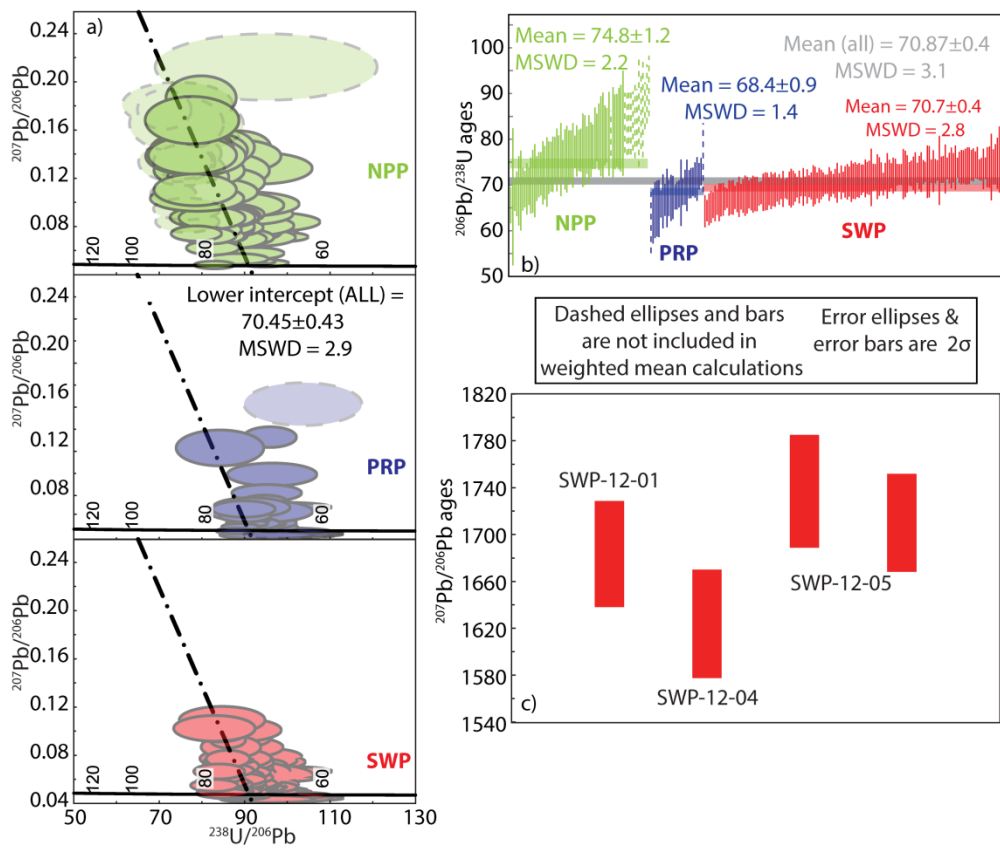


Figure 2.11: In situ monazite U-Pb isotopic data. a) Terra-Wasserburg diagrams for each of the plutons in the OWPB. Same scale used for each plot. Lower intercept calculated for all OWPB samples. b) Weighted mean plot of “young” monazite grains, showing average ages for each pluton and for the entire OWPB. MSWD = mean square weighted deviation. c) Weighted mean plot of “old” monazite grains.

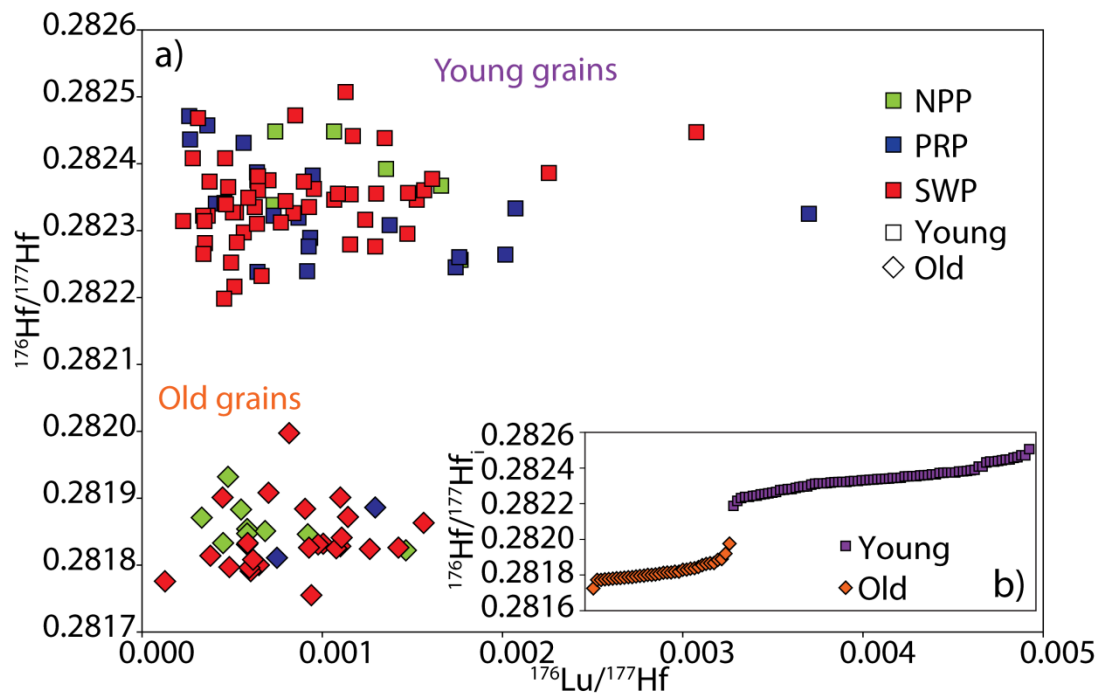


Figure 2.12: In situ zircon Lu-Hf isotopic data. a) $^{147}\text{Sm}-^{144}\text{Nd} - \frac{^{143}\text{Nd}}{^{144}\text{Nd}}$ plot for all OWPB samples. b) $\frac{^{143}\text{Nd}}{^{144}\text{Nd}}$ calculated for all OWPB samples.

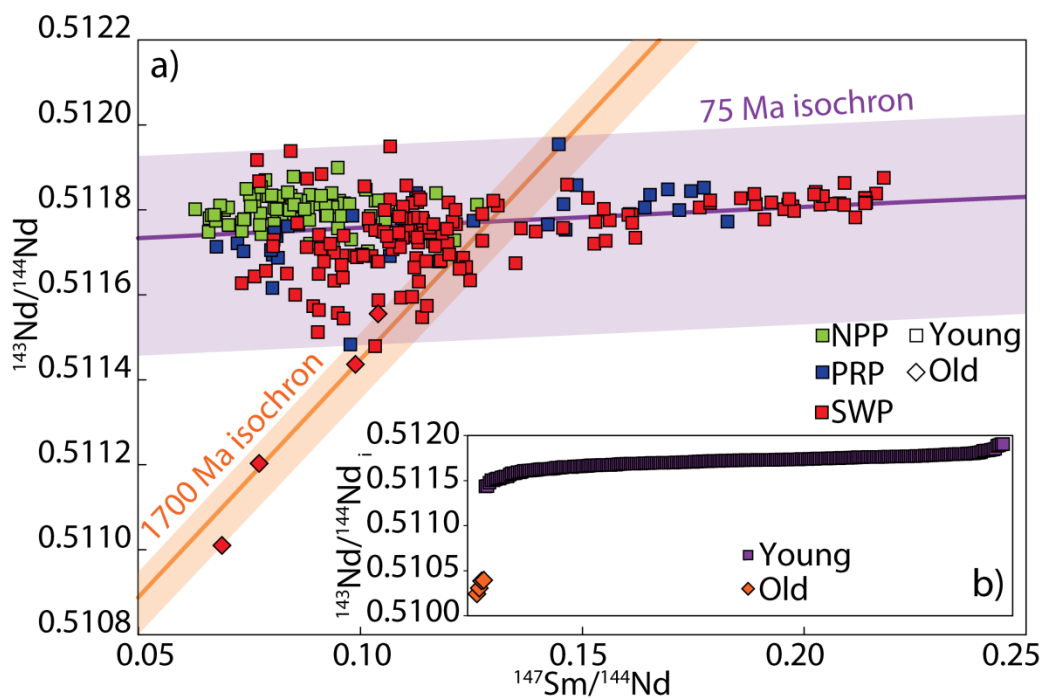


Figure 2.13: In situ monazite Sm-Nd isotopic data. a) $^{176}\text{Lu}-^{177}\text{Hf} - \frac{^{176}\text{Hf}}{^{177}\text{Hf}}$ plot for all OWPB samples. b) $^{176}\text{Hf}/^{177}\text{Hf}_i$ calculated for all OWPB samples.

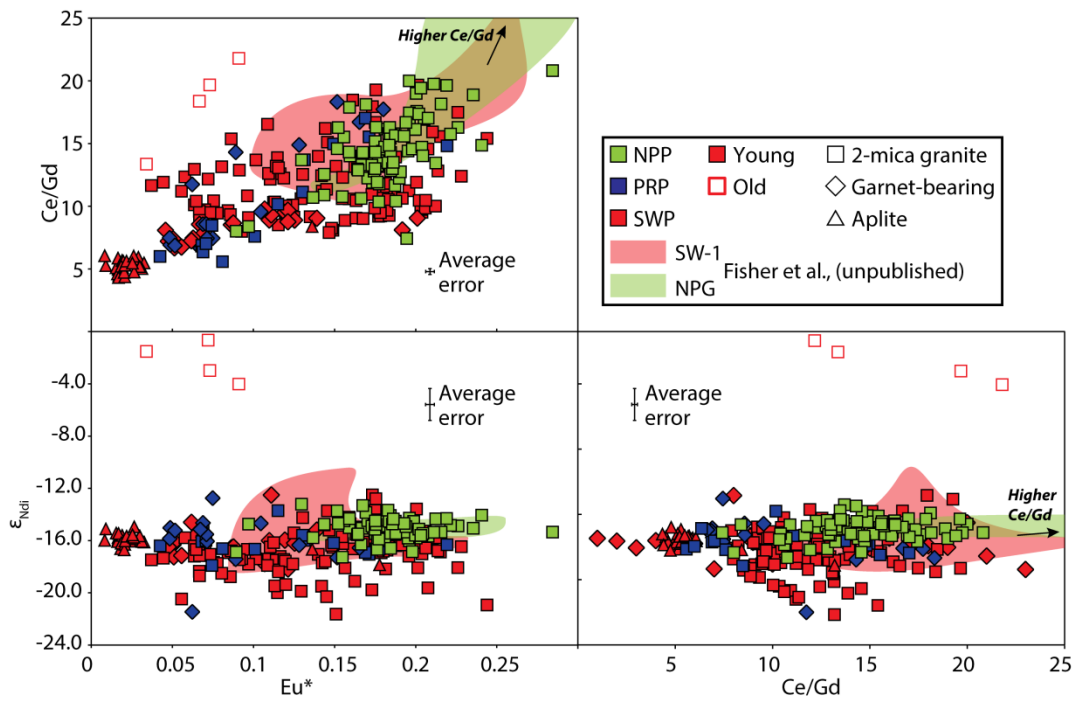


Figure 2.14: In situ monazite REE data. a) Ce/Gd vs. Eu*. b) ϵ_{Nd_i} vs. Eu*. c) ϵ_{Nd_i} vs. Ce/Gd.

SW-1 and NPG data is from Fisher et al., (unpublished), with samples being from the SWP and NPP respectively.

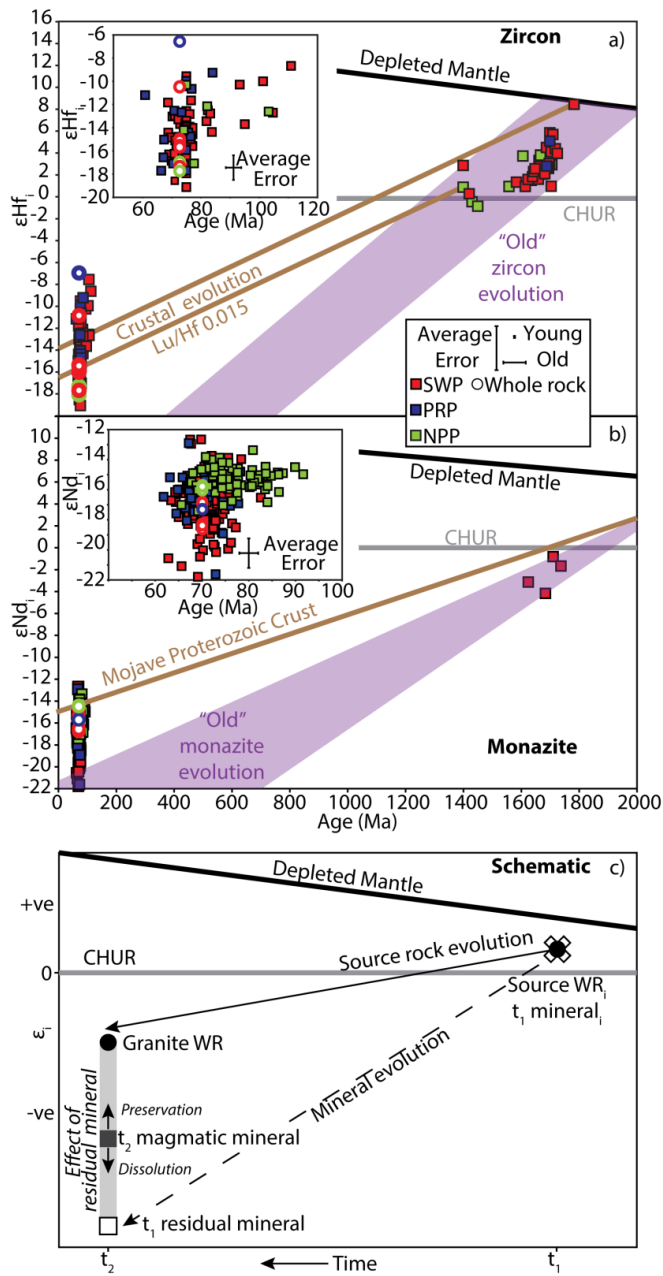


Figure 2.15: Epsilon – time plots for OWPB in situ isotopic data. a) Epsilon – time plot for in situ zircon data. Crustal evolution lines were calculated using initial ratios from zircon grains at 1800 Ma and 1400 Ma, and a typical crustal $^{176}\text{Lu}/^{177}\text{Hf}$ value of 0.015 b) Epsilon - time plot for in situ monazite data. Mojave Proterozoic Crust evolution line from Bennett & De Paolo (1987). c) Schematic diagram showing isotopic systematics of whole rock and mineral in situ samples and how their evolution varied depending on inheritance characteristics.

Chapter 3 - Summary

3.1 - Usefulness of the LASS technique

The analysis of multiple monazite and zircon reference materials attests to the accuracy of the LASS method (Goudie et al., 2014 and Appendix B). The high-spatial precision afforded by the laser-ablation technique suggests that it is the appropriate tool to use when there are intracrystal age variations that are larger than the analytical precision. In this study, therefore, LASS is an appropriate technique for distinguishing Proterozoic versus Cretaceous growth domains of minerals and to constrain the radiogenic tracer isotopic composition of the source region in which those minerals crystallized.

Within the Cretaceous growth domains, however, it appears that the intracrystal age variation is unresolvable at a precision of ~1-2%. This is not criticism specifically of the LASS technique, but is part of the larger discussions currently being held in the earth science community about the advantages of high-precision versus high-resolution work (Schoene et al., 2013). This study was not aimed at gaining a crystallisation age(s) for the OWPB, nor was it specifically addressing the matter of incremental pluton assembly. The *in situ* Hf and Nd isotopes were of most interest, and as demonstrated in Figure 2.11, the correct attribution of an age to an isotopic analysis is critical to making interpretations about initial isotopic compositions.

As well as providing a high spatial resolution dataset of accessory minerals, the LASS method is simply a more efficient way to collect data; two isotopic systems from one ablation spot. This also improves the chances of being able to collect further data from analysed grains, such as oxygen isotopes. Further analysis however brings back the original sampling issues involved with zoned minerals.

3.2 - Directions for future research

While this study shows how the LASS technique is successful in allowing correct calculation and interpretation of initial tracer isotope ratios, further precision is required to fully understand the timing of geological events in the OWPB during the Cretaceous. A study using high-precision ID-TIMS U-Pb dating or ID-TIMS-TEA would be useful in determining 1) whether the pluton was emplaced incrementally, and 2) how this melt geochemically evolved over time, in terms of tracer isotopes and trace elements. This approach has proven to be particularly effective when applied to the Adamello batholith, Italy (Schoene et al., 2012).

Bulk rock saturation temperatures are unable to fully resolve the thermal regimes of melt systems that are evolving in composition and potentially in temperature over time, and over a time period that may be associated with multiple injections of melt. Ti-in-zircon thermometry has proven useful in tracking such thermal perturbations (Claiborne et al., 2006, 2010a, 2010b; Ickert et al., 2010). These potential variations in the thermal regime within a magma body, along with compositional heterogeneities

within that body will have a large effect on the solubility of monazite (Montel, 1993). A more detailed model of saturation systematic could therefore provide useful constraints on the model presented in this paper regarding the effect of solubility of accessory minerals on the transfer of isotopic heterogeneity.

Furthermore, the Hf isotopic composition of the Mojave Proterozoic crust should be determined as it has been for Nd, as this would further constrain the composition of the source region. An investigation into the Lu-Hf composition of the garnet crystals in the garnet-bearing rocks of the OWPB would also allow further insight into the complete Hf budget of the magmatic system.

3.3 - Conclusions

The Old Woman-Piute Batholith, Mojave Desert, California is partly composed of three plutons, the Painted Rock Pluton, Sweetwater Wash Pluton and North Piute pluton. These plutons exhibit predictable bulk rock geochemical trends that can be explained by the fractionation of the mineral assemblage observed, with feldspar, garnet, zircon and monazite being the minerals responsible. Whole rock saturation temperatures calculated from Zr and REE contents indicate emplacement temperatures of ~700-750 °C.

Zircon inheritance is widespread in the OWPB samples while only four monazite grains show inherited cores. U-Pb ages from both zircon and monazite yield ages between ~1400 - 1800 Ma, which is consistent with the regional geochronology of the

Proterozoic crust in the Mojave region. Emplacement of the plutons was during the Cretaceous, with zircon and monazite domains give a range of ages between ~70-75 Ma. Given the precision of the LA-ICP-MS it is not possible to resolve distinct crystallisation ages at the batholith-, pluton- or rock unit- scale. The range of ages preserved may be due to incremental emplacement of melt batches; however a higher precision technique such as ID-TIMS would be required to investigate this hypothesis further.

The Proterozoic crust into which the OWPB is emplaced is suggested to be the source of these melts at depth. The preservation or dissolution of residual zircon and monazite crystals at the source during melting had a large effect on the composition of the resulting melt and the minerals that form from it. Dissolution of accessory minerals allows the transfer of isotopic compositions to the resulting melt. Variable amounts of dissolution of zircon and monazite therefore lead to a wide range of ϵ_{Hf} and ϵ_{Nd} respectively. While this transfer process is effective, the preservation of this heterogeneity indicates that the mixing and homogenisation of melt batches was limited. Furthermore, the source region is observed to be heterogeneous to begin with, as inherited zircon cores preserve a large range of Hf isotopic compositions. There is no evidence in the OWPB of interaction of crustal and mantle melts, therefore this study offers an alternative explanation for the cause of heterogeneity in granitic plutons.

Observed textures in zircon and monazite suggest the magmatic growth of Cretaceous zircon and monazite grains. Where inherited cores are present they are often resorbed and show evidence of dissolution, with core-rim boundaries being

texturally and compositionally sharp. As these textures are indicative of the saturation level of the melt, it is suggested that the melt was approaching zircon saturation when it formed, but dissolution of zircon was required in order for the melt to attain equilibrium. The melt was strongly undersaturated with regards to monazite, meaning that most monazite that was present at the source dissolved and little residual monazite was available to be entrained in the melt. The lack of coherence between Hf and Nd as predicted by the terrestrial array also suggests that unreacted zircon remained at the source. When saturation levels were attained dissolution ceased and new zircon and monazite grew to form rims on inherited grains, or as new crystals without cores.

Of the three plutons studied the NPP is the most homogenous, both in the field and in its geochemistry (at the whole rock- and mineral- scale), the smallest, and is suggested to be the oldest. It is therefore proposed that this pluton formed first from small volumes of homogeneous melt. The PRP and SWP formed subsequently from larger volumes of melt that were potentially emplaced incrementally. These larger bodies were not able to undergo homogenisation and preserved their heterogeneous compositions. They were also able to develop geochemically resulting in a wider range in whole rock elemental compositions and rock types.

References

- Amelin, Y., Lee, D-C., Halliday, A.N., 2000. Early-middle Archaean crustal evolution deduced from Lu-Hf and U-Pb isotopic studies of single zircon grains. *Geochimica et Cosmochimica Acta*, 64, pp. 4205-4225.
- Anderson, J. L., 1983. Proterozoic anorogenic granite plutonism of North America. *Geological Society of America Memoir*, 161, pp. 133-154.
- Barth, A. P., Wooden, J. L., Coleman, D. S. & Marilyn B. Vogel, 2009. Assembling and Disassembling California: A Zircon and Monazite Geochronologic Framework for Proterozoic Crustal Evolution in Southern California. *The Journal of Geology*, 117(3), pp. 221-239.
- Begemann, F., Ludwig, K.R., Lugmair, G.W., Min, K., Nyquist, L.E., Patchett, P.J., Renne, P.R. Shih, C.-Y., Villa, I.M., & Walker, R.J., 2001. Call for an improved set of decay constants for geochronological use. *Geochimica et Cosmochimica Acta*, 65, pp. 111-121.
- Bender, E. E., 2008. Petrogenesis of the Fenner Gneiss, Piute and Old Woman Mountains, San Bernardino County, California, *Geological Society of America Abstracts with Programs*, 40, pp. 250.

Bennett, V. C. & DePaolo, D. J., 1987. Proterozoic crustal history of the western United States as determined by neodymium isotopic mapping. Geological Society of America Bulletin, 99, pp. 674-685.

Blichert-Toft, J., 2008. The Hf isotopic composition of zircon reference material 91500. Chemical Geology, 253, pp. 252-257.

Boehnke, P., Watson, E.B., Trail, D., Harrison, T.M., & Schmitt, A.K. (2013) Zircon saturation re-revisited. Chemical Geology, 351, pp. 324–334.

Bouvier, A., Vervoort, J. D. & Patchett, P. J., 2008. The Lu-Hf and Sm-Nd isotopic composition of CHUR: Constraints from unequilibrated chondrites and implications for the bulk composition of terrestrial planets. Earth and Planetary Science Letters, 273, pp. 48-57.

Burchfiel, B. C. & Davis, G. A., 1981. The Geotectonic development of California. In: W. G. Ernst & W. W. Rubey, eds., Prentice-Hall, pp. 217-252.

Carl, B. S. & Miller, C. F., 1991. Western Old Woman Mountains shear zone: Evidence for late ductile extension in the Cordilleran orogenic belt. Geology, 19, pp. 893-896.

Catlos, E. J., 2013. Versatile Monazite: resolving geological records and solving challenges in materials science: Generalizations about monazite: Implications for geochronologic studies. American Mineralogist, 98, pp. 819-832.

Chang, Z., Vervoort, J. D., McClelland, W. C. & Knaack, C., 2006. U-Pb dating of zircon by LA-ICP-MS. *Geochemistry, Geophysics, Geosystems*, 7, pp. Q05009.

Cherniak, D., 2010. Diffusion in Accessory Minerals: Zircon, Titanite, Apatite, Monazite and Xenotime. In Y. Zhang and D.J. Cherniak, Eds., *Diffusion in Minerals and Melts*, *Reviews in Mineralogy and Geochemistry*, 72, pp. 827-869.

Cherniak, D. J. & Watson, E. B., 2003. Diffusion in Zircon. *Reviews in Mineralogy and Geochemistry*, 53, pp. 113-143.

Claiborne, L. L., Miller, C.F., Walker, B.A., Wooden, J.L., Mazdab, F.K., & Bea, F., 2006. Tracking magmatic processes through Zr/Hf ratios in rocks and Hf and Ti zoning in zircons: An example from the Spirit Mountain batholith, Nevada. *Mineralogical Magazine*, 70, pp. 517-543.

Claiborne, L.L., Miller, C.F., Flanagan, D.M., Clyne, M.A., Wooden , J.L., 2010a. Zircon reveals protracted magma storage and recycling beneath Mount St. Helens. *Geology*, 38, pp. 1011–1014.

Claiborne, L.L., Miller, C.F., Wooden, J.L., 2010b. Trace element composition of igneous zircon: a thermal and compositional record of the accumulation and evolution of a large silicic batholith, Spirit Mountain, Nevada. *Contributions to Mineralogy and Petrology*, 160, pp. 511–531.

Corfu, F., Hanchar, J.M., Hoskin, P.W.O. and Kinny, P. (2003) Atlas of zircon textures. In: J.M. Hanchar and P.W.O. Hoskin, Eds. *Zircon. Reviews in Mineralogy & Geochemistry*, 53, pp 469-500.

Coleman, D. S., Gray, W. & Glazner, A. F., 2004. Rethinking the Emplacement and Evolution of Zoned Plutons: Geochronologic Evidence for Incremental Assembly of the Tuolumne Intrusive Suite, California. *Geology*, 32, pp. 433–6.

Colombini, L.L., Miller, C.F., Gualda, G.A.R., Wooden, J.L., & Miller, J.S., 2011. Sphene and zircon in the Highland Range volcanic sequence (Miocene, southern Nevada, USA): elemental partitioning, phase relations, and influence on evolution of silicic magma. *Mineralogy and Petrology*, 102, pp. 29-50.

Copeland, P., Parrish, R.R., & Harrison, T.M., 1988. Identification of inherited radiogenic Pb in monazite and its implications for U-Pb systematics. *Nature*, 333 (23), pp.760-763.

Cressey, G., Wall, F. & Cressey, B. A., 1999. Differential REE uptake by sector growth of monazite. *Mineralogical Magazine*, 63, pp. 813-828.

Crowley, J. L., Brown, R. L., Gervais, F. & Gibson, H. D., 2008. Assessing Inheritance of Zircon and Monazite in Granitic Rocks from the Monashee Complex, Canadian Cordillera. *Journal of Petrology*, 49, pp. 1915-1929.

Dunning, G., Macdonald, A. & Barr, S., 1995. Zircon and monazite U-Pb dating of the Doi Inthanon core complex, northern Thailand: implications for extension within the Indosinian Orogen. *Tectonophysics*, 251, pp. 197-213.

Faure, G. & Mensing, T., 2005. *Isotopes: principles and applications*. 3rd ed., John Wiley & Sons, 897 pp..

Farina, F., Stevens, G., Gerdes, A., & Frei, D., 2014. Small-scale Hf isotopic variability in the Peninsula pluton (South Africa): the processes that control inheritance of source $^{176}\text{Hf}/^{177}\text{Hf}$ diversity in S-type granites. *Contributions to Mineralogy and Petrology*, 168, pp. 1065.

Fisher, C. M., Hanchar, J.M., Samson, S.D., Dhuime, B., Blichert-Toft, J., Vervoort, J.D., & Lam, R., 2011. Synthetic zircon doped with hafnium and rare earth elements: A reference material for *in situ* hafnium isotope analysis. *Chemical Geology*, 286, pp. 32-47.

Fisher, C. M., McFarlane, C.R.M., Hanchar, J.M., Schmitz, M.D., Sylvester, P.J., Lam, R., & Longerich, H.P., 2011. Sm-Nd isotope systematics by laser ablation-multicollector-inductively coupled plasma mass spectrometry: Methods and potential natural and synthetic reference materials. *Chemical Geology*, Volume 284, pp. 1-20.

Fisher, C.M., Vervoort, J.D. and Hanchar, J.M., 2012. Split-stream laser ablation microanalysis: U-Pb age and Lu-Hf isotopic composition of complexly zoned zircon

crystals from the ancient zircon record. Abstract V12A-03 presented at 2012 Fall Meeting, AGU, San Francisco, Calif., 3-7 Dec.

Fisher, C. M., Vervoort, J. D. & DuFrane, S. A., 2014. Accurate Hf isotope determinations of complex zircons using the "laser ablation split stream" method. *Geochemistry, Geophysics, Geosystems*, 15, pp. 121-139.

Foster, D. A., Harrison, T. M. & Miller, C. F., 1989. Age, Inheritance, and Uplift History of the Old Woman-Piute Batholith, California and Implications for K-Feldspar Age Spectra. *The Journal of Geology*, 97, pp. 232-243.

Foster, D. A., Harrison, T. M., Miller, C. F. & Howard, K. A., 1990. The $^{40}\text{Ar}/^{39}\text{Ar}$ thermochronology of the eastern Mojave Desert, California, and adjacent western Arizona with implications for the evolution of metamorphic core complexes. *Journal of Geophysical Research: Solid Earth*, 95, pp. 20005-20024.

Foster, D. A., Miller, C. F., Harrison, T. M. & Hoisch, T. D., 1992. $^{40}\text{Ar}/^{39}\text{Ar}$ thermochronology and thermobarometry of metamorphism, plutonism, and tectonic denudation in the Old Woman Mountains area, California. *Geological Society of America Bulletin*, 104, pp. 176-191.

Goodge, J.W., & Vervoort, J.D., 2006. Origin of Mesoproterozoic A-type granites in Laurentia: Hf isotope evidence. *Earth and Planetary Science Letters*, 243, pp. 711-731.

Goudie, D. J., Fisher, C.M., Hanchar, J.M., Crowley, J.L., & Ayers, J.C., 2014. Simultaneous *in situ* determination of U-Pb and Sm-Nd isotopes in monazite by laser ablation ICP-MS. *Geochemistry, Geophysics, Geosystems*, 15, pp. 2575-2600.

Goudie, D. J., Fisher, C.M., Hanchar, J.M., Crowley, J.L., & Ayers, J.C., 2014. Simultaneous *in situ* determination of U-Pb and Sm-Nd isotopes in monazite by laser ablation ICP-MS. *Geochemistry, Geophysics, Geosystems*, 15(6), pp. 2575-2600.

Glazner, A. F., Bartley, J. M., Coleman, D. S., Gray, W. M. & Taylor, R. Z., 2004. Are plutons assembled over millions of years by amalgamation from small magma chambers? *Geological Society of America Today*, 14 , pp. 4–11.

Hanchar, J.M. & Miller, C.F., 1993. Zircon zonation patterns as revealed by cathodoluminescence and backscattered electron images: Implications for interpretation of complex crustal histories. *Chemical Geology*, Volume 110, pp. 1-13.

Hanchar, J. M., Miller, C.F., Wooden, J.L., Bennett, V.C., & Staude, J.-M.G., 1994. Evidence from Xenoliths for a Dynamic Lower Crust, Eastern Mojave Desert, California. *Journal of Petrology*, 35, pp. 1377-1415.

Hanchar, J.M. & Rudnick, R., 1995. Revealing hidden structures: The application of cathodoluminescence and back-scattered electron imaging to dating zircons from lower crustal xenoliths. *Lithos* , 36, pp. 289-303.

Harrison, T. M., Blichert-Toft, J., Müller, W., Albarede, F., Holden, P., & Mojzsis, S.J.,

2005. Heterogeneous Hadean hafnium: Evidence of continental crust at 4.4 to 4.5 Ga. *Science*, 310, pp. 1947–1950.

Hawkesworth, C. J., & Kemp, A.I.S., 2006. Using hafnium and oxygen isotopes in zircons to unravel the record of crustal evolution. *Chemical Geology*, 226, pp. 144–162.

Hawkins, D. P. & Bowring, S. A., 1997. U-Pb systematics of monazite and xenotime: case studies from the Paleoproterozoic of the Grand Canyon, Arizona. 127, pp. 87-103.

Hawkins, D. P. & Bowring, S. A., 1997. U-Pb systematics of monazite and xenotime: case studies from the Paleoproterozoic of the Grand Canyon, Arizona. Contributions to Mineralogy and Petrology, Volume 127, pp. 87-103.

Hu, Z., Liu, Y., Gao, S., Liu, W., Zhang, W., Tong, X., Lin, L., Zong, K., Li, M., Chen, H., Zhou, L., & Yang, L., 2012. Improved *in situ* Hf isotope ratio analysis of zircon using newly designed X skimmer cone and jet sample cone in combination with the addition of nitrogen by laser ablation multiple collector ICP-MS. *Journal of Analytical Atomic Spectrometry*, 27, pp. 1391-1399.

Ickert, R.B., Williams, I.S., Wyborn, D., 2010. Ti-in-zircon from the Boggy Plain zoned pluton: implications for zircon petrology and Hadean tectonics. Contributions to Mineralogy and Petrology, 162, pp. 447–461.

Iizuka, T., Eggins, S.M., McCulloch, M.T., Kinsley, L.P.J., Mortimer, G.E., 2011. Precise and accurate determination of $^{147}\text{Sm}/^{144}\text{Nd}$ and $^{143}\text{Nd}/^{144}\text{Nd}$ in monazite using laser ablation-MC-ICPMS. *Chemical Geology*, 282, pp. 45-57.

Iizuka, T., Nebel, O. & McCulloch, M. T., 2011. Tracing the provenance and recrystallization processes of the Earth's oldest detritus at Mt. Narryer and Jack Hills, Western Australia: An *in situ* Sm-Nd isotopic study of monazite. *Earth and Planetary Science Letters*, 308, pp. 350-358.

Jackson, S. E., Pearson, N. J., Griffin, W. L. & Belousova, E. A., 2004. The application of laser ablation-inductively coupled plasma-mass spectrometry to *in situ* U-Pb zircon geochronology. *Chemical Geology*, 211, pp. 47-69.

Jeffries, T. E., Fernandez-Suarez, J., Corfu, F. & Gutierrez Alonso, G., 2003. Advances in U-Pb geochronology using a frequency quintupled Nd:YAG based laser ablation system ($\lambda = 213$ nm) and quadrupole based ICP-MS. *Journal of Analytical Atomic Spectrometry*, 18, pp. 847-855.

Kapp, J.D., Miller, C.F., & Miller, J.S., 2002. Ireteba Pluton, Eldorado Mountains, Nevada; late, deep-source, peraluminous magmatism in the Cordilleran interior. *Journal of Geology*, 110, pp. 649–669.

Karlstrom, K. E., Miller, C. F., Kingsbury, J. A. & Wooden, J. L., 1993. Pluton emplacement along an active ductile thrust zone, Piute Mountains, southeastern California:

Interaction between deformational and solidification processes. Geological Society of America Bulletin, 105, pp. 213-230.

Kelsey, D. E., Clark, C. & Hand, M., 2008. Thermobarometric modelling of zircon and monazite growth in melt-bearing systems: examples using model metapelitic and metapsammitic granulites. Journal of Metamorphic Geology, 26, pp. 199-212.

Kemp, A. I. S. et al., 2007. Magmatic and Crustal Differentiation History of Granitic Rocks from Hf-O Isotopes in Zircon. Science, 315, pp. 980-983.

Kingsbury, J. A., Miller, C. F., Wooden, J. L. & Harrison, T., 1993. Monazite paragenesis and U-Pb systematics in rocks of the eastern Mojave Desert, California, U.S.A.: implications for thermochronometry. Chemical Geology, Volume 110, pp. 147-167.

Kistler, R. W., 1990. Two different lithosphere types in the Sierra Nevada, California. In: L. Anderson, ed. The Nature and Origin of Cordilleran Magmatism, Geological Society of America, Memoirs, pp. 271-281.

Košler, J., Forst, L. & Sláma, J., 2008. Spreadsheet-based data reduction for laser ablation ICP-MS. In: P. J. Sylvester, ed. Laser ablation in the Earth Sciences: Current practices and outstanding. Short Course Series 40, Mineralogical Association of Canada, Quebec, pp. 315-317.

Košler, J. & Sylvester, P. J., 2003. Present Trends and the Future of Zircon in Geochronology: Laser Ablation ICPMS In: J.M. Hanchar and P.W.O. Hoskin, Eds. *Zircon*. Reviews in Mineralogy & Geochemistry, 53, pp. 243-275.

Livaccari, R. F., 1991. Role of crustal thickening and extensional collapse in the tectonic evolution of the Sevier-Laramide orogeny, western United States. *Geology*, 19, pp. 1104-1107.

Ludwig, K., 2003. User's Manual for Isoplot 3.00, Berkeley, California.

MacLachlan, K., N. Rayner, G. Dunning, and C. Leugner (2004), New results and ideas from the Rottenstone Domain project, in Summary of Investigations 2004 [CD-ROM], Misc. Rep. 2004-4.2, 2, p. 21, Industry Resources, Saskatchewan Geological Survey, Saskatchewan, Canada.

Mattinson, J.M., 2005. Zircon U-Pb chemical abrasion (bCA-TIMSQ) method: Combined annealing and multi-step partial dissolution analysis for improved precision and accuracy of zircon ages. *Chemical Geology*, 220, pp. 47-66.

Matzel, J. E., Bowring, S. A. & Miller, R. B., 2006. Time scales of pluton construction at differing crustal levels: Examples from the Mount Stuart and Tenpeak intrusions, North Cascades, Washington. *Geological Society of America Bulletin*, 118, pp. 1412-1430.

McFarlane, C. & McCulloch, M., 2007. Coupling of in-situ Sm-Nd systematics and U-Pb dating of monazite and allanite with applications to crustal evolution studies.

Chemical Geology, Volume 245, pp. 45-60.

Memeti, V., Paterson, S.R., Matzel, J., Mundil, R., & Okaya, D.A., 2010. Magmatic lobes

as "snapshots" of magma chamber growth and evolution in large, composite batholiths: An example from the Tuolumne intrusion, Sierra Nevada, California.

Geological Society of America Bulletin, 122, pp. 1912-1931.

Miller, C. F. & Bradfish, L. J., 1980. An inner Cordilleran belt of muscovite-bearing plutons. Geology, 8, pp. 412-416.

Miller, C.F., Wooden, J. L., Bennett, V. C., Wright, J. E., Solomon, G. C., & Hurst, R. W.,

1990. Petrogenesis of the composite peraluminous-metaluminous Old Woman-Piute range batholith, southeastern California: isotopic constraints. In: J. Anderson,

ed, Geological Society of America Memoirs, pp. 99-109.

Miller, C. F., Hanchar, J.M., Wooden, J.L., Bennett, V.C., Harrison, M.T., Wark, D.A., &

Foster, D.A., 1992. Source region of a granite batholith: evidence from lower crustal xenoliths and inherited accessory minerals. Earth and Environmental Science Transactions of the Royal Society of Edinburgh, 83, pp. 49-62.

Miller, C. F. & Wooden, J. L., 1994. Anatexis, hybridization and the modification of ancient crust: Mesozoic plutonism in the Old Woman Mountains area, California.

Lithos, 32, pp. 111-133.

Miller, C. F., McDowell, S. & Mapes, R., 2003. Hot and cold granites: Implications of zircon saturation temperatures and preservation of inheritance. *Geology*, 31, pp. 529-532.

Miller, J. S., Glazner, A.F., Lang Farmer, G., Suayah, I.B., & Keith, L.A., 2000. A Sr, Nd, and Pb isotopic study of mantle domains and crustal structure from Miocene volcanic rocks in the Mojave Desert, California. *Geological Society of America Bulletin*, 112, pp. 1264-1279.

Miller, J.S., Matzel, J.E.P., Miller, C.F., Burgess, S.D., & Miller, R.B., 2007. Zircon growth and recycling during the assembly of large, composite arc plutons. *Journal of Volcanology and Geothermal Research*, 167, pp. 282-299.

Mittlefehldt, D. W. & Miller, C. F., 1983. Geochemistry of the Sweetwater Wash Pluton, California: Implications for "anomalous" trace element behavior during differentiation of felsic magmas. *Geochimica et Cosmochimica Acta*, 47, pp. 109-124.

Montel, J.-M., 1993. A model for monazite/melt equilibrium and application to the generation of granitic magmas. *Chemical Geology*, 110, pp. 127-146.

Nemchin, A. A., Horstwood, M. S. A. & Whitehouse, M. J., 2013. High-Spatial-Resolution Geochronology. *Elements*, 9, pp. 31-37.

Paces, J. B. & Miller, J. D., 1993. Precise U-Pb ages of Duluth Complex and related mafic intrusions, northeastern Minnesota: Geochronological insights to physical, petrogenetic, paleomagnetic, and tectonomagmatic processes associated with the 1.1 Ga Midcontinent Rift System. *Journal of Geophysical Research*, 98, pp. 13997-14013.

Parrish, R.R., 1990. U-Pb dating of monazite and its application to geological problems. *Canadian Journal of Earth Science*, 27, pp. 1431-1450.

Patchett, P. & Tatsumoto, M., 1981. A routine high-precision method for Lu-Hf isotope geochemistry and chronology. *Contributions to Mineralogy and Petrology*, 75, pp. 263-267.

Paterson, S. R. & Tobisch, O. T. 1992. Rates of processes in magmatic arcs; implications for the timing and nature of pluton emplacement and wall rock deformation. *Journal of Structural Geology* 14, pp. 291–300.

Paton, C., Hellstrom, J., Paul, B., Woodhead, J., & Hergt, J., 2011. Iolite: Freeware for the visualisation and processing of mass spectrometric data. *Journal of Analytical Atomic Spectrometry*, 26, pp. 2508-2518.

Putnis, A., 2002. Mineral replacement reactions: from macroscopic observations to microscopic mechanisms. *Mineralogical Magazine*, 66, pp. 689-708.

Putnis, A., 2009. Mineral replacement reactions. In: Oelkers, E. H. & Schott, J. Eds., *Thermodynamics and Kinetics of Water-Rock Interaction*. Reviews in Mineralogy and Geochemistry, 70, pp. 87-124.

Putnis, C.V., & Ruiz-Agudo, E., 2013. The mineral-water interface: Where minerals react with the environment. Elements, 9, pp.177-182.

Raczek, I., Jochum, K. P. & Hofmann, A. W., 2003. Neodymium and Strontium Isotope Data for USGS Reference Materials BCR-1, BCR-2, BHVO-1, BHVO-2, AGV-1, AGV-2, GSP-1, GSP-2 and Eight MPI-DING Reference Glasses. Geostandards Newsletter, 27, pp. 173-179.

Rapp, R. P. & Watson, E. B., 1986. Monazite solubility and dissolution kinetics: implications for the thorium and light rare earth chemistry of felsic magmas. 94, pp. 304-316.

Rehkämper, M. & Hofmann, A., 1997. Recycled ocean crust and sediment in Indian Ocean MORB. Earth and Planetary Science Letters, 147, pp. 93-106.

Schaltegger, U., Fanning, C.M., Günther, D., Maurin, J.C., Schulmann, K., & Gebauer, D., 1999. Growth, annealing and recrystallization of zircon and preservation of monazite in high-grade metamorphism: conventional and in-situ U-Pb isotope, cathodoluminescence and microchemical evidence. Contributions to Mineralogy and Petrology, Volume 134, pp. 186-201.

Scherer, E.E., Cameron, K.L., & Blichert-Toft, J., 2000. Lu-Hf garnet geochronology: closure temperature relative to the Sm-Nd system and the effects of trace mineral inclusions. *Geochemica et Cosmochimica Acta*, 64, pp. 3413-3432.

Schoene, B., Crowley, J.L., Condon, D.J., Schmitz, M.D., & Bowring, S.A., 2006. Reassessing the uranium decay constants for geochronology using ID-TIMS U-Pb data. *Geochimica et Cosmochimica Acta*, 70, pp. 426-445.

Schoene, B., Schaltegger, U., Brack, P., Latkoczy, C., Stracke, A., & Günther, D., 2012. Rates of magma differentiation and emplacement in a ballooning pluton as recorded by U-Pb TIMS-TEA, Adamello batholith, Italy. *Earth and Planetary Science Letters*, 355-356, pp. 162-173.

Schoene, B., Condon, D.J., Morgan, L., & Mclean, N., 2013. Precision and Accuracy in Geochronology. *Elements*, 9, pp. 19-24.

Seydoux-Guillaume, A.-M., Goncalves, G., Wirth, R., & Deutsch, A., 2003. Transmission electron microscope study of polyphase and discordant monazites: Site-specific specimen preparation using the focused ion beam technique. *Geology*, 31, pp. 973.

Sláma, J., Košler, J., Condon, D.J., Crowley, J.L., Gerdes, A., Hanchar, J.M., Horstwood, M.S.A., Morris, G.A., Nasdala, L., Norberg, N., Schaltegger, U., Schoene, B., Tubrett, M.N., & Whitehouse, M.J., 2008. Plešovice zircon - A new natural reference material for U-Pb and Hf isotopic microanalysis. *Chemical Geology*, 249, pp. 1-35.

Söderlund, U., Patchett, P., Vervoort, J. D. & Isachsen, C. E., 2004. The ^{176}Lu decay constant determined by Lu-Hf and U-Pb isotope systematics of Precambrian mafic intrusions. *Earth and Planetary Science Letters*, 219, pp. 311-324.

Steiger, R. & Jäger, E., 1977. Subcommission on geochronology: Convention on the use of decay constants in geo- and cosmochronology. *Earth and Planetary Science Letters*, 36, pp. 359-362.

Strickland, A., Wooden, J.L., Mattinson, C.G., Ushikubo, T., Miller, D.M., & Valley, J.W., 2013. Proterozoic evolution of the Mojave crustal province as preserved in the Ivanpah Mountains, southeastern California. *Precambrian Research*, 224, pp. 222-241.

Tanaka, T., Togashi, S., Kamioka, H., Amakawa, H., Kagami, H., Hamamoto, T., Yuhara, M., Orihashi, Y., Yoneda, S., Shimuzu, H., Kunimaru, T., Takahashi, K., Yanagi, T., Nakano, T., Fujimaki, H., Shinjo, R., Asahara, Y., Tanimizu, M., & Dragusanu, C., 2000. JNdI-1: a neodymium isotopic reference in consistency with La Jolla neodymium. *Chemical Geology*, 168, pp. 279-281.

Tang M., Wang X.-L., Shu X.-J., Wang D., Yang T., & Gopon P., 2014. Hafnium isotopic heterogeneity in zircons from granitic rocks: Geochemical evaluation and modeling of “zircon effect” in crustal anatexis. *Earth and Planetary Science Letters*, 389, pp. 188–199.

Tomascak, P. B., Krogstad, E. J. & Walker, R. J., 1996. U-Pb Monazite Geochronology of Granitic Rocks from Maine: Implications for Late Paleozoic Tectonics in the Northern Appalachians. *The Journal of Geology*, 104, pp. 185-195.

Tomascak, P. B., Krogstad, E. J. & Walker, R. J., 1998. Sm-Nd isotope systematics and the derivation of granitic pegmatites in southwestern Maine. *The Canadian Mineralogist*, 36, pp. 327-337.

Townsend, K. et al., 2001. Low temperature replacement of monazite in the Ireteba granite, Southern Nevada: geochronological implications. *Chemical Geology*, 172, pp. 95-112.

Vervoort, J. D. & Blichert-Toft, J., 1999. Evolution of the depleted mantle: Hf isotope evidence from juvenile rocks through time. *Geochimica et Cosmochimica Acta*, 63, pp. 533-556.

Vervoort, J. D. & Jonathan Patchett, P., 1996. Behavior of hafnium and neodymium isotopes in the crust: Constraints from Precambrian crustally derived granites. *Geochimica et Cosmochimica Acta*, 60, pp. 3717-3733.

Vervoort, J. D., Patchett, P. J., Söderlund, U. & Baker, M., 2004. Isotopic composition of Yb and the determination of Lu concentrations and Lu/Hf ratios by isotope dilution using MC-ICPMS. *Geochem. Geophys. Geosyst.*, 5, pp. Q11002.

Villaros, A., Buick, I.S., & Stevens, G., 2011. Isotopic variations in S-type granites: an inheritance from a heterogeneous source? Contributions to Mineralogy and Petrology, 163, pp. 243-257.

Walker, J.D., 1998, Permian and Triassic rocks of the Mojave Desert and their implications for timing and mechanisms of continental truncation. Tectonics, 7, pp. 685-709.

Wark, D. A. & Miller, C. F., 1993. Accessory mineral behavior during differentiation of a granite suite: monazite, xenotime and zircon in the Sweetwater Wash pluton, southeastern California, U.S.A. Chemical Geology, 110, pp. 49-67.

Watson, E. B. & Harrison, T. M., 1983. Zircon saturation revisited: temperature and composition effects in a variety of crustal magma types. Earth and Planetary Science Letters, 6, pp. 295-304.

Watson, B.E., Vicenzi, E.P., & Rapp, R.P. 1989. Inclusion/host relations involving accessory minerals in high-grade metamorphic and anatetic rocks. Contributions to Mineralogy and Petrology, 101 , pp. 220-231.

Wiedenbeck, M., Allé, P., Corfu, F., Griffin, W.L., Meier, M., Oberli, F., Von Quadt, A., Roddick, J.C., & Spiegel, W., 1995. Three Natural Zircon Standards for U-Th-Pb, Lu-Hf, Trace Element and REE Analyses. Geostandards Newsletter, 19, pp. 1-23.

Williams, M. L. & Jercinovic, M. J., 2012. Tectonic interpretation of metamorphic tectonites: integrating compositional mapping, microstructural analysis and *in situ* monazite dating. *Journal of Metamorphic Geology*, 30, pp. 739-752.

Williams, M. L., Jercinovic, M. J. & Hetherington, C. J., 2007. Microprobe Monazite Geochronology: Understanding Geologic Processes by Integrating Composition and Chronology. *Annual Review of Earth and Planetary Sciences*, 35, pp. 137-175.

Wooden, J. L. & Miller, D. M., 1990. Chronologic and isotopic framework for Early Proterozoic crustal evolution in the eastern Mojave Desert Region, SE California. *Journal of Geophysical Research: Solid Earth*, 95, pp. 20133-20146.

Woodhead, J. D. & Herzt, J. M., 2005. A Preliminary Appraisal of Seven Natural Zircon Reference Materials for *In situ* Hf Isotope Determination. *Geostandards and Geoanalytical Research*, 29, pp. 183-195.

Woodhead, J.D., Herzt, J. M., Shelley, M., Eggins, S., & Kemp, R., 2004. Zircon Hf-isotope analysis with an excimer laser, depth profiling, ablation of complex geometries, and concomitant age estimation. *Chemical Geology*, 209, pp. 121-135.

Xie, L. et al., 2008. *In situ* simultaneous determination of trace elements, U-Pb and Lu-Hf isotopes in zircon and baddeleyite. *Chinese Science Bulletin*, Volume 53, pp. 1565-1573.

Xiong, Q., Zheng, J., Griffin, W.L., O'Reilly, S.Y., & Pearson, N.J., 2013. Decoupling of U-Pb and Lu-Hf isotopes and trace elements in zircon from the UHP North Qaidam orogen, NE Tibet (China): tracing the deep subduction of continental blocks. *Lithos*, 155, pp. 125-145.

Yuan, H.L., Gao, S., Dai, M.-N., Zong, C.-L., Günther, Fontaine, G.H., Liu, X.-M., & Diwu, C., 2008. Simultaneous determinations of U-Pb age, Hf isotopes and trace element compositions of zircon by excimer laser-ablation quadrupole and multiple-collector ICP-MS. *Chemical Geology*, 247, pp. 100-118.

Appendix A - Analytical Methods

A.1 - Analytical Methods: Whole Rock

A.2 - Major and trace elements

A.2.1 - Crushing

Representative hand samples were kept for each sample and thin sections prepared. Between 0.5 and 1.0kg of material was crushed using a jaw crusher into mm-sized chips and pulverised using a disk mill to <500 µm, with material >63 µm removed by sieving. Whole rock powders (~100µm) were then produced for all 11 samples using a tungsten carbide shatter box at Memorial University. Crushed samples were then split into three portions; one for archive, one for whole rock geochemistry and one for mineral separation.

A.2.2 - Whole rock major and trace elements

From the whole rock geochemistry portion, a further split was made for elemental and isotopic analysis. Major and trace elements were analysed at Activation Laboratories Ltd., Ontario, Canada in accordance with the 4Lithores protocol. A Lithium Metaborate/Tetraborate Fusion ICP and ICP-MS technique was used. Comparison with a variety of laboratory standards suggest an accuracy of < 3% for major elements and < 7% for trace elements.

A.3 - Whole rock isotopes

A.3.1 - Whole rock isotope column chemistry (MUN)

Sm, Nd, Sr, Lu & Hf were separated from whole rock powders using standard column chemistry techniques. Procedures follow a well established “in house” protocol and are described in brief below.

A.3.2 - Sm-Nd & Sr column chemistry (MUN)

To prepare samples for ^{147}Sm - ^{143}Nd analysis a mixed $^{150}\text{Nd}/^{149}\text{Sm}$ spike is added to the whole rock samples, with spike weights based on the Nd elemental concentrations as determined above. Both spike and sample weights are measured using a high-precision balance. The spiked powders are then dissolved in Savillex © Teflon beakers in a 4:1 mixture of 29M Hf – 15M HNO_3 and left on a hotplate to dissolve for five to six days. The solution is then evaporated to dryness and then redissolved in 6M HCl for two to three days. After this solution has been dried down it is then finally redissolved in 2.5M HCl. Sm and Nd are then separated using a conventional two-column chemistry technique. Samples are loaded into a column containing cation exchange resin Bio-Rad AG-50W-X8 (200-400 mesh). A Sr fraction is isolated before extraction of a bulk REE separation. This fraction is then dried down and redissolved in 0.18M HCl before being loaded into a second column containing Eichrom © Ln resin (50-100 mesh). Sm and Nd can then be isolated from the other REEs. The isolated Sr fraction is then further refined using micro-columns with Eichrom © Sr-spec resin and HNO_3 .

A.3.3 - Sm-Nd & Sr TIMS analysis (MUN)

Sm and Nd, and Sr isotopic compositions and concentrations were determined using a multi-collector Finnigan Mat 282 mass spectrometer at Memorial University of Newfoundland, using static and dynamic modes respectively. Sm and Nd are loaded onto a double rhenium filament assembly while Sr utilizes a single tungsten filament with 2 µL of Sr activator (Tantalum fluoride). Sm and Nd analyses were corrected for internal mass fractionation using a Rayleigh law relative to $^{146}\text{Nd}/^{144}\text{Nd} = 0.7219$ and $^{152}\text{Sm}/^{147}\text{Sm} = 1.783$, as well as gain. Measured values were then adjusted to the JNd-1 standard isotopic value of $^{143}\text{Nd}/^{144}\text{Nd} = 0.512115$ (Tanaka et al., 2000). Our current measurement of JNd-1 yields an average of 0.512100 ± 7 (1 std, n=21). Sr ratios are normalized to $^{88}\text{Sr}/^{86}\text{Sr} = 8.375202$ and measured values are adjusted to the NBS-987 standard. Our current measurement of this standard has a mean $^{87}\text{Sr}/^{86}\text{Sr} = 0.710233 \pm 15$ (1 std, n=15).

A.3.4 - Lu-Hf column chemistry (MUN)

The procedures to prepare samples for $^{176}\text{Lu}-^{176}\text{Hf}$ analysis have been described in detail elsewhere (Patchett & Tatsumoto, 1981; Vervoort & Blichert-Toft, 1999; Vervoort et al., 2004) and will only be described briefly here. Whole rock powders are first spiked using $^{176}\text{Lu}-^{180}\text{Hf}$ mixed spikes as outlined in (Vervoort, et al., 2004) with spikes used i.e. mafic, felsic, garnet etc. dependant on the Lu/Hf ratio of the sample as determined as above. These mixtures were then digested in a 3:1 mixture of 29M HF – 15M HNO₃ in steel jacketed PTFE dissolution vessels (Parr type) for five to seven days.

After acid digestion the samples were evaporated to dryness in Savilex © Teflon beakers before being redissolved in 6M HCl for two days, evaporated to dryness again, and further dissolved in 1M HCl – 0.1M HF. The samples are then ready for the first of a multiple stage column separation. The first column containing Bio-Rad AG 50W-X12 resin involves the removal of the high field strength elements (HFSE, including Hf) from the heavy REEs (HREEs, including Lu and Yb). The HFSE split is then introduced to a second column containing LN Spec resin and Ti is removed from the samples using 0.09Hcit-0.45M HNO₃ + 1% H₂O₂. Hf is eluted using 6M HCl – 0.4M HF and is then dried down for a further Hf clean-up procedure using AG 50W-X12 resin. Yb is isolated from the HREE split in a column containing LN spec resin with Yb being removed by 2.5M HCl and Lu being eluted by 6.2M HCl.

A.3.5 - Lu-Hf MC-ICP-MS analysis (MUN)

Lu-Hf isotopic analyses were undertaken using a Thermo-Finnigan Neptune multi-collector (MC-ICP-MS) system at Memorial University of Newfoundland. Elements were measured in static mode and sample input rate was typically ~50µl/min. All solutions were run in 2% HNO₃. Hf analyses consisted of one block of 75 cycles, whereas Lu analyses consisted of one block of 30 cycles, both using ~8 second integrations. After Hf analysis the spray chamber was rinsed first with 0.1% HF and then equilibrated in 0.3N HNO₃. If Hf signals were high 0.2N HCl was used additionally in between the HF and HCl steps. For Lu analysis the spray chamber was rinsed with 2N HCl and then equilibrated in 0.3N HNO₃.

Measurements were bracketed every five samples by three analyses of a 202ppb JMC-475 Hf standard, which averaged $^{176}\text{Hf}/^{177}\text{Hf}=0.282154 \pm 12$ (2 std, n=22) over two analytical sessions. Mass bias- and interference corrected were then adjusted to the JMC-475 accepted values of $^{176}\text{Hf}/^{177}\text{Hf}=0.282160$, $^{178}\text{Hf}/^{177}\text{Hf}=1.467170$ and $^{180}\text{Hf}/^{177}\text{Hf}=1.886660$ (Vervoort & Blichert-Toft, 1999). All Hf compositions were corrected for Lu and Yb interferences. Mass fractionation and interference corrections were applied to the Lu analyses following the protocol described in (Vervoort et al., 2004).

A.4 - Analytical Methods: In Situ

In situ analyses of the OWPB accessory minerals were done using a combination of methods. Zircon analyses were done by analysing for U-Pb isotopes first and then locating Lu-Hf analyses in the same spot or zone. The LASS method (described below) was utilised to investigate the U-Pb and Sm-Nd isotopes in monazite. A U-Pb and Lu-Hf LASS approach was also used on some of the zircon samples.

A.4.1 - LASS setup (WSU)

The LASS method used in this study used a New Wave 213 nm Nd:YAG laser coupled to both a ICP-MS and a MC-ICP-MS, which measured the U-Pb isotopes and the Sm-Nd/Lu-Hf isotopes, respectively. The relative elemental concentrations of Ce, Eu and Gd were also simultaneously measured in monazite using the MC-ICP-MS. A baffled "Y" glass connector is used to split the ablated material after transportation from the sample cell to both mass spectrometers. He gas was used as the sample carrier, and N₂

is added before the splitting of the sample in order to increase the sensitivity and minimize oxide formation. For both zircon and monazite LASS methods, the tracer isotopic data (Lu-Hf and Sm-Nd respectively) were acquired using continuous, single data files that contain a number of individual ablation analyses and baselines. This simplifies data collection and allows the user to focus primarily on the single-collector ICP-MS and the laser interfaces.

A.4.2 - U-Pb zircon analysis (Portsmouth)

U-Pb ages were measured by laser ablation quadrupole mass spectrometry (LA-Q-ICP-MS) after ([Jeffries, et al., 2003](#)), using an Agilent 7500cs coupled to a New Wave Research UP-213 Nd:YAG laser at the University of Portsmouth. Spots 20-30 µm in diameter were rastered along lines 1.5-2x that length.

Ratios were calculated using LamTool ([Košler et al., 2008](#)) normalized to Plešovice through sample-standard bracketing. Rims, as determined by CL imaging, were analysed preferentially to obtain a crystallisation age for the granite. The amount of ^{204}Pb in these analyses was below the detection limit, and no common Pb correction was undertaken. Only ages less than 5% discordant, from a single growth zone and avoiding irregular features such as cracks and inclusions were considered for interpretation. Instrument parameters are described in [Table A.4.2.1](#).

Table A.4.2.1 –Zircon U–Pb operating parameters and data acquisition parameters (Portsmouth)

Unit	Parameter	Settings
ICP-MS	Model	Agilent 7500cs Quadrupole
	Forward power	1550W
	Coolant gas flow	Ar, 15 L/min
	Auxiliary gas flow	Ar, 1.0 L/min
	Carrier gas flow	Ar, c. 1.25 L/min
Laser	Model	NewWave Research UP213 Nd:YAG
	Wavelength	213 nm
	Pulse width	3 ns
	Fluence	c. 4.4 J/cm ²
	Repetition rate	10 Hz
	Spot size	30 µm
	Raster length	45-60 µm
	Raster speed	2 µm/s
	Cell format	'tear drop' low volume cell (c. 2.6 cm ³)
Analytical protocol	Carrier gas flow	He, 0.3 L/min
	Scanning mode	Peak jumping, 1 point/peak
	Acquisition mode	Time-resolved analysis
	Detection	Single electron multiplier
	Masses measured	202, 204, 206, 207, 208, 235, 238
	Integration per peak	20 ms on 202, 204, 207, 235; 10 ms on 206, 232, 238
	Total integration per reading	0.134s
	Ablation duration	60s
	Gas blank	30s on-peak zero subtracted
	Calibration	Plešovice (primary); GJ-1 (internal)
	Standard references:	91500: (Wiedenbeck, et al., 1995); GJ-1: (Jackson, et al., 2004) Plešovice: (Sláma, et al., 2008)
	Data processing package:	LAMTRACE or LamTool
	Mass discrimination	$^{207}\text{Pb}/^{206}\text{Pb}$ and $^{206}\text{Pb}/^{238}\text{U}$ normalised to reference material
	Common-Pb correction, composition and uncertainty	None applied

	Uncertainty level and propagation	Ages are quoted at 2σ absolute; propagation is by quadratic addition. Reproducibility and age uncertainty of reference materials are not propagated.
--	-----------------------------------	---

A.4.3 - Lu-Hf & LASS zircon analyses (WSU)

Samples determined to have concordant U-Pb analyses were then analysed for Lu-Hf using a New Wave 213nm Nd:YAG laser coupled to a ThermoFinnigan Neptune MC-ICP-MS at Washington State University. Two samples (SWP-13-01 & PRP-12-01) were additionally analysed for both U-Pb and Lu-Hf at Washington using the LASS method. Operating parameters for the Neptune are the same for both the Lu-Hf analyses and the LASS method, as those reported in Fisher et al., (2014). For the zircon LASS analyses, after the sample was split to analyse Lu-Hf using a Neptune MC-ICP-MS, the U-Pb was measured simultaneously using a Thermo Element2 (parameters also outlined in (Fisher, et al., 2014)). In both Lu-Hf analyses and LASS analyses the laser operated at 10Hz and a fluence of \sim 8 – 10 J/cm³, using a 30-40 μ m spot size. To further improve sensitivity of Lu-Hf analyses the Neptune is also fitted with a standard nickel sample cone and a nickel “X” skimmer cone, which has been shown to improve sensitivity by a factor of \sim 1.4 (Hu et al., 2012). The zircon LASS operating parameters are summarised in [Table A.4.3.1](#).

Table A.4.3.1 – Zircon LASS operating parameters (WSU).

(a) Cup Configuration and interferences								
L4	L3	L2	L1	Axial	H1	H2	H3	H4
^{171}Yb	^{173}Yb	^{175}Lu	^{176}Yb ^{176}Lu	^{176}Hf ^{177}Hf	^{178}Hf	^{179}Hf	^{180}Hf ^{180}W	^{182}W
REE-oxides	$^{155}\text{Gd}^{16}\text{O}$	$^{157}\text{Gd}^{16}\text{O}$	$^{159}\text{Tb}^{16}\text{O}$	$^{160}\text{Gd}^{16}\text{O}$	$^{161}\text{Dy}^{16}\text{O}$	$^{162}\text{Dy}^{16}\text{O}$ $^{162}\text{Er}^{16}\text{O}$	$^{163}\text{Dy}^{16}\text{O}$	$^{164}\text{Dy}^{16}\text{O}$ $^{164}\text{Er}^{16}\text{O}$
(b) Instrument Operating Parameters								
	MC-ICPMS	Sector Field-Inductively Coupled Plasma Mass Spectrometer						
Model	ThermoFinnigan Neptune	ThermoFinnigan Element2						
Forward power	1200 W							
Mass resolution	Low (400)	Low						
<i>Gas flows-laser ablation</i>								
Cool/plasma (Ar)	16 l/min	0.85 l/min						
Auxiliary (Ar)	0.85 l/min	0.85 l/min						
Sample/nebulizer (Ar)	~0.60 l/min	1 l/min						
Carrier gas (He)	~1.2 l/min	~1.2 l/min						
Nitrogen	5 ml/min	5 ml/min						
<i>Laser ablation</i>								
Type	New wave 213 nm (Nd:YAG)	Masses ^{204}Pb , ^{206}Pb , ^{208}Pb , ^{232}Th , ^{235}U , ^{238}U Points per peak 1						
Repetition rate	10 Hz							
Laser fluence	~8 J/cm ²							
Spot size	30–40 μm							

A.4.4 - Zircon data reduction

A.4.4.1 - Lu-Hf

Lu-Hf data reduction follows that of (Fisher et al., 2011; Fisher et al., 2014) using the Iolite software program (Paton et al., 2011) with a customized in-house protocol. The isobaric ^{176}Yb interference on ^{176}Hf is the most important correction that must be made for *in situ* Hf isotopic analysis (Woodhead et al., 2004) and a detailed explanation of this correction is discussed in Fisher et al., (2011) and Fisher et al., (2014). Samples are then further calibrated to ^{176}Hf - ^{176}Hf value of 0.282507 ± 6 for the Mud Tank zircon standard (Woodhead & Hergt, 2005).

A.4.4.2 - LASS U-Pb

The U-Pb LASS zircon data were reduced using the data reduction protocol outlined by (Chang et al., 2006) and discussed in (Fisher et al., 2014). Analyses of unknowns were bracketed by analyses of standards, with ten unknowns followed by five analyses of two different zircon standards (FC-1 & Plešovice). To adequately account for the range of ages expected in the OWPB samples, the Plešovice standard (337 Ma; Sláma et al., 2008) was used to calibrate the ^{238}U - ^{206}Pb ages, whereas the older FC-1 standard (1099 Ma; Paces & Miller, 1993) was used for the ^{207}Pb - ^{206}Pb ages.

A.4.5 - Monazite LASS (WSU)

All monazite samples were analysed using the LASS technique at Washington State University. Like for the LASS zircon analyses, the ablated sample is carried from the laser cell using He + N₂ and then split to the Element 2 HR-ICP-MS where U-Pb isotopes

are measured, and the Neptune MC-ICP-MS where Sm and Nd isotopes are measured. The laser is operated at 8Hz, $\sim 7\text{J/cm}^2$, with a spot size of 20 μm , allowing for high spatial resolution analyses. This is a higher laser power than that used in both Fisher et al., (2011) & Goudie et al., (2014) who used a lower power to minimise U and Pb elemental fractionation, and to conserve the amount of sample consumed. We experimented with using the laser at 4Hz however we did not see any difference in signal intensity or uncertainty, thus we continued to use the laser at 8Hz.

Analysis of the LREE and JNd_i glass standards required a spot size of 80 μm and 60 μm respectively, due to the lower concentration of Sm and Nd present. While it is preferable to analyse standards and unknowns using the same spot size in order to eliminate any laser induced fractionation, it was not possible using these reference materials. The fractionation between Sm and Nd is thought to be negligible (<1%) however, therefore this difference in spot size does not cause any significant increases in uncertainty (Fisher et al., 2011).

The operating parameters for the LASS monazite analyses are summarised in Table A.4.5.1.

Table A.4.5.1 – Monazite LASS operating parameters (WSU).

(a) Cup Configuration and interferences														
	L4	L3	L2	L1	Axial	H1	H2	H3	H4					
Analyte	^{142}Nd	^{143}Nd	^{144}Nd	^{145}Nd	^{146}Nd	^{147}Sm	^{149}Sm	^{153}Eu	^{157}Gd					
Interferences	^{144}Sm								$^{141}\text{Pr}^{16}\text{O}$					
(b) Instrument Operating Parameters														
	MC-ICPMS				Sector Field-Inductively Coupled Plasma Mass Spectrometer									
Model	ThermoFinnigan Neptune				ThermoFinnigan Element2									
Forward power	1200 W													
Mass resolution	Low (400)				Low									
<i>Gas flows-laser ablation</i>														
Cool/plasma (Ar)	15 l/min				16 l/min									
Auxiliary (Ar)	0.80 l/min				0.85 l/min									
Sample/nebulizer (Ar)	0.7-0.8 l/min				1.21 l/min									
Carrier gas (He)	\sim 1 l/min				1.12 l/min									
Nitrogen	5 ml/min				5 ml/min									
<i>Laser ablation</i>														
Type	New wave 213 nm (Nd:YAG)				Masses ^{204}Pb , ^{206}Pb , ^{208}Pb , ^{232}Th , ^{235}U , ^{238}U Points per peak 1									
Repetition rate	8 Hz													
Laser fluence	\sim 7 J/cm ²													
Spot size	20 μm													

A.4.6 - Monazite LASS data reduction

A.4.6.1 - Sm-Nd

Monazite Sm-Nd data was reduced using Iolite software (University of Melbourne) with a customized in-house protocol that follows the scheme outlined in (Fisher et al., 2011). There are three main corrections required for precise and accurate Sm-Nd isotopic analyses by LA-ICP-MS, as discussed at length in Fisher et al., (2011). The isobaric interference of ^{144}Sm on ^{144}Nd is corrected using the measured ^{149}Sm and the natural invariant ratio of $^{144}\text{Sm}/^{149}\text{Sm}$ (Iizuka et al., 2011; Fisher et al., 2011). Sm mass bias is corrected using an exponential law and the measured $^{147}\text{Sm}/^{149}\text{Sm}$ from the sample (Fisher et al., 2011; Goudie et al., 2014). The accurate determination of $^{147}\text{Sm}/^{144}\text{Nd}$ is necessary when investigating variations in the initial Nd compositions of minerals, and this becomes increasingly important as sample age increases. This is achieved by calibration of measured Sm-Nd isotopic values to the LREE haploandesite glass standard (Fisher et al., 2011) that was analysed after every six unknowns, allowing for simultaneous correction of instrumental drift, elemental fractionation and mass bias. Correction of $^{143}\text{Nd}/^{144}\text{Nd}$ ratios was made in reference to the value of 0.512155 ± 7 (Tanaka et al., 2000).

A.4.6.2 - U-Pb

The U-Pb LASS monazite data, like the U-Pb LASS zircon data, was reduced using the data reduction protocol outlined by Chang et al., (2006). Trebilcock (272 ± 2 Ma;

Tomasca et al., 1998) was used as U-Pb calibration material, as well as being used as a secondary standard to assess the accuracy of the Sm-Nd isotopic analyses.

A.5 - Isotopic reservoir values

CHUR and Depleted Mantle (DM) reservoir parameters used for both whole rock and *in situ* data are as follows. ϵ_{Hf} values were calculated using the present day CHUR values of $^{176}\text{Hf}/^{177}\text{Hf} = 0.282785$ and $^{176}\text{Lu}/^{177}\text{Hf} = 0.0336$ (Bouvier et al., 2008). ϵ_{Nd} values were calculated using the present day CHUR values of $^{143}\text{Nd}/^{144}\text{Nd} = 0.512630$ and $^{147}\text{Sm}/^{144}\text{Nd} = 0.1960$ (Bouvier et al., 2008). Depleted mantle lines were calculated using $^{176}\text{Hf}/^{177}\text{Hf} = 0.283225$ and $^{176}\text{Lu}/^{177}\text{Hf} = 0.038512$ (Vervoort & Blachert-Toft, 1999), and $^{143}\text{Nd}/^{144}\text{Nd} = 0.513200$ and $^{147}\text{Sm}/^{144}\text{Nd} = 0.2140$ (Rehkämper & Hofmann, 1997).

Initial isotopic values for whole rock and *in situ* Nd and Hf isotopes were calculated using measured parent-daughter ratios. The corresponding *in situ* age information was provided by U-Pb measurements made by either the LASS method or by the U-Pb only method. For whole rock Sr isotopes, $^{87}\text{Rb}/^{86}\text{Sr}$ ratios were calculated using the method described in (Faure & Mensing 2005) using the Rb and Sr elemental concentrations as determined by ICP-MS as described above. Decay constants used were $^{176}\text{Lu } \lambda = 1.867 \times 10^{-11}$ (Söderlund et al., 2004), $^{147}\text{Sm } \lambda = 6.539 \times 10^{-12}$ (Begemann et al., 2001), and $^{87}\text{Rb } \lambda = 1.42 \times 10^{-11}$ (Steiger & Jäger, 1977). Whole rock Sr, Sm-Nd and Lu-Hf initial compositions were calculated using an age of 70 Ma, as this allows easier comparison to previous datasets. There is no significant difference in initial compositions

if the crystallisation age of each sample, as determined by weighted average U-Pb *in situ* data, is used.

Appendix B - Analysis of reference standards

B.1 - Whole rock isotopic standards

To assess the precision of the Sm-Nd SIMS technique the USGS BCR-2 standard ($^{143}\text{Nd}/^{144}\text{Nd} = 0.512633$; Raczek et al., 2003) was measured throughout the analysis period, with each analysis comprising a separate dissolution. Our average measurement of the BCR-2 is 0.512636 ± 7 (2 std, n=11). Internal errors (2 standard errors of the mean) are typically <0.002% for Nd isotope compositions, and <0.1% for the $^{147}\text{Sm}/^{144}\text{Nd}$ ratios. The average total blank measured at the MUN TIMS laboratory was 100pg for Nd and therefore is considered negligible.

Precision of the Sr TIMS procedure was assessed by analysis of the NBS 897 standard, which has a reference value of 0.710240. 15 measurements of this standard at the MUN TIMS lab throughout the analysis period yielded an average $^{87}\text{Sr}/^{86}\text{Sr} = 0.710233 \pm 15$ (2std, n=15), which is in excellent agreement with the accepted value.

The precision of the Hf ICP-MS technique was assessed by analysis of the USGS BCR-2 standard ($^{176}\text{Hf}/^{177}\text{Hf} = 0.282862$; Vervoort et al., 2004) throughout the analysis period, with each analysis comprising a separate dissolution. Our average measurement of the BCR-2 is 0.282863 ± 3 (2 std, n=6).

B.2 - In situ isotopic standards

B.2.1 - U-Pb only standards (UoP)

The Plešovice standard was used in order to normalise U-Pb ratios, with analyses yielding an average $^{206}\text{Pb}/^{238}\text{U}$ age of 336.4 ± 1.0 Ma ($n=64$, 2SD) over 4 days, consistent with the published age of 337.1 ± 0.37 Ma (2SD; Sláma et al., 2008) (Figure B.2.1.1a). Internal zircon standard GJ-1 yielded an average $^{206}\text{Pb}/^{238}\text{U}$ age of 600.29 ± 0.96 Ma ($n=192$, 2SD), within uncertainty of the 600.4 ± 1.3 Ma published age (2SD; Jackson et al., 2004) (Figure B.2.1.1b).

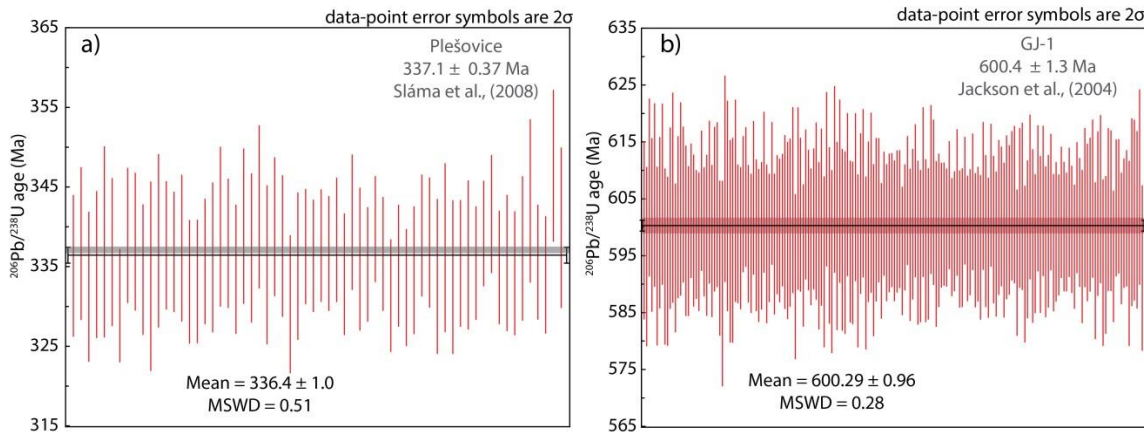


Figure B.2.1.1 – Weighted average plots of Plešovice and GJ-1 standard U-Pb analyses.
Coloured bars represent accepted values of standards.

B.2.2 - Lu-Hf only standards (WSU)

For Lu-Hf only zircon analyses, two standards were measured during the analytical session at Washington State University. The Mud Tank standard was used as the internal normalising standard, using the values of 0.282507 ± 6 (Woodhead & Hergt,

2005). The synthetic B144/MunZirc standard was also analysed to assess the accuracy of the technique. This yielded a weighted average of $^{176}\text{Hf} - ^{176}\text{Hf} = 0.282139 \pm 11$ ($n= 6$, 2SE; accepted value = 0.282135 ± 7 ; (Fisher et al., 2011)) (Figure B.2.2.1).

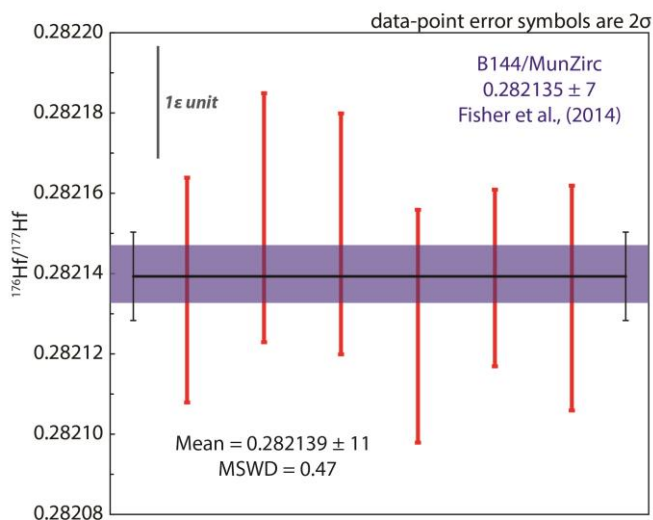


Figure B.2.2.1 – Weighted average plots of B144/MunZirc standard Lu-Hf analyses.
Coloured bars represent accepted values of standards.

B.2.3 - LASS zircon standards

For the LASS zircon analyses a number of reference zircons were used covering the range of natural zircon compositions expected from the OWP samples.

Plešovice was used as the U-Pb internal standard and therefore it is not possible to make an assessment of accuracy for its LASS age determinations. A weighted average of $^{176}\text{Hf} - ^{176}\text{Hf} = 0.282460 \pm 6$ ($n= 25$, 2SE), which is in good agreement with the accepted value of $^{176}\text{Hf} - ^{176}\text{Hf} = 0.282482 \pm 13$ (Sláma et al., 2008) (Figure B.2.3.1a). FC-1 was also used as a $^{207}\text{Pb}/^{206}\text{Pb}$ internal standard so it is only possible to assess the accuracy of its Lu-Hf analysis. A weighted average of $^{176}\text{Hf} - ^{176}\text{Hf} = 0.282174 \pm 11$ ($n= 7$, 2SE), which is in

good agreement with the accepted value of $^{176}\text{Hf} - ^{176}\text{Hf} = 0.282184 \pm 16$ (Woodhead & Hergt, 2005) (Figure B.2.3.1b).

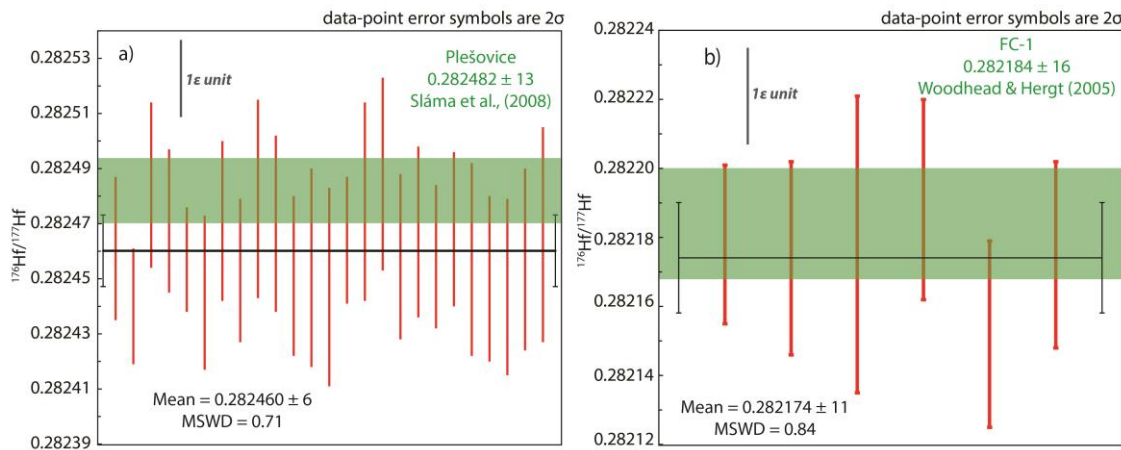


Figure B.2.3.1 – Weighted average plots of Plešovice and FC-1 standard Lu-Hf analyses.
Coloured bars represent accepted values of standards.

As for the Lu-Hf only zircon analyses, Mud Tank was used as the internal normalising standard for the LASS Lu-Hf analyses, and this yielded a weighted average $^{176}\text{Hf} - ^{176}\text{Hf} = 0.282507 \pm 9$ ($n = 8$, 2SE) (Figure B.2.3.2a). The currently accepted age for the Mud Tank zircon is an ID-TIMS age of $^{207}\text{Pb}/^{235}\text{U} = 732 \pm 5$ Ma (Black & Gulson, 1978). LASS analyses yield concordant or near concordant ellipses, and a weighted average age of $^{207}\text{Pb}/^{235}\text{U} = 760 \pm 24$ Ma (Figure B.2.3.2b). The spread in data and high uncertainty of the analyses is likely due to the low U and Pb contents of the zircon standard, which is from a carbonatite.

The B144/MunZirc standard yielded a weighted average of $^{176}\text{Hf} - ^{176}\text{Hf} = 0.282139 \pm 16$ ($n= 4$, 2SE; accepted value = 0.282135 ± 7 ; Fisher et al., 2011) (Figure B.2.3.3).

Although this synthetic zircon was analysed using the LASS setup it does not contain any U or Pb so no age determinations can be made.

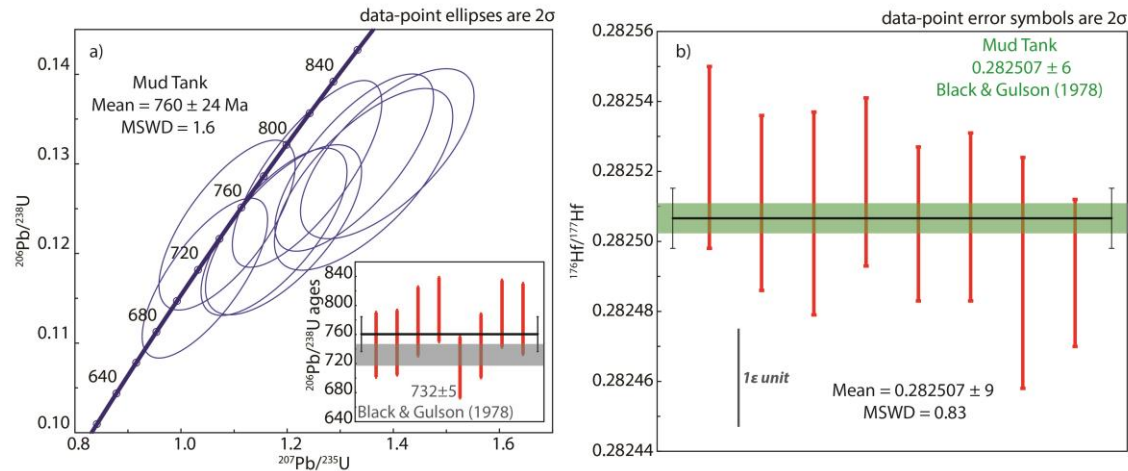


Figure B.2.3.2 – Concordia and weighted average plot of Mud Tank standard LASS analyses. a) Concordia and weighted average plots of U-Pb data. b) Weighted average plots of Lu-Hf data. Coloured bars represent accepted values of standards.

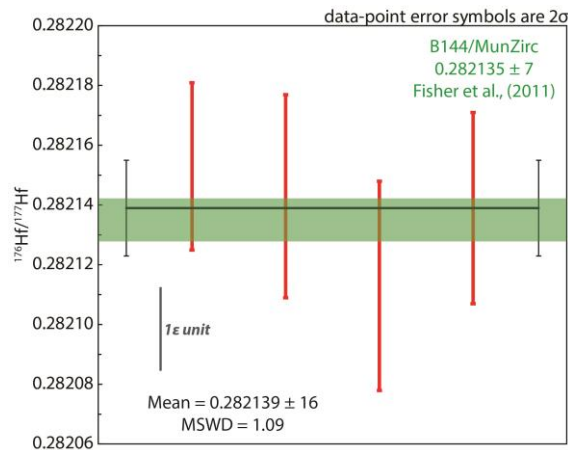


Figure B.2.3.3 – Weighted average plot of B144/MunZirc standard Lu-Hf LASS analyses. Coloured bars represent accepted values of standards.

The 91500 zircon standard has been well characterised in terms of U-Pb and Lu-Hf and thus serves as a good test of the LASS approach. The accepted $^{206}\text{Pb}/^{238}\text{U}$ ID-TIMS age for the 91500 zircon is 1063.4 ± 1.4 Ma (Schoene et al., 2006). Eight LASS analyses yield concordant data, with a $^{206}\text{Pb}/^{238}\text{U}$ weighted average of 1106 ± 12 Ma, which is slightly older than the ID-TIMS age. $^{207}\text{Pb}/^{206}\text{Pb}$ weighted average gives an age of 1077 ± 27 Ma, which compares well with the ID-TIMS $^{207}\text{Pb}/^{206}\text{Pb}$ age of 1066.4 ± 5 Ma (Schoene, et al., 2006) (Figure B.2.3.4a). A weighted average of $^{176}\text{Hf}-^{176}\text{Hf} = 0.282282 \pm 28$ ($n= 8$, 2SE), which is in good agreement with the accepted value of $^{176}\text{Hf}-^{176}\text{Hf} = 0.282305 \pm 6$ (Blichert-Toft, 2008) (Figure B.2.3.4b).

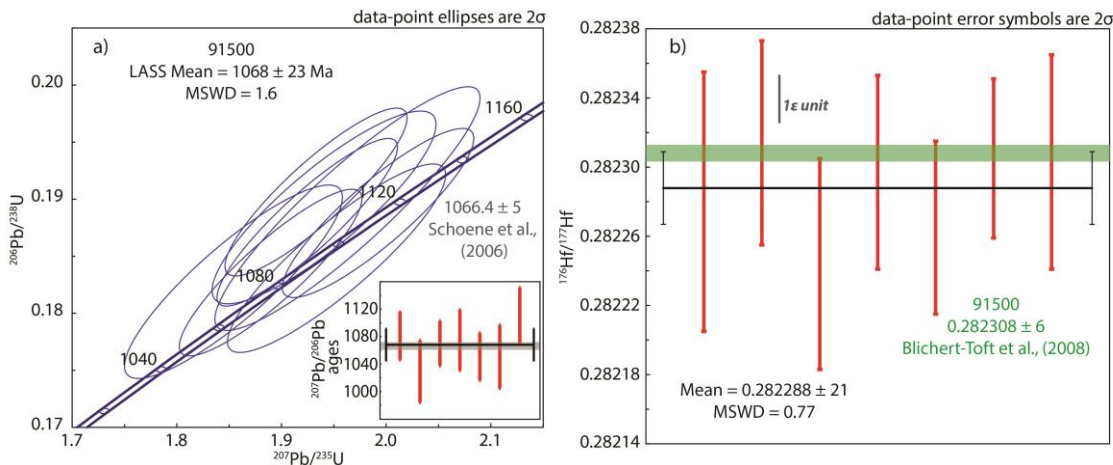


Figure B2.3.4 – Concordia and weighted average plot of 91500 standard LASS analyses.
a) Concordia and weighted average plots of U-Pb data. b) Weighted average plots of Lu-Hf data. Coloured bars represent accepted values of standards.

B.2.4 - LASS monazite standards

Trebilcock was used as the U-Pb internal standard and therefore it is not possible to make an assessment of accuracy for its LASS age determinations. Trebilcock was measured 200 times during the 3 days of LASS monazite analysis and therefore provides an excellent check on the accuracy of Sm-Nd isotopic determinations throughout the analysis period. A weighted average of ^{143}Nd - $^{144}\text{Nd} = 0.5126114 \pm 42$ ($n = 187$, 2SE), which is in excellent agreement with the accepted values of both the ID-TIMS and the LA-MC-ICP-MS accepted values of ^{143}Nd - $^{144}\text{Nd} = 0.512616 \pm 11$ and 0.512607 ± 26 respectively (Fisher et al., 2011) (Figure B.2.4.1a).

For monazite LASS analyses the JNd_i synthetic glass was used as the internal standard for Sm-Nd. Analyses of this standard yielded a weighted average ^{143}Nd - $^{144}\text{Nd} = 0.512111 \pm 11$ ($n = 15$, 2SE), which is in good agreement with the accepted values for both ID-TIMS and LA-MC-ICP-MS analyses of ^{143}Nd - $^{144}\text{Nd} = 0.512115 \pm 7$ and 0.512089 ± 23 respectively (Fisher et al., 2011) (Figure B.2.4.1b).

The synthetic LREE glass was also used as an internal standard for Sm-Nd LASS analyses, yielding a weighted average of ^{143}Nd - $^{144}\text{Nd} = 0.512112 \pm 14$ ($n = 32$, 2SE), which is in excellent agreement with the accepted values for both ID-TIMS and LA-MC-ICP-MS analyses of ^{143}Nd - $^{144}\text{Nd} = 0.512115 \pm 7$ and 0.512097 ± 33 respectively (Fisher et al., 2011) (Figure B.2.4.1c).

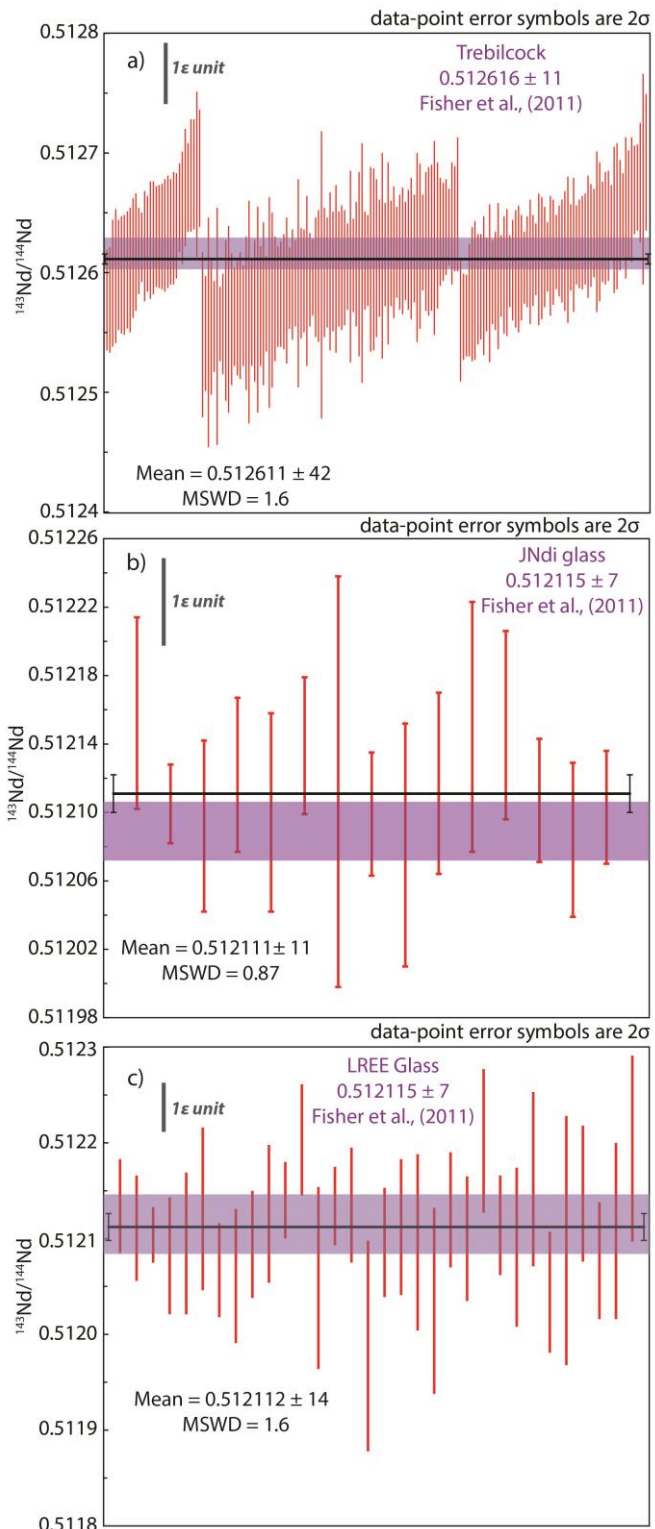


Figure B.2.4.1 – Weighted average plot of a) Trebilcock, b)JNdI glass and c)LREE glass standard Sm-Nd analyses. Coloured bars represent accepted values of standards.

The KMO monazite is used in this study as a check on both the U-Pb and Sm-Nd isotopic accuracy of the LASS method. Previous ID-TIMS by (Machlachlan et al., 2004) give as $^{207}\text{Pb}/^{206}\text{Pb}$ weighted average age of 1822 ± 1.5 Ma. LASS analyses of KMO are concordant on both conventional Concordia and Tera-Wasserburg diagrams and yield a weighted average age of 1828 ± 14 Ma ($n=11$, 2SE) (Figure B.2.4.2a). The only published Sm-Nd isotopic composition of KMO is presented in Goudie et al., (2014), where the LASS $^{143}\text{Nd}/^{144}\text{Nd}$ weighted average is calculated to be 0.511433 ± 29 . LASS analyses from this study give a $^{143}\text{Nd}/^{144}\text{Nd}$ weighted average of 0.511384 ± 40 (Figure B.2.4.2b), which is in agreement with the above value.

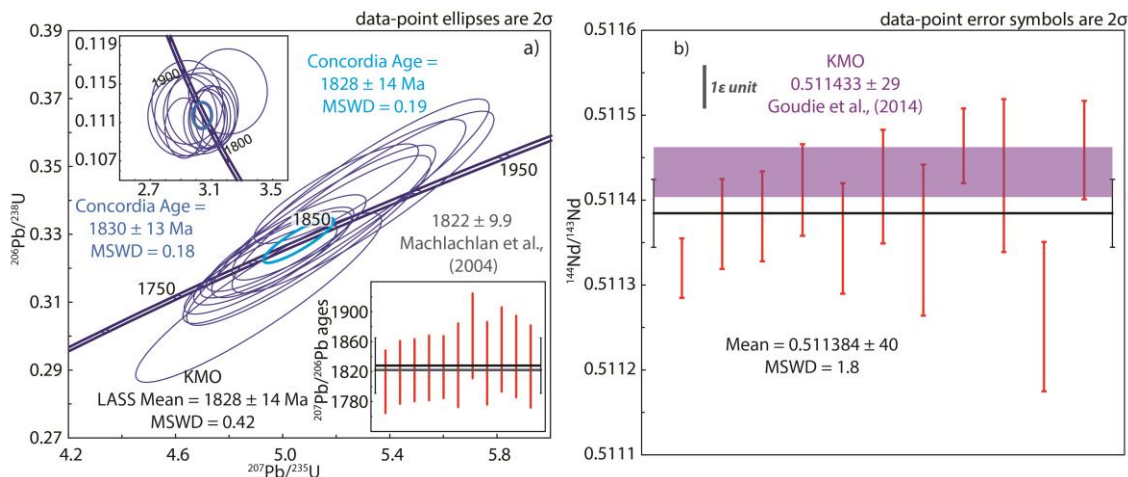


Figure B.2.4.2 – Concordia and weighted average plot of KMO standard LASS analyses.
a) Concordia, Terra-Wasserburg and weighted average plots of U-Pb data. b) Weighted average plots of Sm-Nd data. Coloured bars represent accepted values of standards.

Twelve analyses of the Thai monazite standard were performed throughout the analysis period. As this standard has been characterised for both U-Pb and Sm-Nd isotopes it serves as a useful check on the accuracy of the LASS method. Analyses yield concordant and near concordant results when plotted on Tera-Wasserburg plots (Figure B.2.4.3). Error! Reference source not found.a), with divergence from Concordia due to their young age and insufficient in-growth of ^{207}Pb . The weighted average $^{206}\text{Pb}/^{238}\text{U}$ age = 27.56 ± 0.79 Ma. This is consistent with the ID-TIMS age reported by (Dunning et al., 1995) of 26.8 ± 0.5 Ma. The weighted average of Thai monazite by LASS is $^{143}\text{Nd}-^{144}\text{Nd} = 0.512668 \pm 20$ ($n = 12$, 2SE), which is consistent with both the ID-TIMS and LA-MC-ICP-MS values reported by (Fisher et al., 2011) of $^{143}\text{Nd}-^{144}\text{Nd} = 0.512646 \pm 10$ and $^{143}\text{Nd}-^{144}\text{Nd} = 0.512578 \pm 26$ (Figure B.2.4.3b).

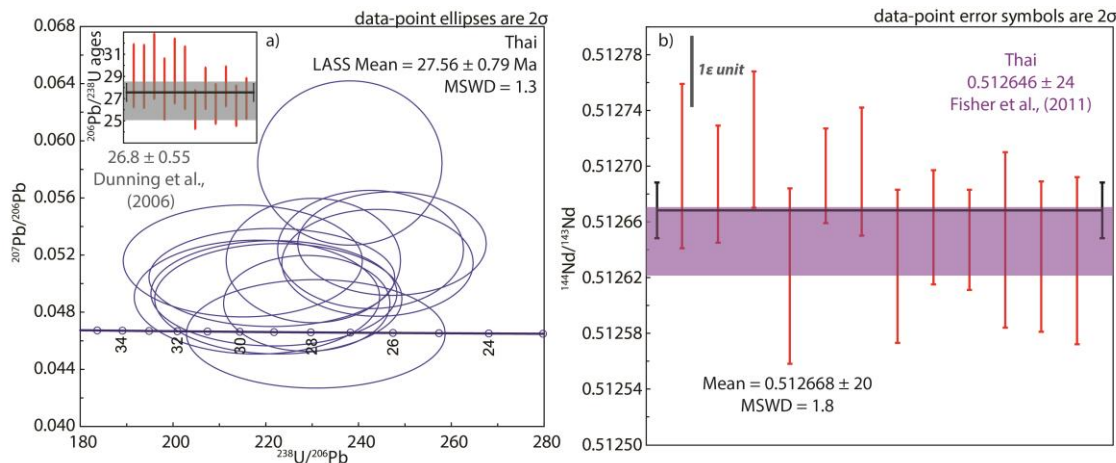


Figure B.2.4.3 – Terra-Wasserburg and weighted average plot of Thai standard LASS analyses. a) Terra-Wasserburg and weighted average plots of U-Pb data. b) Weighted average plots of Lu-Hf data. Coloured bars represent accepted values of standards.

Appendix C – Supplementary data files

Supplementary data files are presented here in digital format only.

C1 – Zircon *in situ* U-Pb data

C2 – Zircon *in situ* Lu-Hf data

C3 – Zircon *in situ* LASS U-Pb – Lu-Hf data

C4 – Monazite *in situ* LASS U-Pb – Sm-Nd data